Medieval demise of a Himalayan giant summit induced by mega-landslide

Jérôme Lavé, Cyrielle Guérin, Pierre Valla, Valery Guillou, Thomas Rigaudier, Lucilla Benedetti, Christian France-Lanord, Ananta Prasad Gajurel, Guillaume Morin, Jean Pascal Dumoulin, et al.

Title: Medieval demise of a Himalayan giant summit induced by mega-landslide.

authors

Jérôme Lavé [1,*]
Cyrielle Guérin [2]
Pierre G. Valla [3]
Valery Guillou [4]
Thomas Rigaudier [1]
Lucilla Benedetti [4]
Christian France Lanord [1]
Ananta Prasad Gajurel [5]
Guillaume Morin [1#]
Jean Pascal Dumoulin [6]
Christophe Moreau [6]
Valier Galy [7]

affiliations

1. CRPG, CNRS, Université de Lorraine, Vandoeuvre les Nancy, France
2. CEA- DAM, DIF, Arpajon, France
3. ISTerre, CNRS, Université Grenoble Alpes, Grenoble, France
4. CEREGE, CNRS, Aix Marseille Université, Aix-en-Provence, France
5. Department of Geology, Tribhuvan University, Kathmandu, Nepal
6. LMC14, LSCE, CEA, CNRS, Université Paris-Saclay, Gif-sur-Yvette, France
7. Department of Marine Chemistry and Geochemistry, Woods Hole Oceanographic Institution, Woods Hole, USA

\# now at INRAE, Aix Marseille Univ, UMR RECOVER, Aix-en-Provence, France

* corresponding author, email address : jerome.lave@univ-lorraine.fr

Abstract

Despite numerous studies on Himalayan erosion, it is not known how the very high Himalayan peaks erode. While valley floors are efficiently eroded by glaciers, the intensity of periglacial processes, which erode the headwalls extending from glacial cirques to crest-lines, appears to decrease sharply with altitude[1,2]. This contrast suggests that erosion is muted and much less than regional rock uplift rates for the highest Himalayan peaks raising questions about their long-term evolution[3,4]. Here we report geological evidence for a giant rockslide that occurred around 1190 AD in the Annapurna massif (central Nepal), involving a total rock volume of ~23 km^3. This event collapsed a paleosummit culminating likely above 8000 m in altitude. Our data suggest that a mode of high-altitude erosion could be mega-rockslides, leading to the sudden reduction of ridge crest elevation by several hundred meters and ultimately preventing the disproportionate growth of the Himalayan peaks. This erosion mode, associated with steep slopes and high relief arises from a greater mechanical strength of the peak substratum, probably due to the presence of permafrost at high altitude. Giant rockslides also have implications for landscape evolution and natural hazards: the massive supply of finely-crushed sediments can fill valleys >150 km farther downstream and overwhelm the sediment load in Himalayan rivers for a century or more.

Main text

On the human time scales, mountain peaks appear eternal. Yet, on geological time scales, mountain peaks are ephemeral: their shape and altitude are constantly evolving in response to the competition between tectonic uplift and erosion. However, very few direct observations exist of how Earth's highest mountain peaks evolve. Whereas their growth can be considered progressive over time, we don't know if their erosion is also progressive or episodic, or whether summit erosion proceeds at the same rates as valley-floor lowering[5]?

It has been postulated that a glacial buzzsaw mechanism places an upper limit on mountain elevation and relief irrespective of the tectonic uplift rate[3,6], confining mountain heights to within about 1.5 km of the local Equilibrium Line Altitude[7] (ELA). In this concept, efficient periglacial weathering, frost cracking, and rock falls along steep hillslopes produce rapid retreat of glacier cirque headwalls, limiting peak elevation at rates commensurate with rapid valley-floor downcutting by glaciers[8]. In various settings, however, this concept has been challenged[9-12]. In the Himalayas, one of the most active mountain range on Earth, the >8000-m peaks culminate ~3000 m above the ELA and seem to contradict the notion of a comprehensively operating glacial buzzsaw[1,12]. At these extreme elevations, local measurements of cirque headwall retreat show rates mostly lower than regional erosion rates[13-16]. Frozen-based ice cover, as well as a sharp decrease in frost-cracking efficiency for increasing altitudes, due to the absence of common freeze-thaw cycles[1,2], are suspected to strongly limit the erosion of the glaciated peaks protruding far above the ELA[1]. If high-elevation summit erosion is unable to match rapid valley-floor downcutting rates, this mismatch could lead in theory to disproportionate growth of the Himalayan peaks.

In steep and active mountains, it is conjectured, however, that mechanical strength of the mountain rock mass sets an upper limit to peak elevation and the height of oversteepened slopes[4],

such that slope adjustment might occur through landslides at a rate paced by river downcutting. This equilibrium has been corroborated in non-glaciated and vegetated landscapes, where landslides can be tracked from satellite-image inventory[17-19]. The 2021 rock-and-ice avalanche of the Ronti peak (India)[20] illustrated that landslides can also contribute dramatically to the erosion of high-elevation glaciated Himalayan peaks. Nevertheless, the lack of systematic landslide inventories precludes any reliable assessment of the relative contribution of this erosive process in long-term evolution of high-elevation mountainous areas. Instead, the few coseismic landslide inventories show an apparent sharp decrease in landslide occurrence at high elevations[21]. This observation indicates either an erosion mechanism distinct from landsliding, or a size-frequency distribution of landslides[17] that would be clearly skewed in favour of very large landslides, remaining infrequent enough not to be seen by remote sensing techniques.

In the present study, we document evidence of a recent giant rockslide in the Annapurna region (central Himalayas, Nepal; Fig.1), which illuminates the topographic evolution of high Himalayan peaks, their abrupt erosion by large rockslides, and the disproportionate consequences of such collapses along downstream drainage systems.

Uncovering a giant rockslide deposit

The southern flank of the Annapurna massif, currently culminating at 8091 m a.s.l., presents a 6 km drop in elevation from the high summits to the Lesser Himalayas hills. The area encompasses steep slopes, active microseismicity[22], and strong ground shaking by major earthquakes[23,24] (Mw≥8). Heavy monsoon precipitation prevails over its southern slopes. This tectonic and climatic setting induces some of the highest regional erosion rates in the Himalayan range, with values of 3-5 mm/yr[25-27].

The Annapurna massif, dominated by calcareous metasediments of the Tethyan Sedimentary Series[28,29] (TSS) (Extended Data Fig. 1), is punctuated by several large glacial cirques, separated by >7500-m glaciated peaks (Fig. 1). Between Annapurna III and IV, the Sabche cirque is a deep and wide depression bordered by extremely steep cliffs (Fig. 1). The cirque bottom is filled with light-colored sedimentary deposits, which have been eroded into large and tapering penitents several hundred meters high (Fig. 1d). Inaccessibility has so far prevented precise field description of these deposits, which have been interpreted from afar as subglacial tills or glaciolacustrine sediments[30]. Up close, these massive deposits are well consolidated, especially in the southern, most basal part, comprising finely-crushed matrix-supported breccia with centimetric to decimetric angular clasts from various TSS carbonate lithologies (Extended Data Fig. 2 and Supp. Info. SI-1). The coarse elements are more abundant in the upper part of the deposit and reach sizes of several meters. The breccia color is quite uniform (white to grayish) except locally with yellowish units reminiscent of the yellow limestones of the Annapurnas[28] (Fig. 1c). The breccia sediment infill appears as relatively continuous without any apparent unconformity but displays incomplete mixing, internal shear zones and rare jigsaw facies (Extended Data Fig. 2). These sedimentary features[31], the intense rock fragmentation, the exceptional thickness (>400 m _ Fig. 1d), and the exclusive presence of these breccia among all cirques of the Annapurna massif, unequivocally indicate that these breccia sediments were generated by a single rockslide granular avalanche.

The elevation of the breccia remnants along the southern side of the cirque and of a few preserved top surfaces in its northern part (Fig. 1) suggests that the cirque was completely filled by

rockslide debris (Supp. Info. SI-4), with thickness locally >1 km. In addition, a debris avalanche overflowed the cirque and spilled into the upper Seti valley where scattered outcrops of massive breccia deposits can be observed for ~10km downstream along the valley walls or as isolated >200-m-high massive spur remnants (Extended Data Fig. 3 and Supp. Info. SI-2). These remnants are dominated by angular TSS limestone clasts in a finely-fragmented and pulverized carbonate-rich matrix. Little mixing appears at the metric scale (as observed for Sturzströme in motion[32]), dyke injections are deformed by brittle deformation, and the basal shearing contact with the gneissic-bedrock valley flanks is overlain by a mixing zone incorporating fragmented vegetal debris.

Volume and Age of the rockslide deposit

Subtraction of the restored basal topography of the Sabche cirque from the initial breccia deposit surface provides an estimated volume of the rock avalanche deposits of 23.5 $^{+4}/_{-3}$km^3. An additional volume of ~3.5 km^3 is similarly inferred along the upper Seti valley (see Method, Extended Data Fig. 4 and Supp. Info SI-4). Accounting for an average breccia porosity of 15 ±5% (Supp. Info SI-5), this reconstructed deposit would correspond to a total volume of collapsed rock of 23 $^{+3.5}/_{-3}$km^3, constituting the largest rockslide described in the Himalayas to date[33,34].

Four 2- to 5-m high blocks of Silurian marly limestone were sampled on a large blocky and chaotic remnant of the original deposit surface (Extended Data Fig. 5) for ^{36}Cl surface-exposure dating (Supp. Info table SI-11-2). They display consistent ^{36}Cl concentrations with an average surface-exposure age of 1196 ±75(2σ) yr AD (fig. 2a).

In parallel, infra-red stimulated luminescence (IRSL) dating on feldspar were conducted on three breccia samples from an internal shear zone, assuming that increased temperature and/or shear heating[35] during the rock avalanche did partially reset the IRSL signal (Extended Data Fig. 6, and Supp. Info. SI-12). The observed partial reset is moderate for two samples with average apparent IRSL ages of several kyr, but is highly pronounced for one sample taken in the most-deformed levels. For the latter, the IRSL age distribution is highly-scattered with an apparent modal age of ~1200 yr BP and an estimated minimum age of ~900 yr BP (Fig. 2a), consistent with surface-exposure dating of the top relict surface.

Finally, eight ^{14}C analyses on plant fragments of stripped vegetation in the contact zone between rock-avalanche material and bedrock in the upper Seti valley (site K on Fig. 1), provided reproducible calibrated ages (Fig. 2a, Supp. Info. Table SI-10-1). The most probable age of 1190 ±26(2σ) AD is strikingly consistent with the ^{36}Cl surface-exposure ages of the rockslide deposit surface, thereby confirming the monogenic nature of the rock avalanche between the Sabche cirque and the upper Seti valley.

Reconstruction of the collapsed paleo-peak

In order to understand the origin of the collapsed rock mass, we identified the failure surface in the NE cirque part below the Annapurna IV (Figs. 1 and 3). There, the morphology of the rock cliffs stands out (see Methods and Extended Data Fig. 4d) with fresh planar or prismatic structural surfaces, devoid of any major glacier or runoff-related erosion. The proposed giant rockslide, collapsing along this uneroded failure surface, would have beheaded the paleo-summit of Annapurna IV.

To reconstruct the initial geometry of the paleo-Annapurna IV from the restored rock volume of 23 $^{+3.5}/_{-3}$km^3, we hypothesized that the stability of the paleo-summit hillslopes follows

mechanical characteristics that prevail for the whole Annapurna massif, for similar altitudes and lithologies. Stability of 82-100% of the high elevation slopes requires an apparent rock mass cohesion of 1-2 MPa, assuming a friction angle of 35 degrees (Methods and Extended Data Fig. 7 & 8). For these geomechanical properties, we generated thousands of random possible topographies for the Annapurna IV paleo-summit, and considered as acceptable only those fitting both the collapsed rock volume and the regional hillslope stability (Methods and Extended Data Fig. 9). Through this Bayesian approach, we estimated that the paleo-Annapurna IV may have peaked at an average elevation of ~8100 m (~600 m above the modern summit and comparable to the Annapurna I), and exceeded 8000 m with a probability of 0.65-0.76 (Fig. 3d). The eroded volume corresponds to an average 1 km of bedrock lowering, and involves lithologies ranging from Silurian to Cambrian (Fig. 3c) in good agreement with the diversity of colour and carbonate content of the breccia material (Fig. 4)

Sediment export and downstream consequences

The collapse released a huge amount of potential gravitational energy of ~1.2×10^{18} J (Fig. 3). Significant energy release was consumed in rock-material fragmentation, which, aided by the schistose nature of the marly-calcareous bedrock, likely explains the extreme degree of disintegration observed in the breccia material. After the paleo-summit collapse ~830 years ago, the erosion of the fine-grained breccia by rainwash, landsliding, pro-glacial streams, or glaciers, and their export by the upper Seti river, were extremely efficient and rapid: of the initial 23.5 km^3 of rockslide debris, only ~10% can still be observed today in the Sabche cirque (Extended Data Fig. 4c). Assuming long-term denudation rate of ~3mm/yr in the High Himalaya[26], the return time of a giant rockslide of similar volume would be >100 kyr at the scale of the entire Sabche cirque headwalls. The response time of the glacio-fluvial system to evacuate the Sabche breccia material appears therefore very short in comparison.

Farther downstream of the Seti river, the Pokhara Basin (Fig. 1) is known to have been filled very rapidly 500-1000 years ago[30,36] by ~5 km^3 of mostly conglomeratic sediment with calcareous clasts, whose only possible origin is the Sabche cirque. Sedimentary fill is characterized by the stratigraphic continuity of a succession of planar beds with varied facies (Supp Info. SI-9) that reflect rapid aggradation by fluvial, hyperconcentrated, or turbulent, sediment-laden flows[30,36].

Extensive ^{14}C dating of organic fragments found in the fine-grained units of the Pokhara sediments[36-38], collected at different burial depths, and complemented by eight new dates (Supp. Info. table SI-10-1), provide robust constraints on the timing of aggradation (Fig. 2b). They indicate onset of aggradation around 1200 AD at an average rate of 1m/yr until ~1300 AD. Taken together, the similarity in carbonate content (Fig. 4) and the age of the basal units in close agreement with the giant rockslide age, but stratigraphically postdating the breccia (Extended Data Fig. 3a) strongly suggest a co-genetic link between these two sedimentary units. The Pokhara conglomerates are thus best explained by the active erosion of the Sabche rock-avalanches breccia and by the rapid sediment transfer by Seti river down to Pokhara valley.

Fine conglomerates with calcareous pebbles irregularly crop out far downstream of Pokhara, along the Seti, the Trisuli and even the Narayani river (Fig. 4) in the foreland (site N on Fig. 1). There, a fine, carbonate-rich conglomerate unit, dated at 1150-1220AD (^{14}C dating, Fig. 2a), shows how the Narayani was temporarily overwhelmed by sediments from the paleo-Annapurna IV collapse. Such sediment pulse may even have reached the mid-Ganga plain, as

suggested by a >3-m thick unit at the top of a core drilled into an elevated Narayani megafan lobe (site G on Fig. 1). This unit is anomalously rich in TSS carbonate (30-60%) as compared to the average proportion of ~10% in Late-Pleistocene to modern Narayani sediments (Fig. 4, and Extended Data Fig. 10).

The amalgamated sediment volume in the Pokhara basin, middle Seti valley, and Narayani megafan lobe may have reached 15 km^3 (Supp. Info. SI-9-C), thereby representing ≤50% of the initial Sabche breccia volume (assuming 30% fluvial sediment porosity). The other half was presumably partly dissolved and partly exported farther downstream as suspended load, and may have ended up in the Bengal fan, the largest sediment sink for most Himalayan sediment[39].

Sediment aggradation in Pokhara valley suggests that the most intense phase of breccia removal in the Sabche cirque and associated sediment supply downstream lasted for a century (Fig. 2b) and impacted the whole downstream sediment routing system. During that period, the rate of sediment yield (0.1-0.2 km^3/yr exported from a 60-km^2 area) was comparable to the highest measured values of post-volcanic eruption sediment transport[40] and led to an overwhelming content of TSS material in river sediments >300 km downstream. Compared to the Narayani basin (30,000 km^2), which exports annually ~0.05km^3/yr of sediment[41,42], post-collapse erosion of the Sabche breccias (only 0.2% of the Narayani total basin area) would have increased this annual flux by a factor of 3 over 100-150 years (see also carbonate-based budget in Supp. Info. SI-9-D).

The collapse has paradoxically positive and negative downstream consequences. In the long term, the creation of a large flat surface in the Pokhara valley has undoubtedly been beneficial, allowing the development of extensive agricultural areas, and, above all, the recent development of the country's second largest city with all of its infrastructures. On the contrary, in the short term, if the paleo-Annapurna IV collapse occurred today, the Pokhara metropolitan area would be decimated, with appalling human and economic costs. Not only would the upstream parts of the valley be swept away by the granular avalanche, but numerous sediment-laden flows would rapidly bury the valley under tens of meters of sediment, leaving a vast gravel plain in the Seti valley. Even the Indian side of the Ganga plain, i.e. a densely populated region, might be impacted by increased probability of river-channel avulsions and rapid sedimentation along the Narayani megafan. Although such events are rare, understanding the causes of the paleo-Annapurna IV collapse and its downstream consequences appears thus fundamental to comprehend the major threat that potential giant rockslides can pose to the local populations and infrastructures in these high-mountain regions.

Possible causes for the Sabche rockslide

Several factors make the High Himalaya region clearly prone to large-scale slope failure. Glacial valley deepening due to sub-glacial carving, combined with intense frost cracking close to the ELA[2], represents one of the major pre-conditioning factors that produce steep, unstable headwalls surrounding glacier cirques. Schistosity orientation and structural planes also likely guide slope failure of the paleo-Annapurna IV (Extended Data Fig. 4d).

By contrast, causes triggering the Sabche rockslide remain speculative. It has been suggested previously[36] that the filling of the Pokhara Basin arose from various pulses of debris flows following numerous landslides activated by 3 large earthquakes, at 1100 ±50AD[23], 1255AD and 1344 AD[24]. According to ^{14}C dating of breccia at Karuwa (site K on Fig. 1), the Sabche rockslide occurred after 1150AD and before 1255AD at >99% confidence. Seismic triggering due

to one of these 3 large earthquakes seems therefore excluded. Nevertheless, as the current catalog of paleo-earthquakes is likely incomplete for medieval times, we cannot exclude the impact of an undocumented earthquake in the region.

Independently, climate might also be involved as a preparatory or/and triggering factor for the Sabche collapse. The Medieval Climate Anomaly[43], from 900 to 1200AD, was possibly characterized by >+1°C warmer temperatures in the High Himalaya. This could have thawed part of the failure surface (see estimate in Supp. Info. SI-8) and favoured high-elevation rockslide(s)[20]. Although the cohesion loss from thawing appears to have been likely insufficient to trigger the paleo-Annapurna IV collapse (unless the rock mass was already close to a critical state), such climatic factor on high-elevation bedrock destabilization calls for closer attention on the effects of current global warming when assessing future gravitational hazards related to the high Himalayan peaks.

The fate of the High Himalayan peaks

The identification of a cataclysmic rockslide around 1190 AD, which beheaded what may have been the Himalaya's 15th 8,000-m peak, provides key insights into the likely evolution of the highest Himalayan peaks. First, this is not an isolated case. Several giant rockslides have been documented[33,34,44] in central Nepal with deposits reaching up to 10-15 km^3. All are located in the high Himalayas and originated from summits/ridges between 4500 and 6000m elevation. Although the current catalogue is incomplete and precludes definition of a precise erosion budget, massive summit collapses resulting in a sudden reduction of their height by several hundred meters could be the primary denudation mode of high, glaciated Himalayan peaks.

Notably, high summits commonly display steeper slopes, with median values rising from 35° below the ELA to 50° above it[2,45]. Steep slopes surrounding the glacial cirques of the Annapurnas are maintained by higher bulk material strength. The regional cohesion values (C≈1-2MPa) calculated for the glaciated relief cannot be considered as absolute values, because the transient effects of pore pressure or seismic acceleration have not been taken into account[46]. Nevertheless, they appear, for similar internal friction angles, ~4 times higher than the cohesion values (C≈0.2-0.7MPa) for the fluvially-dominated High Himalayan landforms (below 4000 m, south of the glaciated Annapurna ridges _ Supp. Info. SI-6), and an order of magnitude higher than in other non-glaciated high mountains[47] (C≤0.1MPa but using a distinct approach to derive cohesion values). In the Himalayas, this higher rock strength is not related to a lithological effect[12], given that the steeper slopes at high altitudes in central Himalaya have values independent of the rock type[2]. Instead, we surmise that the higher rock mass strength is favoured by permanently frozen conditions at high elevations. Such climatic conditions hold rocks in place by ice-rock interlocking[48,49], while preventing regolith formation, penetrative chemical weathering, and limiting groundwater recharge and high pore pressures at depth. If permafrost strengthens the first tens or hundreds of meters below the ground surface (Supp. Info. SI-8), and/or if weakened bedrock is absent near the surface, then the initiation of small and medium-sized landslides becomes more difficult. This could explain their very rare occurrence at high altitudes, and the need to erode the high summits through rare, but large deep-seated rockslides.

The above considerations on the evolution of glaciated high peaks allow us to revisit the concept of glacial buzzsaw. While topographic data suggest that the mean elevation of mountain ranges may be directly limited by active glacial and periglacial erosion processes[3,7], the glacial buzzsaw mechanism is not sufficiently effective, where rock uplift is sustained, to prevent the emergence of high peaks >3000 m above the snowline[12], as observed in the Annapurnas massif. On the contrary, once a mountain peak passes over the zone where rock mass is permanently frozen and the intensity of frost cracking drops drastically, the frozen conditions provide enhanced protection against surface erosion. This may even initiate a positive feedback. The increased mechanical strength of the frozen, unweathered rock mass promotes headwall stability, and an increase in both their length and steepness[46]. In turn, the increased steepness of the headwalls that prevents the accumulation of ice and glacial erosion[11], combined with headwall lengthening[12], allows the growth of high peaks and their further protrusion into the realm of permanently frozen and muted periglacial erosion conditions (Fig. 5). This positive feedback has a limit, however, set by the cohesion of the deep unweathered rock mass, and our observations suggest that deep-seated rockslides are ultimately the controlling mechanism that limits the persistent growth of the high Himalayan glaciated summits (Fig. 5).

Such a conceptual scenario (Fig. 5) might operate both on a regional (central Himalaya) and global scale. Many large-scale tectonic zones undergoing local sustained uplift rate present high peaks that protrude well above the snow line (i.e. by 2500 to 4000 m), either in the Himalayan syntaxes (Nanga Parbat and Namche Barwa), the Karakoram, the Pamir, the Western Kunlun Cordillera, the Gongga Shan, the central TianShan (Jengish Chokusu and Khan Tengri massifs), or, far from the India-Asia collision, e.g. in the Denali or St Elias massifs in Alaska. Future work should assess the erosive contribution of giant rockslides on the long-term topographic evolution of these regions, and also quantify a likely relationship between the rock uplift rate and the amplitude of relief above the snowline[50].

References :

1. Banerjee, A., & Wani, B. A. (2018). Exponentially decreasing erosion rates protect the high-elevation crests of the Himalaya. *Earth and Planetary Science Letters*, *497*, 22-28.
2. Scherler, D. (2014). Climatic limits to headwall retreat in the Khumbu Himalaya, eastern Nepal. *Geology*, *42*(11), 1019-1022.
3. Brozovic, N., Burbank, D. W., & Meigs, A. J. (1997). Climatic limits on landscape development in the northwestern Himalaya. *Science*, *276*(5312), 571-574
4. Burbank, D. W., Leland, J., Fielding, E., Anderson, R. S., Brozovic, N., Reid, M. R., & Duncan, C. (1996). Bedrock incision, rock uplift and threshold hillslopes in the northwestern Himalayas. *Nature*, *379*(6565), 505-510.
5. Molnar, P., & England, P. (1990). Late Cenozoic uplift of mountain ranges and global climate change: chicken or egg?. *Nature*, *346*(6279), 29-34.
6. Montgomery, D. R., Balco, G., & Willett, S. D. (2001). Climate, tectonics, and the morphology of the Andes. *Geology*, *29*(7), 579-582.
7. Egholm, D. L., Nielsen, S. B., Pedersen, V. K., & Lesemann, J. E. (2009). Glacial effects limiting mountain height. *Nature*, *460*(7257), 884-887.
8. Scherler, D., Bookhagen, B., & Strecker, M. R. (2011). Hillslope-glacier coupling: The interplay of topography and glacial dynamics in High Asia. *Journal of Geophysical Research: Earth Surface*, *116*(F2)
9. Thomson, S. N., Brandon, M. T., Tomkin, J. H., Reiners, P. W., Vásquez, C., & Wilson, N. J. (2010). Glaciation as a destructive and constructive control on mountain building. *Nature*, *467*(7313), 313-317.
10. Valla, P. G., Shuster, D. L., & Van Der Beek, P. A. (2011). Significant increase in relief of the European Alps during mid-Pleistocene glaciations. *Nature geoscience*, *4*(10), 688-692;
11. Ward, D. J., Anderson, R. S., & Haeussler, P. J. (2012). Scaling the Teflon Peaks: Rock type and the generation of extreme relief in the glaciated western Alaska Range. *Journal of Geophysical Research: Earth Surface*, *117*(F1).
12. Brocklehurst, S. H., & Whipple, K. X. (2007). Response of glacial landscapes to spatial variations in rock uplift rate. *Journal of Geophysical Research: Earth Surface*, *112*(F2).
13. Heimsath, A. M., & McGlynn, R. (2008). Quantifying periglacial erosion in the Nepal high Himalaya. *Geomorphology*, *97*(1-2), 5-23.
14. Seong, Y. B., Owen, L. A., Caffee, M. W., Kamp, U., Bishop, M. P., Bush, A., ... & Shroder, J. F. (2009). Rates of basin-wide rockwall retreat in the K2 region of the Central Karakoram defined by terrestrial cosmogenic nuclide 10Be. *Geomorphology*, *107*(3-4), 254-262.
15. Scherler, D., & Egholm, D. L. (2020). Production and transport of supraglacial debris: Insights from cosmogenic 10Be and numerical modeling, Chhota Shigri Glacier, Indian Himalaya. *Journal of Geophysical Research: Earth Surface*, *125*(10), e2020JF005586.
16. Orr, E. N., Owen, L. A., Saha, S., Hammer, S. J., & Caffee, M. W. (2021). Rockwall slope erosion in the northwestern Himalaya. *Journal of Geophysical Research: Earth Surface*, *126*(2), e2020JF005619.
17. Hovius, N., Stark, C. P., & Allen, P. A. (1997). Sediment flux from a mountain belt derived by landslide mapping. *Geology*, *25*(3), 231-234.

18. Larsen, I. J., & Montgomery, D. R. (2012). Landslide erosion coupled to tectonics and river incision. *Nature Geoscience*, *5*(7), 468-473.
19. Marc, O., Behling, R., Andermann, C., Turowski, J. M., Illien, L., Roessner, S., & Hovius, N. (2019). Long-term erosion of the Nepal Himalayas by bedrock landsliding: the role of monsoons, earthquakes and giant landslides. *Earth Surface Dynamics*, *7*(1), 107-128.
20. Shugar, D. H., Jacquemart, M., Shean, D., Bhushan, S., Upadhyay, K., Sattar, A., ... & Westoby, M. J. (2021). A massive rock and ice avalanche caused the 2021 disaster at Chamoli, Indian Himalaya. *Science*, *373*(6552), 300-306.
21. Roback, K., Clark, M. K., West, A. J., Zekkos, D., Li, G., Gallen, S. F., ... & Godt, J. W. (2018). The size, distribution, and mobility of landslides caused by the 2015 Mw7. 8 Gorkha earthquake, Nepal. *Geomorphology*, *301*, 121-138.
22. Pandey, M. R., Tandukar, R. P., Avouac, J. P., Lave, J., & Massot, J. P. (1995). Interseismic strain accumulation on the Himalayan crustal ramp (Nepal). *Geophysical Research Letters*, *22*(7), 751-754.
23. Lavé, J., Yule, D., Sapkota, S., Basenta, K., Madden, C., Attal, M., Pandey, R., 2005.Evidencefor a Great Medieval Earthquake (~A.D. 1100) in Central Himalaya, Nepal. Science307, 1302–1305.
24. Bollinger, L., Sapkota, S. N., Tapponnier, P., Klinger, Y., Rizza, M., Van der Woerd, J., ... & Bes de Berc, S. (2014). Estimating the return times of great Himalayan earthquakes in eastern Nepal: Evidence from the Patu and Bardibas strands of the Main Frontal Thrust. *Journal of Geophysical Research: Solid Earth*, *119*(9), 7123-7163.
25. Lavé, J., Avouac, J.P., 2001.Fluvial incision and tectonic uplift across the Himalayas of Central Nepal. J. Geophys. Res. 106 (B11), 26561–26591.
26. Burbank, D. W., Blythe, A. E., Putkonen, J., Pratt-Sitaula, B. G. A. B. E. T., Gabet, E., Oskin, M., ... & Ojha, T. P. (2003). Decoupling of erosion and precipitation in the Himalayas. *Nature*, *426*(6967), 652-655.
27. Godard, V., Burbank, D. W., Bourlès, D. L., Bookhagen, B., Braucher, R., & Fisher, G. B. (2012). Impact of glacial erosion on 10Be concentrations in fluvial sediments of the Marsyandi catchment, central Nepal. *Journal of Geophysical Research: Earth Surface*, *117*(F3).
28. Colchen, M., Le Fort, P., & Pêcher, A. (1986). *Recherches geologiques dans l'Himalaya du Nepal*. CNRS.
29. Godin, L. (2003). Structural evolution of the Tethyan sedimentary sequence in the Annapurna area, central Nepal Himalaya. *Journal of Asian Earth Sciences*, *22*(4), 307-328.
30. Fort, M. (1987). Sporadic morphogenesis in a continental subduction setting: an example from the Annapurna Range, Nepal Himalaya. *Zeitschrift für Geomorphologie*, *63*(9), 36.
31. Weidinger, J. T., Korup, O., Munack, H., Altenberger, U., Dunning, S. A., Tippelt, G., & Lottermoser, W. (2014). Giant rockslides from the inside. *Earth and Planetary Science Letters*, *389*, 62-73.
32. Bowman, E. T., Take, W. A., Rait, K. L., & Hann, C. (2012). Physical models of rock avalanche spreading behaviour with dynamic fragmentation. *Canadian Geotechnical Journal*, *49*(4), 460-476.

33. Weidinger, J.T., Schramm, J.-M., Surenian, R., 1996. On preparatory causal factors, initiating the prehistoric Tsergo Ri landslide (Langthang Himal, Nepal). Tectonophysics 260,95–107.
34. Weidinger, J.T., 2006, Predesign, failure and displacement mechanisms of large rockslides in the Annapurna Himalayas, Nepal. Eng. Geol. 83 (1), 201–216.
35. Bateman, M. D., Swift, D. A., Piotrowski, J. A., Rhodes, E. J., & Damsgaard, A. (2018). Can glacial shearing of sediment reset the signal used for luminescence dating? Geomorphology, 306, 90–101.
36. Schwanghart, W., Bernhardt, A., Stolle, A., Hoelzmann, P., Adhikari, B. R., Andermann, C., ... & Korup, O. (2016). Repeated catastrophic valley infill following medieval earthquakes in the Nepal Himalaya. *Science*, *351*(6269), 147-150.
37. Stolle, A., Bernhardt, A., Schwanghart, W., Hoelzmann, P., Adhikari, B. R., Fort, M., & Korup, O. (2017). Catastrophic valley fills record large Himalayan earthquakes, Pokhara, Nepal. *Quaternary Science Reviews*, *177*, 88-103.
38. Stolle, A., Schwanghart, W., Andermann, C., Bernhardt, A., Fort, M., Jansen, J. D., ... & Korup, O. (2019). Protracted river response to medieval earthquakes. *Earth Surface Processes and Landforms*, *44*(1), 331-341.
39. Lupker, M., France-Lanord, C., Lavé, J., Bouchez, J., Galy, V., Métivier, F., ... & Mugnier, J. L. (2011). A Rouse-based method to integrate the chemical composition of river sediments: Application to the Ganga basin. *Journal of Geophysical Research: Earth Surface*, *116*(F4).
40. Hayes, S. K., Montgomery, D. R., & Newhall, C. G. (2002). Fluvial sediment transport and deposition following the 1991 eruption of Mount Pinatubo. *Geomorphology*, *45*(3-4), 211-224.
41. Lupker, M., Blard, P.-H., Lavé, J., France-Lanord, C., Leanni, L., Puchol, N., Charreau, J.,Bourlès, D., 2012.10Be-derived Himalayan denudation rates and sediment budgetsin the Ganga basin. Earth Planet. Sci. Lett. 333–334, 146–156
42. Morin, G. P., Lavé, J., France-Lanord, C., Rigaudier, T., Gajurel, A. P., & Sinha, R. (2018). Annual sediment transport dynamics in the Narayani basin, Central Nepal: assessing the impacts of erosion processes in the annual sediment budget. *Journal of Geophysical Research: Earth Surface*, *123*(10), 2341-2376.
43. Mann, M. E., Zhang, Z., Rutherford, S., Bradley, R. S., Hughes, M. K., Shindell, D., ... & Ni, F. (2009). Global signatures and dynamical origins of the Little Ice Age and Medieval Climate Anomaly. *science*, *326*(5957), 1256-1260.
44. Fort, M. (2011). Two large late Quaternary rock slope failures and their geomorphic significance, Annapurna Himalayas (Nepal). *Geografia Fisica e Dinamica Quaternaria*, *34*(1), 5-14.
45. Gabet, E.J., Pratt-Sitaula, B.A., Burbank, D.W., 2004.Climatic controls on hillslope angle and relief in the Himalayas. Geology 32 (7), 629–632
46. Schmidt, K. M., & Montgomery, D. R. (1995). Limits to relief. *Science*, *270*(5236), 617-620.
47. Gallen, S. F., Clark, M. K., & Godt, J. W. (2015). Coseismic landslides reveal near-surface rock strength in a high-relief, tectonically active setting. *Geology*, *43*(1), 11-14.

48. Davies, M.C.R., Hamza, O., Lumsden, B.W., and Harris, C., 2000, Laboratory measurement of the shear strength of ice-filled rock joints: Annals of Glaciology, v. 31, p. 463–467, doi:10.3189/172756400781819897.
49. Gruber, S., and Haeberli, W., 2007, Permafrost in steep bedrock slopes and its temperature-related destabilization following climate change: Journal of Geophysical Research, v. 112, F02S18, doi:10.1029/2006JF000547.
50. Pedersen, V. K., Egholm, D. L., & Nielsen, S. B. (2010). Alpine glacial topography and the rate of rock column uplift: a global perspective. *Geomorphology*, *122*(1-2), 129-139.

Figure Legends :

Figure 1: Location maps of the Sabche breccia deposits. (a) Map of Nepal and Narayani basin (in red) with the >8000m summits (triangles) (G=drill cores GR1-2 (purple symbols) in Dudahi in India; S=Sabche; P=Pokhara; k=Kathmandu). (b) Topographic map of central Nepal focusing on the Seti river with the rock-avalanche breccia deposit (in yellow) in the Sabche cirque (headwaters of the Seti river) and along the upper Seti valley due to the rockslide of the Annapurna IV SW-flank. Subsequent erosion of this brecciated material led to the downstream sediment aggradation with massive conglomeratic terraces (in pink) in Pokhara basin and as far as south of the Main Boundary Thrust (MBT), near Narayangad (N). (S=Sabche; K=Karuwa; P=Pokhara; MCT=Main Central Thrust; STD=South Tibetan Detachment). (c) Zoomed map of the glaciated Sabche cirque showing contrasting breccia facies of and sample locations. (d) Aerial view of the Sabche cirque; its breccia filling (outlined by dashed line and 'br') exposed by large whitish penitents, hundreds of meters high, left by the erosion of the rock avalanche deposits.

Figure 2: Chronological constraints on deposits related to the Sabche rockslide. (a) Dating of the rock-avalanche deposit and Pokhara conglomeratic formation along the Seti river from the Sabche cirque down to Narayangad (site locations according to letters on fig. 1). From top to bottom: the probability density function (pdf) of ^{36}Cl exposure ages on blocks located on a upper surface relic of the rockslide deposit; zoom-in on the young tail of the feldspar IRSL age pdf showing partial signal reset (see complete pdf and individual aliquot ages on Extended Data Fig. 6) of a shearing band toward the base of the rockslide deposit in Sabche cirque; calibrated ^{14}C age pdf (black or gray solid lines) of wood debris sampled in the rock avalanche deposit in Karuwa (site K on Fig.1b) at the bedrock contact of the Seti valley; calibrated ^{14}C age pdf of organic fragments taken in the most basal conglomeratic units in Pokhara basin[36,38]; calibrated ^{14}C age pdf of a charcoal sampled in fine conglomerates north of Narayangad. The red curve represents the composite pdf, combining all available dating at each site. The numbers in parentheses indicate the number of dated samples.
(b) ^{14}C ages of numerous organic-debris samples from the central part of Pokhara basin (published and new dating), represented according to their stratigraphic relative elevation. Points and error bars correspond to the median value and the 95% confidence interval of the calibrated ages pdf, respectively. Analyses restricted to leaves, wood fragments, and tree trunks, in order to minimize the effect of suspected reworking in particular for charcoals. A notably rapid sedimentation rate of ~1m/yr

is documented. Note that "charcoal in buried paleosols" refers to charcoal collected from former soils on the flanks of the Seti Valley that were buried by and predate the Pokhara conglomerate.

Figure 3: Reconstruction of the Annapurna IV paleo-summit before its collapse. (a) Thickness of the rock-avalanche deposit estimated from breccia relics in Sabche cirque and along upper Seti valley. The orange arrow (oriented at N245) corresponds to the optimal direction of collapse (see Extended Data Fig. 9e). Circled black letters correspond to sites described in Fig. 1b. (b) Average shape of the reconstructed paleo-topographies that satisfy rock volume and hillslope stability constraints (grayed paleo-summit on top the present topography in slight transparency). (c) Cross section (location in a) through the middle of the Sabche cirque, withaveraged paleo-topography before collapse and approximate geometry of the post-collapse breccia deposit; *rsb* and *bdb* indicate the projection on the section plane of the centres of mass of the rock slide and breccia deposit volumes respectively, and whose elevation difference is used to calculate the released potential gravitational energy. (d) Probability densities (presented as histogram and resulting from 2000 random paleo-topographies) of the summit point elevation of the paleo-Annapurna IV satisfying increasing levels of requirement: firstly, the collapsed volume V_{RS} is in the range between 20 and 26.5 km^3 (grey); secondly, the summit slopes were stable regarding small to medium-size landslides (pink); thirdly, the safety factor (SF) along the failure surface was rather minimal (red) (see Method and Extended Data Fig. 9). The probability that the summit point could have exceeded 8000 m (thick line) is 65% and 76% if the paleo-topographies satisfy the first two and three conditions respectively.

Figure 4: Far downstream signature of the reworked rockslide deposits evidenced by sediment carbonate content. Comparison of the carbonate content in brecciated rock avalanche material, in TSS units at the source of the rockslide, in Pokhara conglomeratic formation, and in modern sediment along the Seti river (see also Supp. Info table SI-13). Unlike rockslide-derived sediments, which show a very high and relatively constant proportion of carbonate, modern sediments display downstream increasing dilution of the carbonate fraction, in particular after the confluence of the Seti with the Madi or Trisuli rivers. (Rivers: Ma = Mardi; M = Madi; Tr = Trisuli; Ka = Kali Gandaki; numbers in parenthesis = ratio of drainage areas with the Seti as denominator). Circled black letters and red acronyms correspond to the sites and faults mentioned in Fig. 1a and 1b.

Figure 5: Evolutionary sketch of the high peak emergence well above the ELA (Equilibrium Line Altitude) in a glaciated landscape undergoing sustained rock uplift. Starting from a fluvially-dominated landscape (A) raised above the ELA (white dotted line), glacier development and subglacial erosion leads to lengthening and steepening of headwalls (B and C). Whereas sub-glacial erosion keeps much of the relief below the ELA (i.e. buzzsaw effect[3]) and frost cracking erosion above the upper glaciated rim steepens the headwalls, further rock uplift drives the summit into the zone where the rock mass becomes permanently frozen and undergo minimal surface erosion (C and D). The continued growth of the peak elevation ends in a major gravitational instability (D and E), i.e. a giant rockslide that beheads the summit and results in a thick rock-avalanche deposit (yellow shading in E)

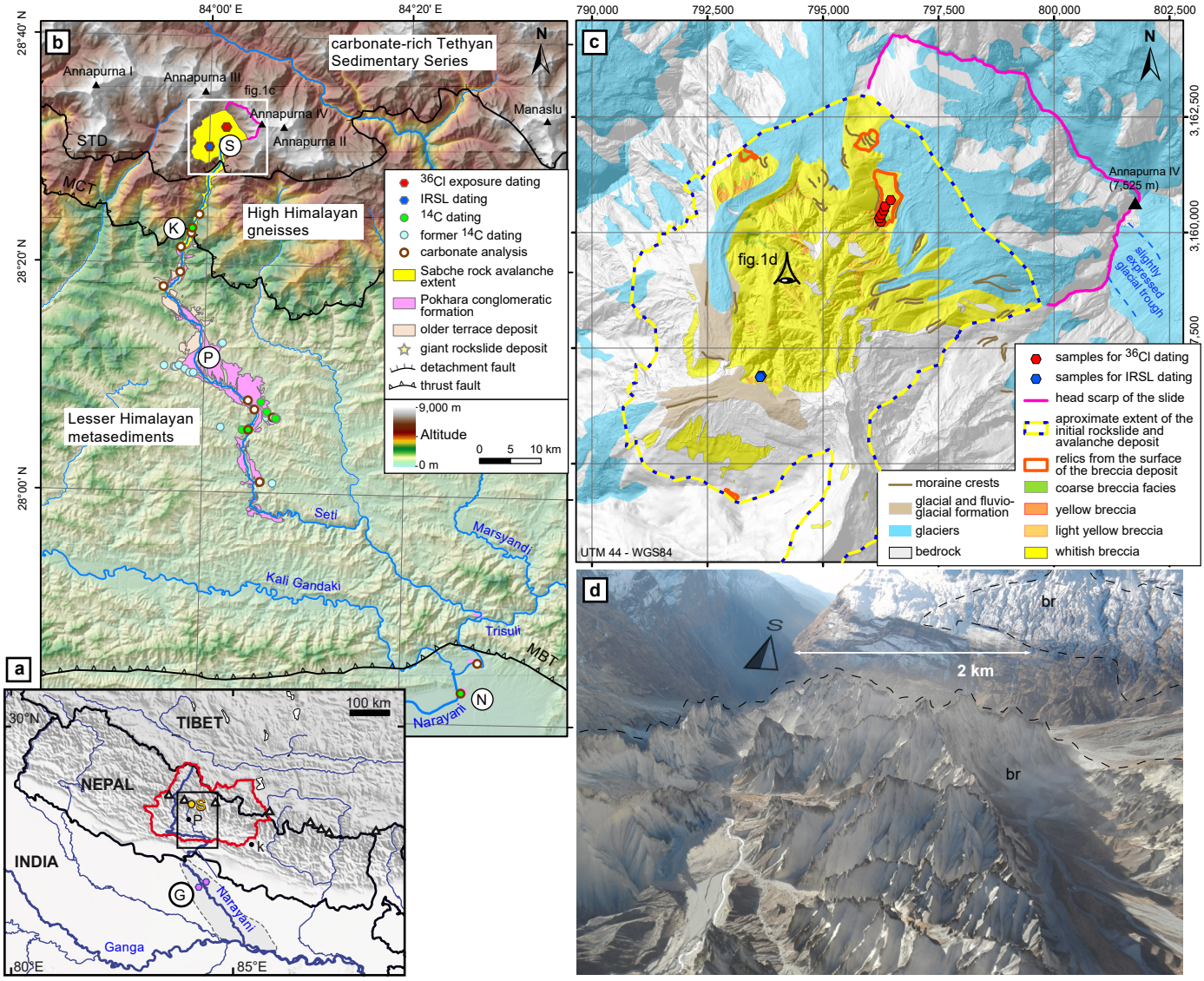
a
b
c
d
84°00' E
84°20' E
28°40' N
28°20' N
28°00' N
carbonate-rich Tethyan Sedimentary Series
Annapurna I
Annapurna III
fig.1c
Annapurna IV
Annapurna II
Manaslu
STD
MCT
High Himalayan gneisses
Lesser Himalayan metasediments
Seti
Marsyandi
Kali Gandaki
Trisuli
MBT
Narayani
36Cl exposure dating
IRSL dating
14C dating
former 14C dating
carbonate analysis
Sabche rock avalanche extent
Pokhara conglomeratic formation
older terrace deposit
giant rockslide deposit
detachment fault
thrust fault
9,000 m
Altitude
0 m
0 5 10 km
TIBET
NEPAL
INDIA
100 km
30°N
80°E
85°E
Ganga
Narayani
790,000
792,500
795,000
797,500
800,000
802,500
3,162,500
3,160,000
7,500
Annapurna IV (7,525 m)
fig.1d
slightly expressed glacial trough
UTM 44 - WGS84
samples for 36Cl dating
samples for IRSL dating
head scarp of the slide
aproximate extent of the initial rockslide and avalanche deposit
relics from the surface of the breccia deposit
coarse breccia facies
yellow breccia
light yellow breccia
whitish breccia
moraine crests
glacial and fluvio-glacial formation
glaciers
bedrock
br
2 km

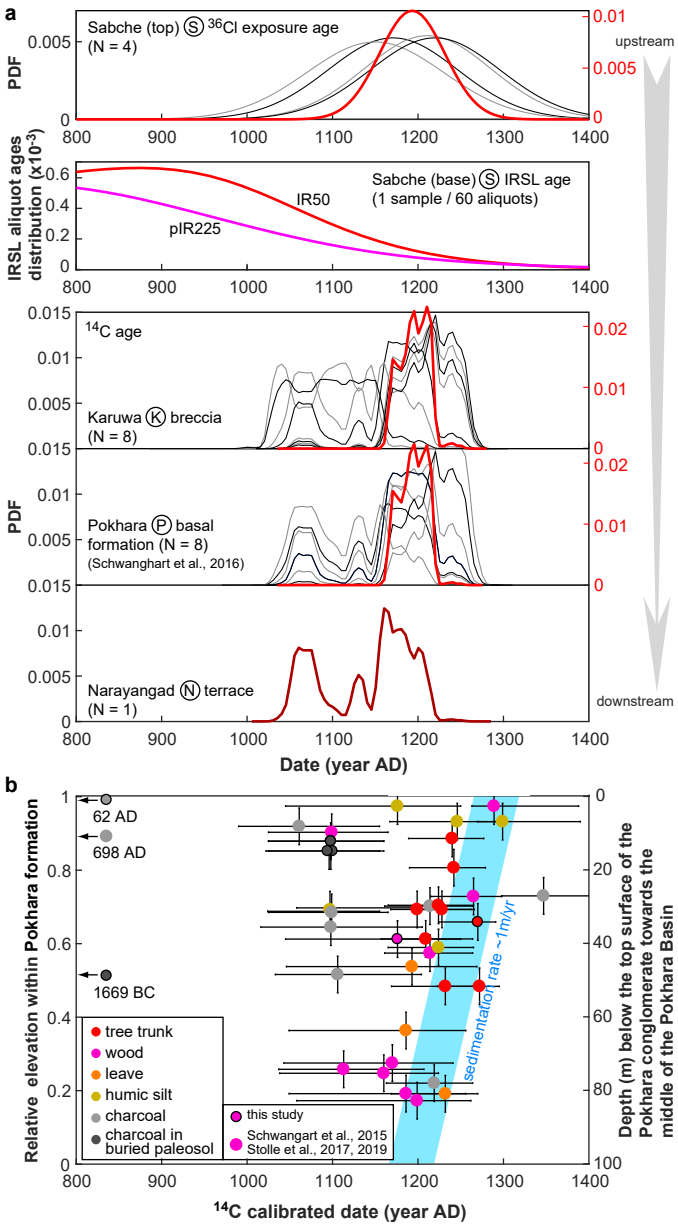
a
Sabche (top) Ⓢ 36Cl exposure age
(N = 4)
PDF
upstream
Sabche (base) Ⓢ IRSL age
(1 sample / 60 aliquots)
IR50
pIR225
IRSL aliquot ages distribution (x10-3)
14C age
Karuwa Ⓚ breccia
(N = 8)
Pokhara Ⓟ basal formation (N = 8)
(Schwanghart et al., 2016)
Narayangad Ⓝ terrace
(N = 1)
downstream
Date (year AD)
b
62 AD
698 AD
1669 BC
tree trunk
wood
leave
humic silt
charcoal
charcoal in buried paleosol
this study
Schwangart et al., 2015
Stolle et al., 2017, 2019
sedimentation rate ~1m/yr
Relative elevation within Pokhara formation
Depth (m) below the top surface of the Pokhara conglomerate towards the middle of the Pokhara Basin
14C calibrated date (year AD)

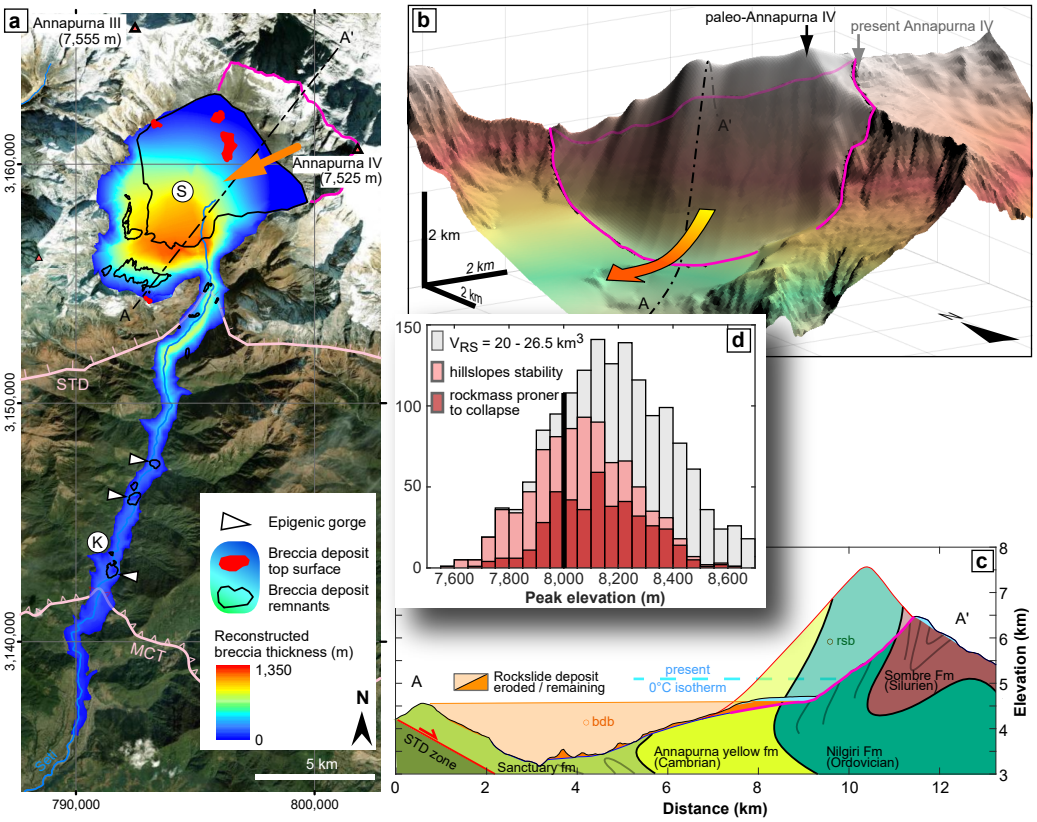
a
Annapurna III
(7,555 m)
A'
Annapurna IV
(7,525 m)
S
A
STD
K
MCT
3,160,000
3,150,000
3,140,000
790,000
800,000
Epigenic gorge
Breccia deposit
top surface
Breccia deposit
remnants
Reconstructed
breccia thickness (m)
1,350
0
N
5 km
b
paleo-Annapurna IV
present Annapurna IV
A'
A
2 km
2 km
2 km
d
V_{RS} = 20 - 26.5 km^3
hillslopes stability
rockmass proner
to collapse
150
100
50
0
7,600
7,800
8,000
8,200
8,400
8,600
Peak elevation (m)
c
A
A'
Rockslide deposit
eroded / remaining
present
0°C isotherm
rsb
bdb
STD zone
Sanctuary fm
Annapurna yellow fm
(Cambrian)
Nilgiri Fm
(Ordovician)
Sombre Fm
(Silurien)
0
2
4
6
8
10
12
Distance (km)
3
4
5
6
7
8
Elevation (km)

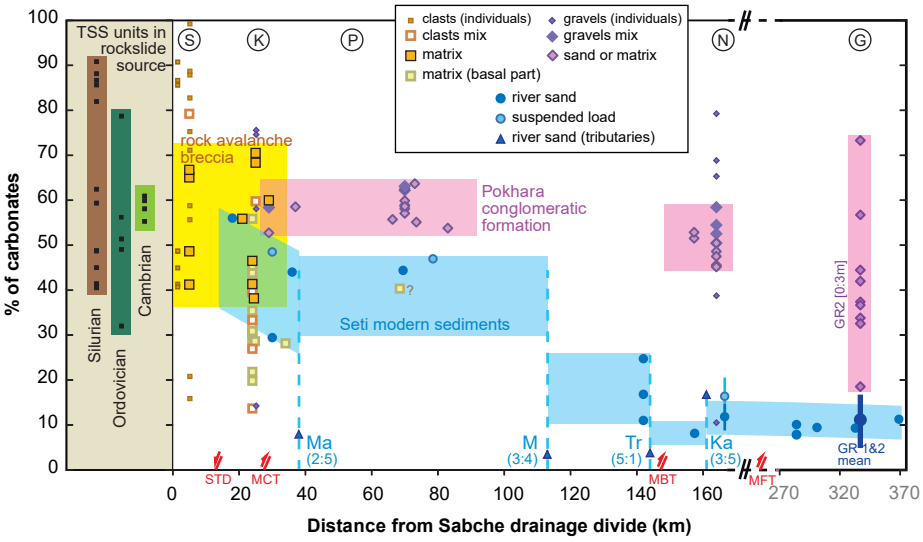
clasts (individuals)
clasts mix
matrix
matrix (basal part)
gravels (individuals)
gravels mix
sand or matrix
river sand
suspended load
river sand (tributaries)
TSS units in rockslide source
Silurian
Ordovician
Cambrian
rock avalanche breccia
Pokhara conglomeratic formation
Seti modern sediments
GR2 [0:3m]
GR1&2 mean
Ma (2:5)
M (3:4)
Tr (5:1)
Ka (3:5)
STD
MCT
MBT
MFT
S
K
P
N
G
% of carbonates
Distance from Sabche drainage divide (km)

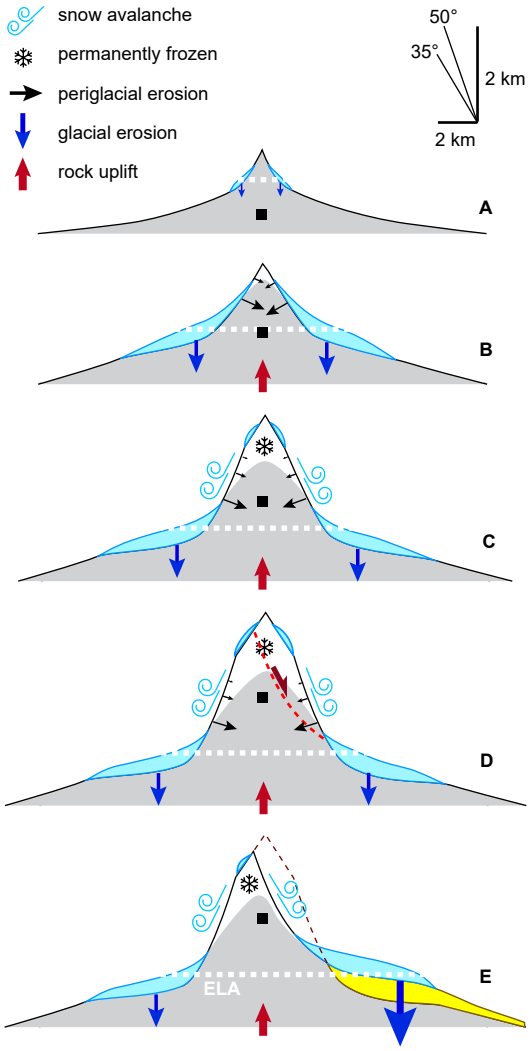
snow avalanche
permanently frozen
periglacial erosion
glacial erosion
rock uplift
50°
35°
2 km
2 km
A
B
C
D
E
ELA

Methods

^{14}C dating

16 organic fragments were collected from 3 distinct areas for ^{14}C dating: 7 wood-fragments samples taken in the breccia deposit at Karuwa (K site on fig.1), 8 samples of charcoal and wood fragments in the southern part of the Pokhara basin (P site), and one micro-charcoal sample found in Pokhara type sediments outcropping at the range outlet (site N in Fig. 1b).

Organic fragment preparation includes standard cleaning and ABA treatment, and combustion at 850°C as described in ref.51. The CO_2 was converted to graphite and analysed on the LMC14 AMS facility[52] "ARTEMIS'', except for one sample prepared and analysed at the National Ocean Sciences Accelerator Mass Spectrometry (NOSAMS) facility at the Woods Hole Oceanographic Institution.

Radiocarbon ages are calculated[53] by correcting the fractionation with the $\delta^{13}C$ calculated from the $^{13}C/^{12}C$ ratio measured on ARTEMIS. We used the IntCal13 curve[54] for calibrating our ^{14}C ages to calendar years using Oxcal online calculator (https://c14.arch.ox.ac.uk/oxcal/OxCal.html) (Supp. Info. table SI-10-1).

^{36}Cl exposure age dating

We sampled plurimetric blocks of Siluro-Devonian black shale and calcschists, deposited on top of the main northern remnant of the original Sabche breccia surface. Samples were prepared at the CEREGE (Aix-en-Provence, France), following standard procedures[55,56]. ^{36}Cl and Cl concentrations were obtained on each sample by isotope dilution accelerator mass spectrometry at ASTER-CEREGE. Major and trace elements were measured at the French National facility for geochemical analysis (SARM-CRPG) (Supp. Info. table SI-11-3).

^{36}Cl production rate was calculated according to concentration in target elements (Supp. Info. table SI-11-2) and Lal/Stone time-dependent scaling using Chronus Online calculator (http://hess.ess.washington.edu/math/index_dev.html). Several blocks made of finely schistosed rocks show evidence of frost cracking and physical weathering, but the shape of the original surface is generally still identifiable and indicates a maximum surface erosion of ~10cm (Supp. Info. table SI-11-1). An additional correction for snow shielding was considered from snow cover measurements on the Himalayan southern flanks 25km to the east[57]. Snow and erosion corrections represent ~25 and 40 yr respectively.

Infra-red stimulated luminescence (IRSL) dating on sheared breccia deposits

TSS carbonate units may contain small amounts of quartz and feldspar grains. The luminescence signal can be reset (called triboluminescence) by heating, mechanical crushing or shearing[35] processes in intense sheared bands such as frictionnites. In the southern part of the rockslide deposit, we collected three samples from two sites approximately ~50 m apart within an internal basal shear zone (CA-13-273, -274, and CA-13-283); Extended Data Fig. 6). Collected samples measured 15x12x7cm and 7x7x5cm respectively. Sample preparation followed the procedure

described in ref.58 to isolate K-feldspar fraction. Bulk samples were sent to Actlabs or SARM-CRPG for major and trace element analysis, used to estimate (see Supp. Info. SI-12 for full details) the total dose rate with the online Dose Rate and Age Calculator[59].

Luminescence measurements have been performed at the University of Lausanne (Switzerland) using a post-IR IRSL protocol[60] at 50°C (IR50) and 225°C (pIR225), as described in the Supp. Info. SI-12. Dose-equivalent distributions were statistically analysed[61] using the Central Age Model (CAM), and also the Minimum Age Model (MAM) for sample CA-13-283 which best represent luminescence reset during shearing (Extended Data Fig. 6). Final ages were calculated with individual fading corrections[62].

Volume of the rockslide deposit

To calculate the total volume of the initial rock-avalanche deposit in the Sabche cirque and the upper Seti (fig. 3), we consider the difference between the initial surface of the breccia deposit and the original topographies of the cirque bottom and upper Seti valley before the collapse (Extended Data Fig. 4).

The original cirque surface is based on the recognition from air views and satellite images of the outcropping substrate areas beneath the deposits (Fig. 1 and Extended Data Fig. 4a). These outcrops spread outwards from near the cirque centre (and after removing the ice cover in the NE part of the cirque) and permit a rough interpolation of a smoothed initial surface. It is difficult to assess the second order relief (mostly small ridges separating glacier streams, considering by equivalence the cirque of the Annapurna Sanctuary located just west of that of Sabche). Introducing an a priori moderate relief carved by glaciers suggests an uncertainty on the volume reconstruction of the order of +3/-2 km^3. Based also on observations made in the Annapurna Sanctuary cirque, the volume of moraines and ice that could have been entrained by the rock avalanche was estimated to be <0.1 and 0.5 km^3, respectively.

The initial top surface of the rockslide deposit has been estimated based on a few remnants in the northern and north-western parts of the cirque (Extended Data Figs. 4b, 5a) and on top of the ridge along its southern part (Extended Data Fig. 2f). These surfaces are all located at an altitude of ~4600m, but are not sufficient to constrain the geometry of the deposit surface in its central part, where the breccia penitents left by erosion provide only a minimum elevation (Fig. SI-4-1c). Nevertheless, literature evidence from the geometry of large collapses characterized by frontal confinement, as the Sabche one, suggest that this central part was likely at an elevation above 4600 m (Supp. Info. SI-4). The present course of the glacier descending from the Annapurna III, which has been diverted westward, requires also the presence of an initially convex surface of the rock-avalanche deposit (Fig. 1). Despite uncertainties related to secondary hummocky features, a central convexity or a downward transition between the cirque and the Upper Seti valley, the mean rock-avalanche surface can presumably be approximated by a nearly horizontal deposit at an elevation of ~4600 m (Extended Data Fig.4b). We estimate that these uncertainties affect the reconstruction of the breccia volume by an error of 2-3 km^3 (Supp. Info. Fig. SI-4).

Along the upper Seti, a similar approach was used to estimate the breccia volume, assuming, for the rock-avalanche deposits' original surface, a progressive thickness decrease along the upper Seti valley down to the last breccia occurrence (Supp. Info. Fig. SI-1-1) and relying on the minimum thickness indicated by the relic breccia spurs.

The combination (mean squared error) of the different sources of error on the basal and summit surfaces of the breccia deposit results in a final uncertainty in the volume reconstruction of +4/-3 km^3.

Finally, to derive the volume of solid rock that collapsed from the Annapurna IV summit, the breccia deposit volume was corrected for breccia porosity, measured from various rockslide breccia sampled in the Annapurna region (Supp. Info. SI-5). An average value of 15±5% was found, consistent with previous estimates on rock-avalanche material[63].

Original failure surface of the Sabche rockslide

The entire NE and NNE area of the Sabche cirque displays numerous structural surfaces related to stratification or schistosity, and oriented at N110° (Extended Data Fig. 1). The eastern part of the ridge joining the Annapurnas-III and -IV (Fig. 3) shows large structural slabs with dips of ~45° to the south, i.e., quite well-oriented to represent slip planes. Below the Annapurna IV, the cliffs are characterized by geometric breaks (prisms, dihedrals) that connect these structural surfaces to irregular surfaces oriented at ~N0°. In contrast with slopes that dominate the western or eastern sides of cirque, these cliffs do not display any obvious trace of glacial or avalanche erosion, i.e. any trace of channelizing forms. This absence suggests that their surfaces were created by recent fracturing, and most probably correspond to the rockslide failure surface.

To corroborate these observations in a more objective way and to draw the a priori extension of the failure surface, a morphological criterion is defined by looking at the transverse curvature (Extended Data Fig. 4d) of the high-resolution topography (2-m Pleiades tri-stereo-derived DTM, see realization details in Supp. Info. SI-3), excluding ice and snow-pack areas. The structural surface appears with minimal curvature, whereas the slopes affected by erosion display converging thalwegs underlined by negative curvature. Using these indicators, we identified a zone of "fresh" planar or prismatic surfaces just south and west of the Annapurna IV summit, distinct from the areas beyond where erosion has begun to carve out channelized or converging relief. This first area (the upper and lateral limits of which are represented by the pink line in Fig.1c and Extended Data Figs 1-4) is considered as delimiting the original failure surface of the rockslide.

Even if we cannot exclude the possibility that small/secondary rock slides or rock falls would have partly rejuvenated this surface, analogous to the May 5th 2012 rockslide event[64] at the SE end of the Annapurna IV, the absence of deposits on top of the northern remnant of the original surface (Extended Data Fig. 5) suggests that no major reshaping event has affected the initial failure surface.

Paleo-Summit Reconstruction

To reconstruct the paleo-summit, three constrains must be verified: first, the restored rock volume must equal the collapsed one, i.e. $23^{+3.5}/_{-3}km^3$; second, the paleo-topography has to be on the verge of collapse; and third, the slopes and cliffs below the paleo-summit must be mechanically stable, otherwise they would have failed before the giant mass through smaller rockslides. The failure surface follows large portions of structural surfaces associated with the local schistosity developed in marly limestone and possibly presenting lower cohesion and friction angles. Defining a Safety Factor (SF) associated with this failure plane is difficult in absence of specific

measurements on these planes, and because of uncertainties on the exact geometry of the most basal part of the failure surface (below modern glaciers and debris). Other than mass conservation, the restoration therefore relies only on cliff average stability.

Mechanical characteristics of the Annapurna range substratum

To check the stability of headwalls below the paleo-summit, we explored the average mechanical rock properties that ensure the stability of the regional relief in the entire high Annapurna range. Estimating the average material properties of a region can be done by considering the best-fitting strength parameters that reproduce the frequency-area distribution of landslides[47]. Here, in the absence of such a landslide distribution in the Annapurna region, we instead estimate the stability of the Annapurna summits by exploring the maximum value for the cohesion that allows the stability of all regional slopes. At this scale, testing slope stability through complex numerical approaches is computationally too demanding, and simplified limit *equilibrium* analysis, despite its limitations, is usually preferred[65,66].

In order to calculate the spatial distribution of the Safety Factor (SF) in the Annapurna region, we have developed a Matlab© code largely adapted from previous approaches[66]. The slope stability analysis is based on the limit equilibrium concept for a 3D model with rotational movement on a potential ellipsoidal slip surface.

At each topographic grid point, our model evaluates the slope stability conditions for a large number of randomly selected ellipsoidal slip surfaces (Extended data Fig. 7). These are defined by the geographic coordinates of the centre, the length of their three half-axes a, b and c, by their orientation α in the direction of the steepest topographic slope β_0 and inclination β that follows the steepest slope plus or minus 15°, and by an offset of the ellipsoid centre above the terrain z_c. For each failure surface, the SF is computed using the 3-D sliding surface Hovland's model[67]:

$$SF = \frac{\sum_{slip\ surface} C.A_{(x,y)} + \rho g D_{(x,y)} \cos(\beta_c) tan(\varphi_c)}{\sum_{slip\ surface} \rho g D_{(x,y)} \sin(\beta_m)} \quad (1)$$

with $\beta_m = tan^{-1}(\tan(\beta_c).\cos(\alpha_c - \alpha))$, and $A_{(x,y)} = \frac{1}{\cos(\beta_c)}$

where the summation sign corresponds to the pixel summation of the resisting and driving forces (projected on each surface element) applied on each vertical rock column of thickness D, and A is the 3-D area of the slip surface for the considered pixel, ρ the rock density, C the apparent cohesion of the substrate, φ its internal friction angle, β_c and α_c the local slope and aspect of the surface of rupture at the base of the considered column. The driving force and sliding act in the direction of α. β_m is the apparent dip of the slip surface at the considered column in the direction of sliding. No inter-column forces or external forces, such as seismic loading, are considered in the model.

In contrast with a previous model[66], and because soil is absent above 4500m, we don't consider potential slip at the soil-substratum interface, but assume a homogeneous substratum. Because we are not interested in exact friction and cohesion values, but only by apparent regional values that could be applied to the slopes of the Annapurna IV, we do not consider either seepage forces, or pore pressure effects.

Practically (Extended Data Fig. 7), we employ a brute force procedure by exploring at regular steps different parameters. First, we iterate on the pixels of the topography. For each pixel,

we iterate between the extreme geometric limits of the ground trace, calculating the average aspect and steepest slope over the given scale. For each explored ground window, we iterate on the parameters (a, b, c and β) of the ellipsoids that fit the ground trace and calculate the SF (failure surfaces displaying an overhanging portion are rejected). For each pixel, the parameters giving the minimum SF value are retained and the associated potential rockslide is located at the coordinates of its center of mass. Finally, in the result grid, if a pixel contains several centres of mass of potential rockslides, we keep only the one with the lowest SF.

Before applying our model to the glaciated Annapurna area or to the fluvially-dominated region farther south (Supp. Info. SI-6), we tested it on a benchmark case and ensured that the searching procedure was finding: (1) similar solution (SF value) as previous studies[65,66]; and (2) optimal ellipsoidal failure geometries not too far from the semi-analytic circular[68] or log-spiral[69] solutions. Regarding this later point, our optimal surfaces are a bit more concave than the semi-analytic solutions, but the SF values match to within <10%.

To explore the mechanic stability of the Annapurna range, we consider the steep areas within similar elevation range and lithology as the Annapurna IV collapse, i.e., for elevations higher than ~4000 m and for TSS units, excluding the flat cirque bottom (Extended Data Fig. 8). For the SF calculation, a fixed value of the internal friction angle at φ=35° (ref. [70]) is considered. Only cohesion values were varied. For each cohesion value, we plot the distribution of SF values. If most prominent cliffs are near the verge of failure as expected in mountains with both high uplift and high erosion[16], then the distribution mode has to be slightly above the critical value of 1, i.e. for an apparent cohesion ≥1MPa for the high relief of the Annapurna range.

Locally, the geometry of gravity instabilities is most often related to the orientation of fracture families and/or to schistosity: at the scale of our approach, such a consideration of local factors is not possible, and the explored cohesion value should be viewed as an average estimate. In addition, as neither the effects of pore pressure, seepage forces, nor seismic acceleration are taken into account, this value can be seen as a minimum[46] for the glaciated relief of the Annapurnas. More importantly, because the internal friction angle has not been explored, the cohesion values tested in our procedure must be viewed as an apparent value. However, the precise value is of little importance insofar as we are looking for a relative criterion to test realistic topographies of the paleo-Annapurna IV in a second step (Supp. Info. SI-7), or to compare apparent cohesion values between glaciated and unglaciated areas (Supp. Info. SI-6).

Paleo-topographic reconstruction

To explore a family of possible geometries for the Annapurna IV paleo-summit, we generated 2000 topographies from fixed ground support points along the northern ridge and from random paths for the crest and the southern basal footprints (see also computing chart in Supp. Info. SI-7). Whereas the elevation of the southern basal footprints is interpolated from the initial cirque surface (Extended Data Fig. 4a), the crestline elevation is randomly varied within a fixed range (the northern slopes between the present head scarp and the crest are allowed to vary between 35 and 50°, whereas the horizontal path is oriented in continuity with the present ridgelines at their eastern and western terminations). Intermediate points with randomly varying elevations are also generated before performing surface interpolation and volume calculation.

To consider a paleo-topography as acceptable, besides producing a rockslide volume between 20 and 26.5km^3, its hillslopes must be stable according to the SF criterion defined for the Annapurna region. For each randomly generated paleo-topography, we thus apply the same procedure described in the previous section (Extended Data Fig. 7), and derive the distribution of minimal SF values. For the high relief of the Annapurnas and assuming $\varphi = 35°$, all SF values were found to be >=1 for a cohesion value C=2MPa. Based on this absolute cut-off, any paleo-topography presenting SF values lower than unity for C=2MPa were rejected. From the final set of acceptable geometries, we calculate a mean topography, a distribution of volumes, of crest profiles and of paleo-summit elevations (Fig. 3d and Extended Data Fig.9).

It should be noted that for the modelled paleo-topographies the optimal ellipsoidal failures predict a steeper and shallower rupture surface than that actually observed and preserved in the present topography beneath Annapurna IV. Applying Hovland formula[67] (eq. (1)) on the actual failure surface, and exploring various sliding directions in order to reach a minimal stability, leads to SF_{fs} values of 1.42±0.1 for C=2MPa (vertical red line in Extended Data Fig. 9g), well above the collapsing threshold of 1. Although this high value results in part from the surface roughness compared to that of a smooth ellipsoid, it also reflects the likelihood that the rupture was strongly guided by existing schistosity planes, especially in the western part of the collapse. It is hypothesized that these schistosity planes exhibit friction angles and cohesion significantly lower than 35° and 1-2MPa, respectively. Nevertheless, if we attempt to reduce the set of possible paleo-topographies, we could potentially add a third criterion that the SF_{fs} along the failure surface has to be minimal or not too high: we might, therefore, preferentially select a subset of paleo-topographies with $SF_{fs} \leq 1.42$ (for C=2MPa), which would be more prone to collapse (dark red histogram in Fig. 3d).

Methods and Extended Data references:

51. Dumoulin J.P. et al., 2017. Status report on sample preparation protocols developed at the LMC14 Laboratory, Saclay, France: from sample collection to 14C AMS measurement. Radiocarbon 59, 713-726.
52. Moreau, C., Caffy, I., Comby, C., Delqué-Količ, E., Dumoulin, J.-P., Hain, S., Quiles, A., Setti, V., Souprayen, C., Thellier, B., et al. (2013). Research and Development of the Artemis 14C AMS Facility: Status Report. Radiocarbon; Vol 55, No 2–3 (2013).
53. Mook, W. G., & Van Der Plicht, J. (1999). Reporting 14C activities and concentrations. *Radiocarbon*, *41*(3), 227-239.
54. Reimer, P. J., Bard, E., Bayliss, A., Beck, J. W., Blackwell, P. G., Ramsey, C. B., ... & Van Der Plicht, J. (2013). IntCal13 and Marine13 radiocarbon age calibration curves 0–50,000 years cal BP. *radiocarbon*, *55*(4), 1869-1887.
55. Stone, J. O., Allan, G. L., Fifield, L. K., & Cresswell, R. G. (1996). Cosmogenic chlorine-36 from calcium spallation. *Geochimica et Cosmochimica Acta*, *60*(4), 679-692.
56. Schlagenhauf, A., Gaudemer, Y., Benedetti, L., Manighetti, I., Palumbo, L., Schimmelpfennig, I., ... & Pou, K. (2010). Using in situ Chlorine-36 cosmonuclide to recover past earthquake histories on limestone normal fault scarps: a reappraisal of methodology and interpretations. *Geophysical Journal International*, *182*(1), 36-72.
57. Putkonen, J.K., 2004.Continuous snow and rain data at 500 to 4400 m altitude. Arct.Antarct. Alp. Res. 36 (2), 244–248
58. Diaz, N., King, G.E., Valla, P.G., Herman, F. & Verrecchia, E., 2016: Pedogenic carbonate nodules as soils time archives: challenges and investigations related to OSL dating. Quat. Geochronol. 36, 120-133.
59. Durcan, J.A., King, G.E. & Duller, G.A.T. 2015: DRAC: Dose Rate and Age Calculator for trapped charge dating. Quaternary Geochronology 28, 54–61.
60. Buylaert, J.P., Murray, A.S., Thomsen, K.J. & Jain, M. 2009: Testing the potential of an elevated temperature IRSL signal from K-feldspar. Radiation Measurements 44, 560–565.
61. Galbraith, R.F., Roberts, R.G., Laslett, G.M., Yoshida, H. & Olley, J.M., 1999: Optical dating of single and multiple grains of quartz from jinmium rock shelter, northern Australia: part i, experimental design and statistical models. Archaeometry 2, 339-364.
62. Huntley, D.J. & Lamothe, M. 2011: Ubiquity of anomalous fading in K-feldspars and the measurement and correction for it in optical dating. Canadian Journal of Earth Sciences 38, 1093–1106.
63. Govi, Gula & Nicoletti, (2002), Val Pola rock avalanche of July 28, 1987, in Valtellina (Central Italian Alps), in Catastrophic Landslides: Effects, Occurrence, and Mechanisms GSA rev.in Engineering Geology, 15.)
64. Oi, H., Higaki, D., Yagi, H., Usuki, N., & Yoshino, K. (2014). Report of the investigation of the flood disaster that occurred on May 5, 2012 along the Seti River in Nepal. *International Journal of Erosion Control Engineering*, *7*(4), 111-117.
65. Xie, M., Esaki, T., Qiu, C., & Wang, C. Geographical information system-based computational implementation and application of spatial three-dimensional slope stability analysis. *Computers and Geotechnics*, 33(4-5), 260-274 (2006).

66. Mergili, M., Marchesini, I., Rossi, M., Guzzetti, F., & Fellin, W. (2014). Spatially distributed three-dimensional slope stability modelling in a raster GIS. *Geomorphology*, *206*, 178-195.
67. Hovland, H. J. (1977). Three-dimensional slope stability analysis method. *Journal of the Geotechnical Engineering Division*, *103*(9), 971-986.
68. Hungr, O., Salgado, F.M., Byrne, P.M., 1989. Evaluation of a three-dimensional method of slope stability analysis. Can. Geotech. J. 26, 679–686.
69. Leshchinsky, D., Baker, R., & Silver, M. L. (1985). Three dimensional analysis of slope stability. *International Journal for Numerical and Analytical Methods in Geomechanics*, *9*(3), 199-223.
70. Byerlee, J. (1978). Friction of rocks. In *Rock friction and earthquake prediction* (pp. 615-626). Birkhäuser, Basel.
71. Parsons, A. J., Law, R. D., Searle, M. P., Phillips, R. J., & Lloyd, G. E. (2016). Geology of the Dhaulagiri-Annapurna-Manaslu Himalaya, Western Region, Nepal. 1: 200,000. *Journal of Maps*, *12*(1), 100-110.
72. Morin, G. (2015). L'érosion et l'altération en Himalaya et leur évolution depuis le tardi-pléistocène: analyse des processus d'érosion à partir de sédiments de rivière actuels et passés au Népal central (Doctoral dissertation, Université de Lorraine).

Extended Data Figure Legends

Extended Data Fig. 1: Geologic map and cross section of the Sabche cirque area. (Upper) Interpretative geologic map of the Sabche cirque area based on published maps[28,71] West and North of the cirque. The TSS units that outcrop along those cliffs correspond to the base of the TSS series, namely carbonate-rich sediments, Cambrian to Silurian in age, and presenting an upward decreasing degree of metamorphism[28]. The different lithologic limits were extrapolated across the cirque based according to our observations made on photos taken from ultralight aeroplane and helicopter, and from satellite images. Structures and bedding attitudes were also estimated from photos or from the tri-stereo DEM. (Lower) Interpretative structural cross section AA' (see location on main map) built according to published sections further West[28,71] and to the bedding attitude we estimated from a large set of airplane photos or from the DEM. The northern part of the section, which has been affected by the rockslide, is relatively well constrained since bedding are pretty well identifiable on photos. The southern part is much less constrained because the Sanctuary units display less identifiable beddings and because the structure is much more heckled with numerous small-scale folding. STD = South Tibetan Detachment, DD = Deodali detachment.

Extended Data Fig. 2: Different facies of the breccia deposit in Sabche cirque (photos a to f = taken from an ultra-light aeroplane _ See pictures location on fig. 1 in Supp. Info.): (a) compact, homogeneous, pulverized and indurated fine grained breccia exposed over ~200 m high cliffs; (b) and (c) package of coarse and blocky material topped by more finely pulverized fine grained breccia material; (c) and (d) Internal contacts between grey and yellowish breccia facies (issued from the Annapurna Yellow Limestone formation[28]) presenting inverted order and suggesting limited mixing during the rockslide collapse; (d) Contact close to the southern base of the cirque deposit in its southern part: this contact, slightly sloping towards the N or NW, presents as a thin band of shearing and micro-crushing where IRSL samples were taken (CA-273, -274 and -283). (e) Rare preserved phantom of limestone dismantled strata, or jigsaw facies. (f) In the southern part of the cirque, veneers of breccia deposit are preserved on the N-dipping flank of the cirque up to 4350m altitude (z2), and at the top of the eastern ridge of Macchapuchare (fig. 1) at ~4570m altitude (z1 = satellite image taken on 30/12/2011); (g) Saw-cut samples of compact and indurated facies exposed in the basal part of the deposit (CA-273, site of panel d): the breccia is made of finely crushed material with a few angular clasts.

Extended Data Fig. 3*:* Outcrops near Karuwa (site K on fig. 1) exposing the stratigraphy of the granular avalanche breccia deposit.
(a) 40-m-high cliff overhanging the Seti river, exposing breccia of the granular avalanche material and cut by a small inset terrace capped by a filling of (b) finely-layered limestone rich gravels of Pokhara conglomerates. (c) Breccia facies with juxtaposition of parts made of limestone/marble of different colors with pockets of whitish elements and matrix within a set of darker elements and matrix. The size of elements, the proportion of clast *vs.* matrix, as well as the carbonate content remain however similar between the different colored areas. They are interpreted as figure of incomplete mixing at meter-scale of the avalanche material issued from the basal Ordovician units

that display alternation of light and dark layers in the Sabche cirque along the steep SW face of the Annapurna IV (c'). (d) Internal part of the breccia displaying dyke injection of a fluid rich phase that coloured the breccia, and the post-injection (e) multiple brittle to ductile faulting and shearing of this dyke and of its shoulders. (f) Schematic section of the contact between the avalanche brecciatic deposit and the gneissic bedrock of the Seti valley flanks. This contact displays a transition in terms of lithology and clast size: breccia with large (up to >1m) and sub-angular to rounded boulders of local biotitic gneisses are progressively replaced by smaller angular elements (<30cm) within a matrix-dominant material made of ~100% of TSS lithologies. The gneiss rich unit, which corresponds to local material dragged and entrained at the base of the avalanche, contained quantity of millimetric to sub-metric pieces of vegetal debris (root, branch and trunk (g)) ripped from the sides of the valley, and whose density decreases also rapidly away from the former valley wall. (h) Bedrock/breccia contact in the upper part of the talweg displaying a contact zone, 0 to 40-cm thick, made of a mixture between limestone breccia, local gneissic clasts, and paleosol pockets, including numerous wood debris, and the presence of a (i) shearing zone of a few centimetres thickness. Green numerical codes correspond to the names of the samples (CA-xx-xx) dated by ^{14}C.

Extended Data Fig. 4: Elements for reconstructing the volume of collapsed rockslide material in the Sabche cirque and the initial rockslide failure surface. Maps of the base (a) and top (b) of the rock avalanche brecciated deposits, including the interpolation constraints, and (c) present-day residual thickness of the breccia deposits. (d) Sabche rockslide scar identification from the transverse curvature (m^{-1}) computed from the high resolution (2-m pixel) topography. The recent scar surface (3 and 4) is characterized by step like dihedrals that delineate planar faces with low curvature along the stratification/foliation planes and irregular faces following a set of fractures at 90°. In contrast, outside the scar (1 and 2), the topography displays the first marks of erosion and gullies organisation toward a converging network.

Extended Data Fig. 5: The main dated relic of the rockslide deposit surface in the upper Sabche cirque

(a) Satellite image (Google Earth) of a large flat area in the northern part of the Sabche cirque. This flat area corresponds to the top of the rockslide deposit (4600m), which was amply resurfaced by glaciers except along its southern part where the original surface is covered with numerous multi-metric blocks. (b) Picture taken from an ultra-light aeroplane of the area, south of which the multi-meter blocks CA-13-260 to 265 were sampled. (A: original chaotic upper surface of the rockslide deposit; B: gently hilly surface of the hummocky moraine deposits; C: crested moraine left by the glacier issued from the South-Eastern face of the Annapurna III and which is now deeply entrenched into the breccia deposit; D: recent moraine left by the glacier issued from the West face of the Annapurna IV; E: present-day glacier issued from the West face of the Annapurna IV). (c) Five of the six blocks sampled for cosmogenic ^{36}Cl dating at the top of this relic surface. All the blocks of the surface consist of carbonate rocks: limestone, marly to sandstone limestone, sandstone marl. These lithologies are finely schistosed and their surface physically weathered.

Extended Data Fig. 6: Internal shear zone near the basal part of the rockslide deposit in the Sabche cirque and IRSL dating (see location on Fig. 1C**)**. (a) The shear zone varies in thickness from a few centimetres up to 30cm at the level of fish-like structures (to the left of the hammer). (b) The shear zone (sample CA-13-283) appears as colored bands of relatively compact breccia made of centimeter size angular clast within a finer yellowish matrix; (c & d) Thin sections observed under polarizing microscope, cut into the shear zone perpendicularly to the shearing plane and showing thin zones of homogeneous finely fragmented almost glassy material within microbreccia facies with locally remnant of larger clasts. (e) Schematic sedimentologic description of the breccia around shear zone at 2 sites, around 50m apart (Extended Data Fig. 2d). (f and g) Age distributions (fading-corrected) and kernel density estimate (KDE) plots for samples CA-13-283 and -273 respectively. IR50 ages and KDE are represented by filled circles and thick line, respectively. pIR225 ages and KDE are represented by open circles and dashed line, respectively.

Extended Data Fig. 7: Definition and validation testing of the hillslope safety factor (SF) exploration procedure in the Annapurna Range region. (a) Definition of the variables for the computation of the Safety Factor (SF) according to 3D-Hovland criterion[67], and (b) computation chart of the searching procedure of the ellipsoid-type failure surfaces that minimize the SF all over the topography of a given region. (c) Validation test of the searching procedure in the case of a topographic step, 1-m high, dipping at 60° with $\varphi = 15°$ and $C = 0.116$ Pa. The optimal ellipsoids surfaces at the four increments that present minimal SF are compared with close-formed solutions[68,69]. The SF values remain within 5% of the ones associated to these solutions whatever the nominal value (solid line) or the one calculated with 3D-Hovland criterion applied to their geometry (dashed line) is considered.

Extended Data Fig. 8: Results of the hillslope safety factor exploration in the Annapurna Range region. (a) Map of the minimum SF along the hillslopes of the Annapurna high relief found using the systematic searching procedure (Extended Data fig. 7) within the area delineated by the dashed line. Calculation is made for an internal angle of friction of 35° and a cohesion, *C*, of 1.15 MPa. The steepest faces surrounding the highest peaks (black triangles), like the SSE face of the Annapurna I (A-I), one of the most challenging climbing route in High Himalaya, present a Safety Factor lower than 1 and would be considered as unstable for this given cohesion value. Note that for a given pixel, the search procedure may have found several optimal failures, of different sizes, whose centers of mass related to the same pixel: in this case, the failure with the minimum SF was chosen. A-II =Annapurna II, A-III =Annapurna III, A-IV =Annapurna IV, and Ma = Machapuchare. (b) Histograms of the values of the SF for different values of cohesion, *C*, between 0.5 and 2 MPa. For *C*=2MPa, almost all the hillslopes are apparently stable.

Extended Data Fig. 9: Paleo-summit reconstruction

(a) Construction points used to build simplified topography of the paleosummit. This construction is essentially based on two main lines, whose geometry is explored in a random way: the paleocrest (in cyan) and the paleocliff SW base (in blue). These lines are built as the sum of harmonics function (up to the 8th term) of random amplitude and phase. The two extremities of the paleocrest have been chosen to prolong on average the direction of the present crests line further West and East. Similarly, the extremities of the base of the SW cliff and the isolated mobile point (in cyan)

were chosen to prolong the SW-facing cliffs of the Sabche cirque. Densifying points are then added before using Matlab© interpolation function *griddata*. (b) Map extent of the density (in log scale) of the random paths explored for the paleocrest and the paleobase, with one random example of path (black solid line). (c) Same as (b) but for the elevation profile of the paleocrest. In both graphs, purple lines indicate the 95% probability of the density of the a posteriori paths that respect both rockslide volume and hillslope stability constraints. (d) Map and histogram (inset graph) of the SF values obtained through the searching procedure (ED-fig. 7) applied, within dashed lines and for a cohesion value of C=2 MPa, to one of the randomly generated paleotopography. (e) Average shape of the topographies that satisfy rockslide volume and regional stability criterion, including a rose diagram of the optimal sliding direction N245 (i.e. the direction that minimizes the SF on the failure surface). (f) Histogram of the volumes of the collapsed summit explored by the generator of random topographies. 75% of the values fall within the range of the volume estimated for the rockslide. The topographies that satisfy the regional stability criterion are superimposed in pink colour. (g) Histograms of the SF on the failure surface for cohesion values C=2 MPa. The topographies that satisfy the rockslide volume are superimposed in darker colour, and the ones that satisfy both rock volume and regional stability criterion in pink colour.

Extended Data Fig. 10: Possible Sabche rockslide signature in the Gandak fan?

(a) Stratigraphic log and carbonate content of two 50-m long cores, GR1 and GR2, drilled in the Gandak fan[72]. The two boreholes GR1 and GR2 show relatively constant carbonate percentages close to the current river values (represented by the blue and gray lines respectively). Nevertheless, GR2 is characterized by a 25-30% anomaly between -10 and -3m, and by a very strong 35-70% carbonate anomaly between -3m and the surface. This anomaly was corroborated by additional measurements on samples taken in a 3-m-deep small pit dug in the close vicinity of the GR2 drill site. Such a recent anomaly in carbonate content might correspond to deposition of the fine fraction of the sediments issued from the Sabche cirque erosion, 300km further downstream. Whereas these carbonate rich units are not directly dated, ^{14}C ages in GR1 core indicate that they are probably younger than ~1.5 kyr, which is compatible with a deposit related to the Annapurna IV collapse and more or less synchronous of the Pokhara conglomerate deposits.

(b) Residual topography obtained by subtracting a second order polynomial fit (dashed lines = Trend function in ArcGis) to the topography (30m SRTM) of the Narayani fan. This residual topography enables to highlight small topographic variations on the surface of the fan. It is seen that GR1 was drilled in the recent flood plain of the Narayani (in yellow to reddish colors), while GR2 was drilled in a N-S lobe 3 to 5 m higher than the rest of the fan (in bluish colors). This lobe, which was then re-incised on its eastern border by the Narayani (see zoomed image) could have been built during the episode of strong sediment input that followed the collapse in the Sabche cirque.

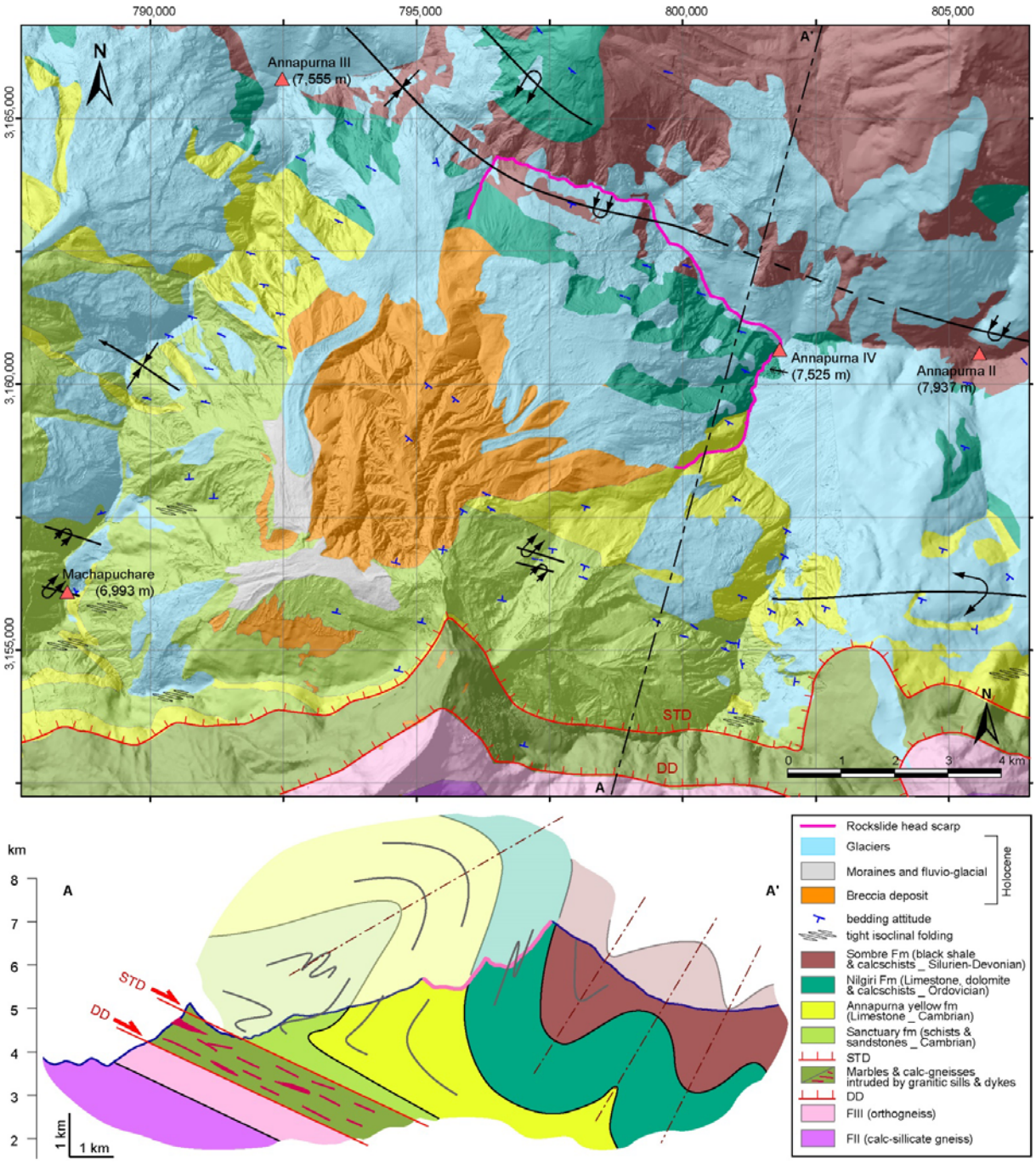

Extended data figure 1

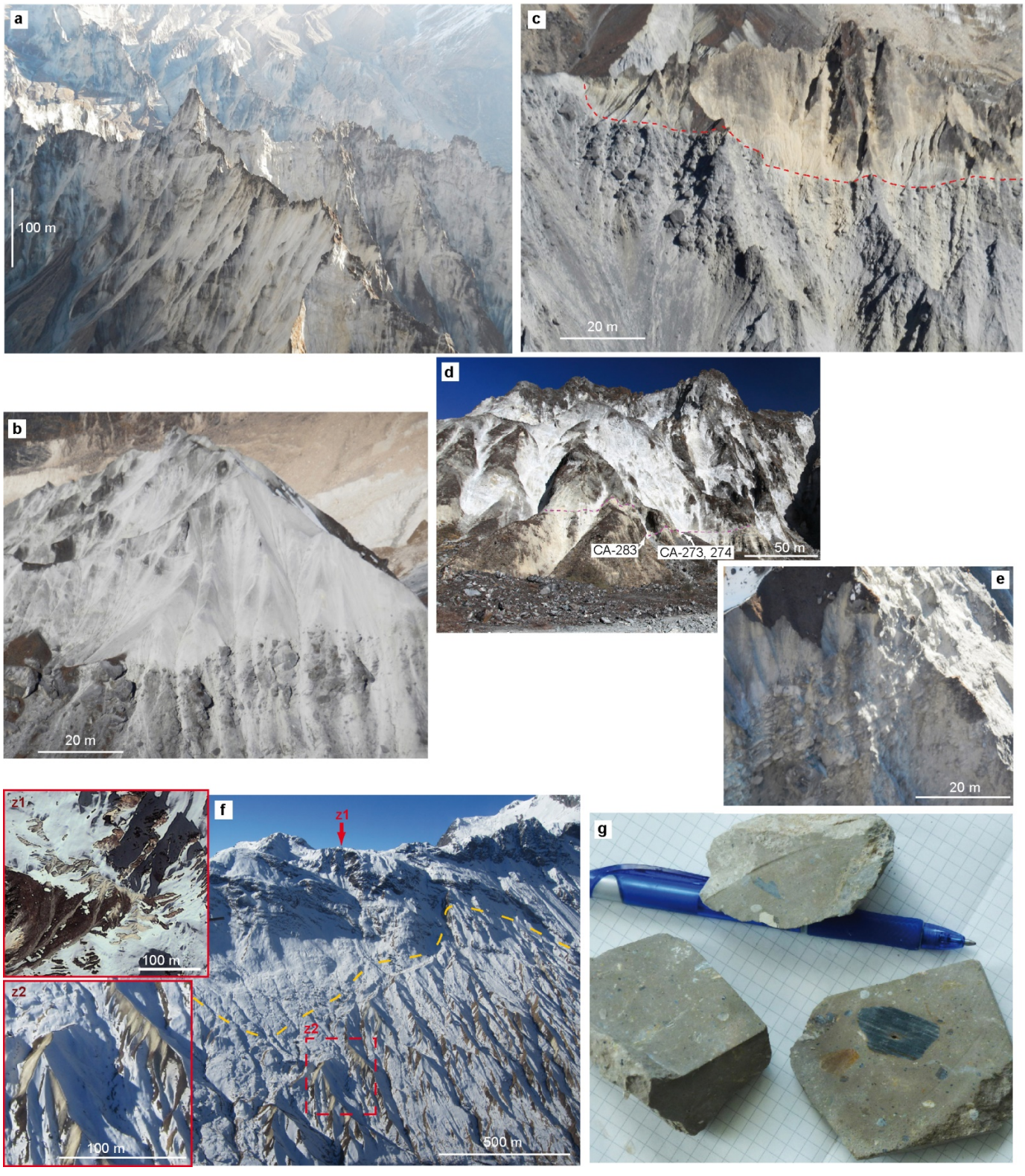

Extended data figure 2

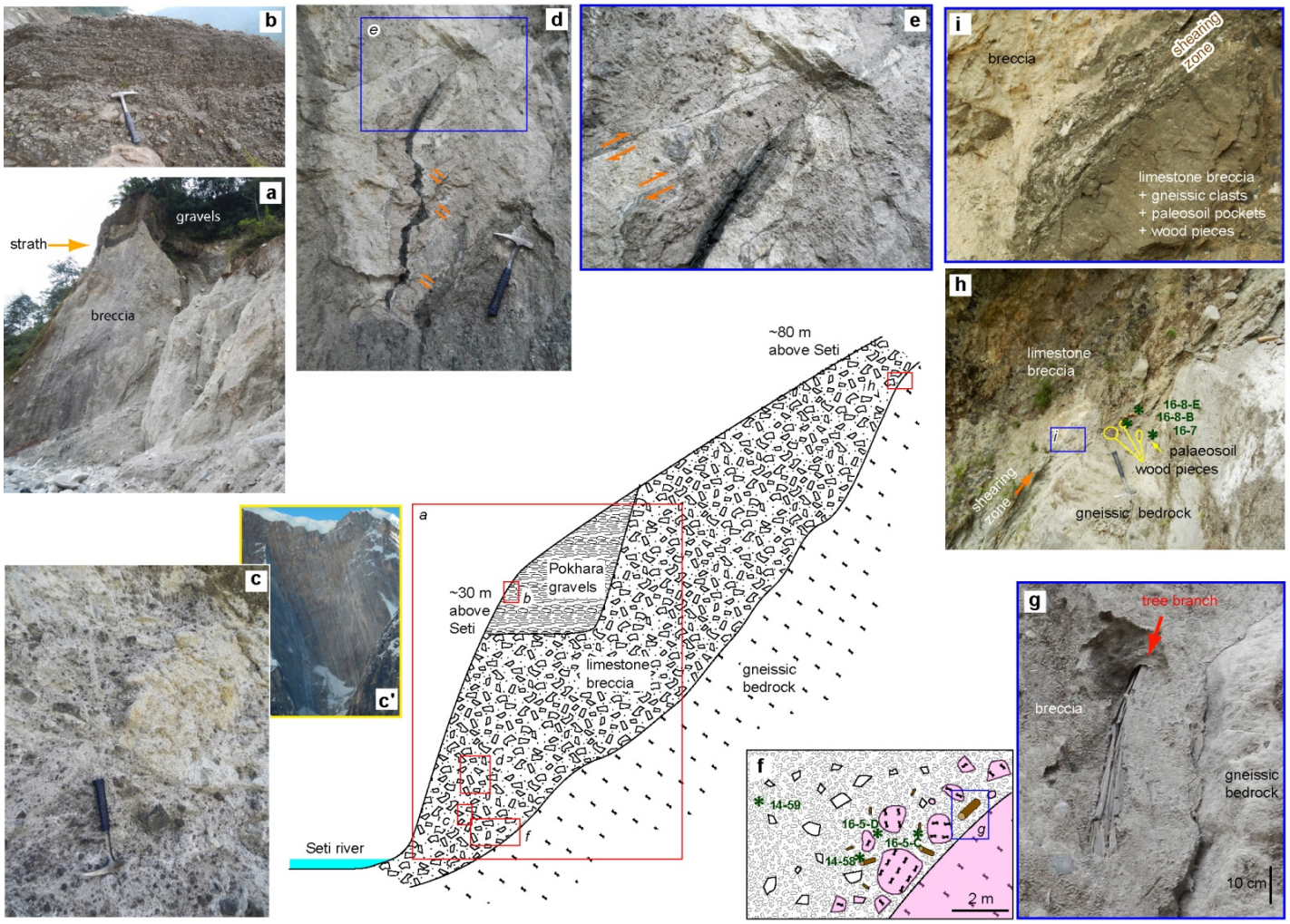

Extended data figure 3

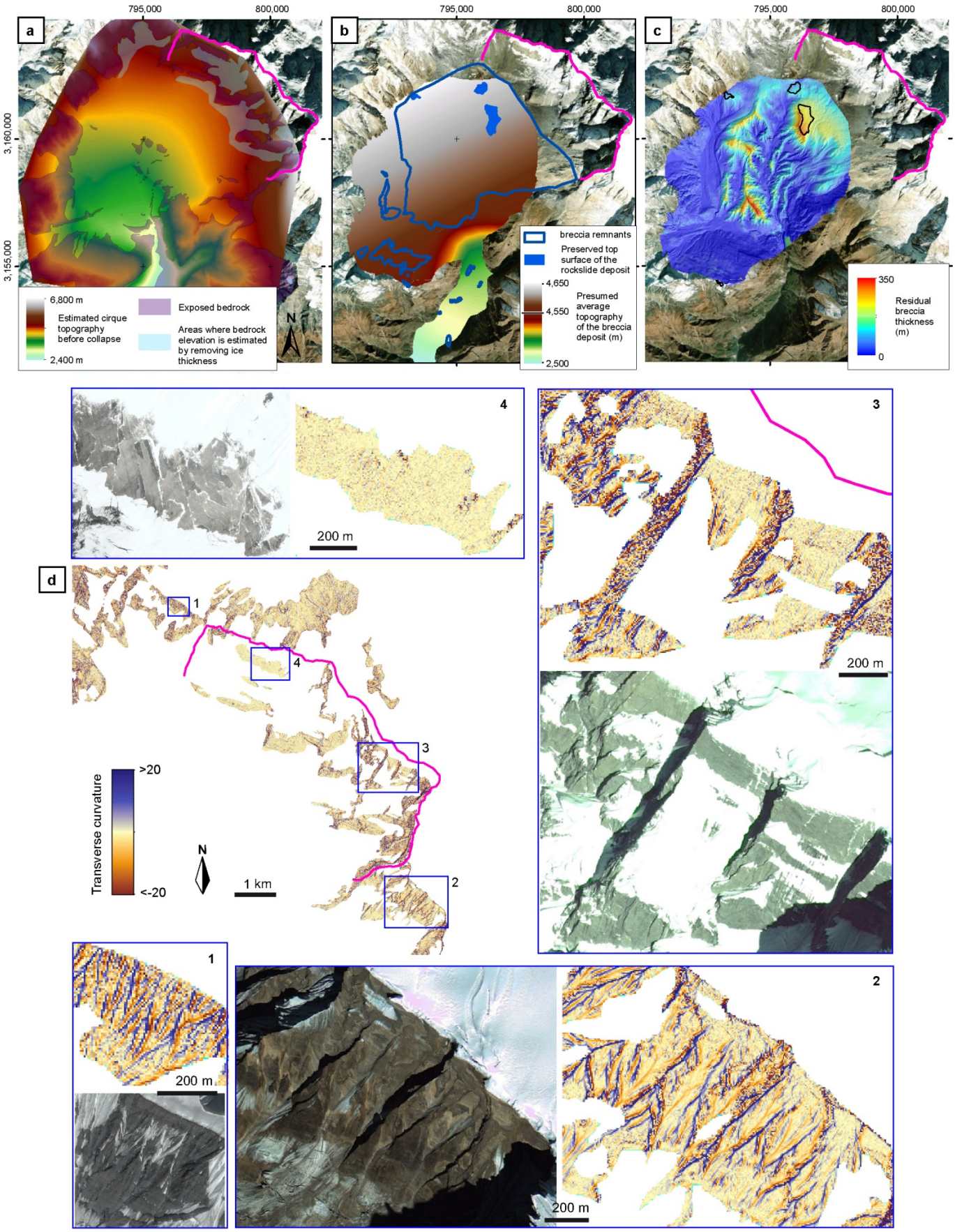

Extended data figure 4

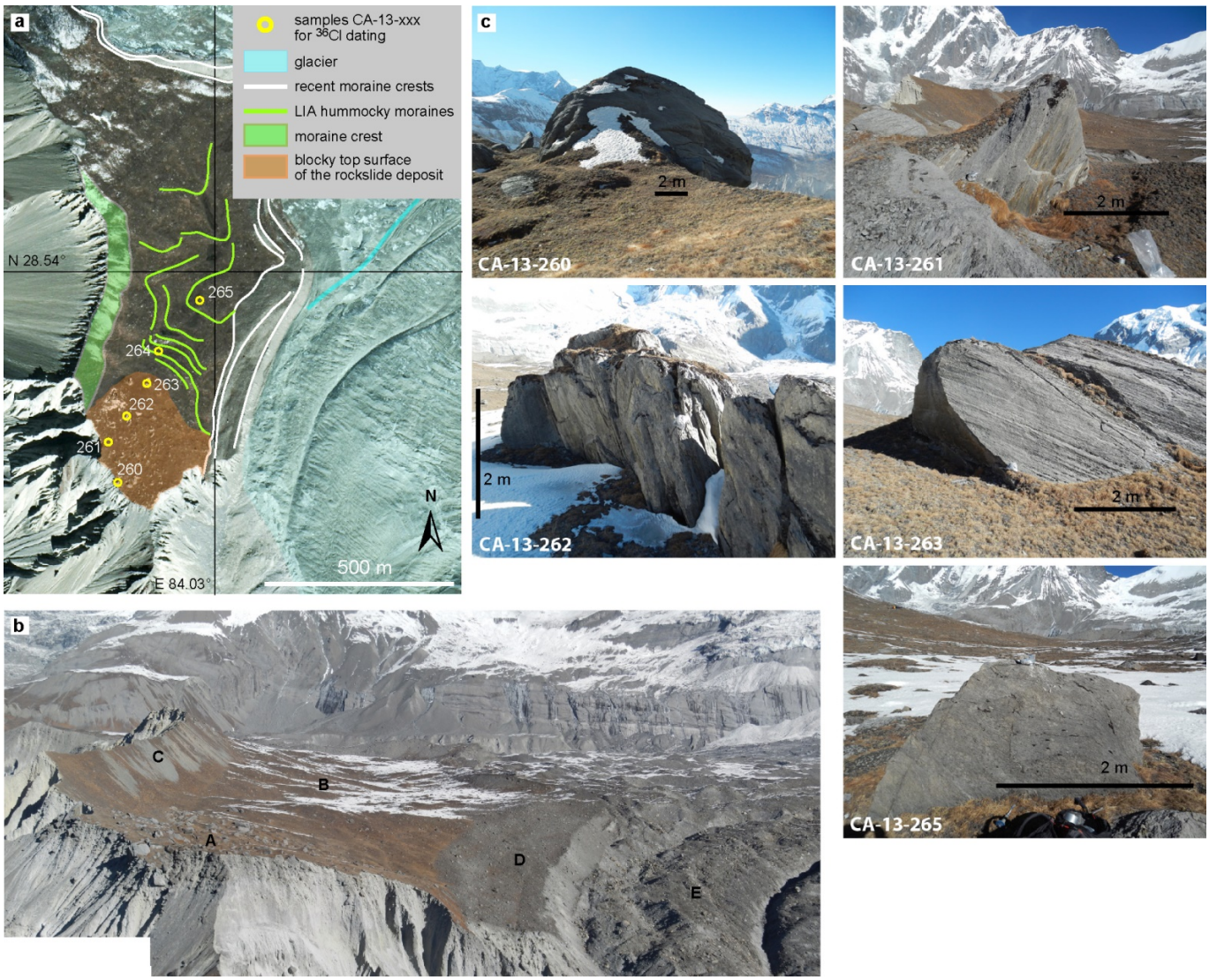

Extended data figure 5

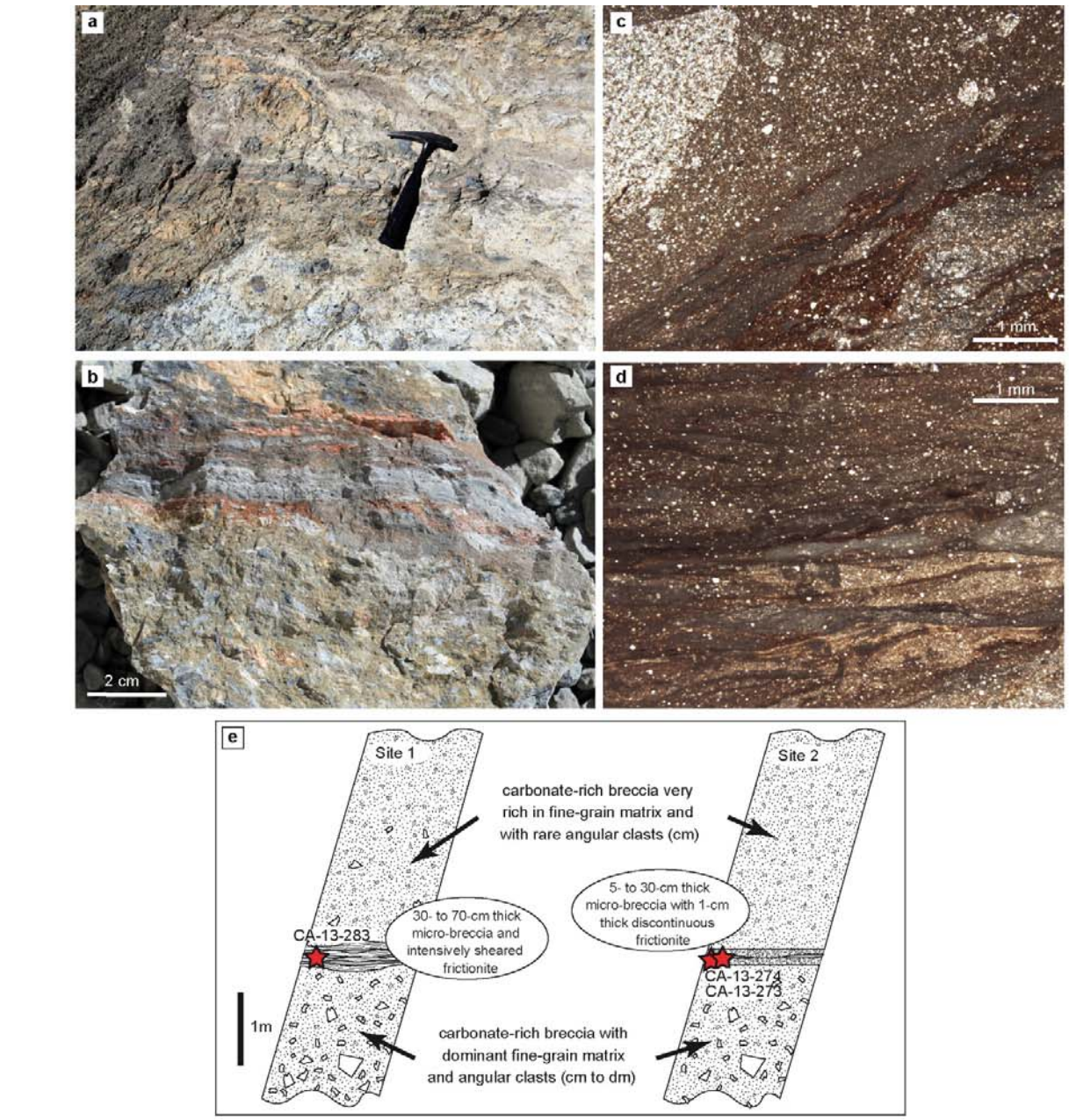

Extended data figure 6

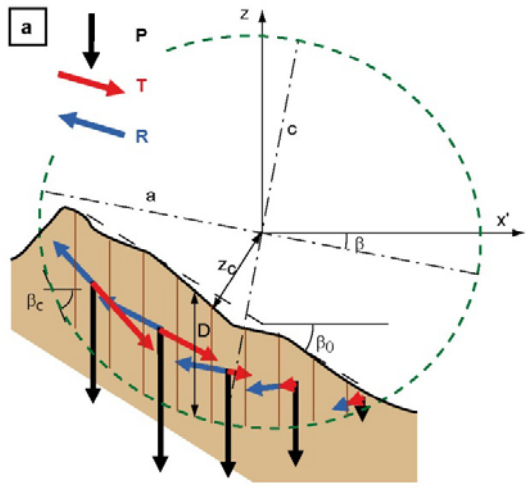

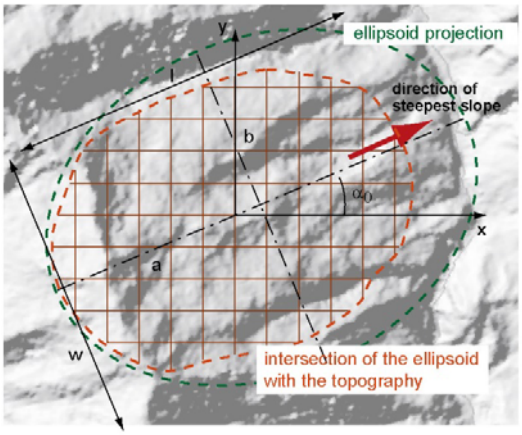

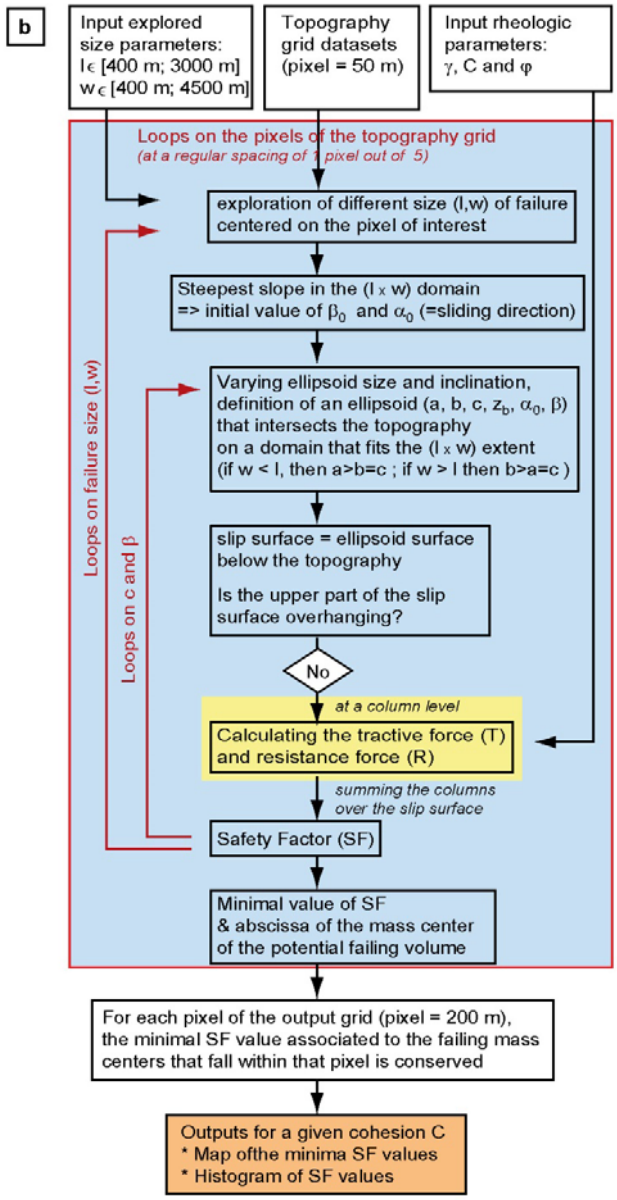

Parameters:
ρ = bedrock density (kg/m³)
dx = topography grid size
φ = internal friction angle (fixed at 35°)
C = cohesion (N/m²) (incrementally varied

Local topographic variables:
β_0 = downward slope angle
α_0 = orientation or aspect of the topographic slope

Explored ellipsoid parameters:
z_c = distance of the ellipsoid center to the topography
β = tilting angle of the ellipsoid
a, b, c = ellispoid excentricity parameters

Local variables along the ellipsoid surface:
D = local thickness of rock column
β_c = local slope of the surface of rupture
α_c = local orientation of the surface of rupture
$\beta_m = \text{atan}(\cos(\alpha_c - \alpha_0).\tan(\beta_c))$ = apparent dip of the failure surface in the slip direction (equated to α_0)

Local Forces along the ellipsoid surface:
Weight of a column of material: $P = \rho g D dx^2$
Tractive force: $T = dx^2.\rho g D.\sin(\beta_m)$
Resisting force: $R = dx^2.(C/\cos(\beta_c) + \tan(\varphi).\rho g D.\cos(\beta_c))$

Safety Factor : $SF = \frac{\sum R_{(x,y)}}{\sum T_{(x,y)}}$

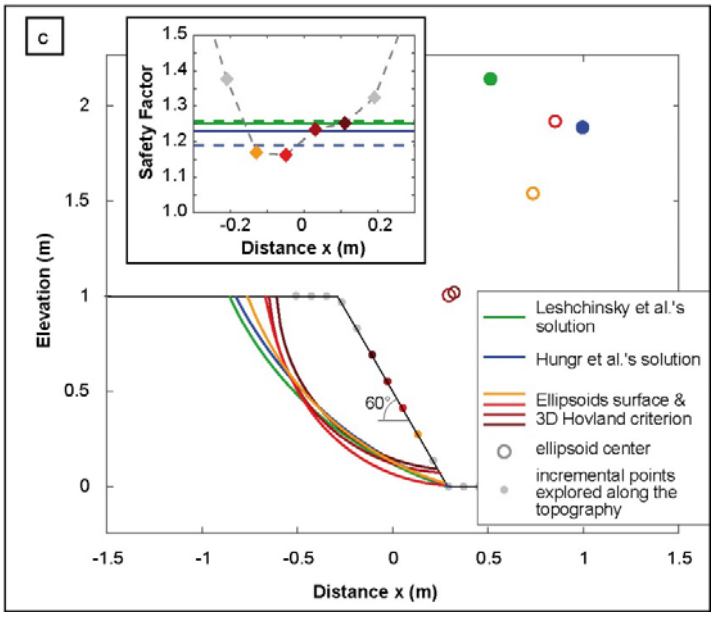

Extended data figure 7

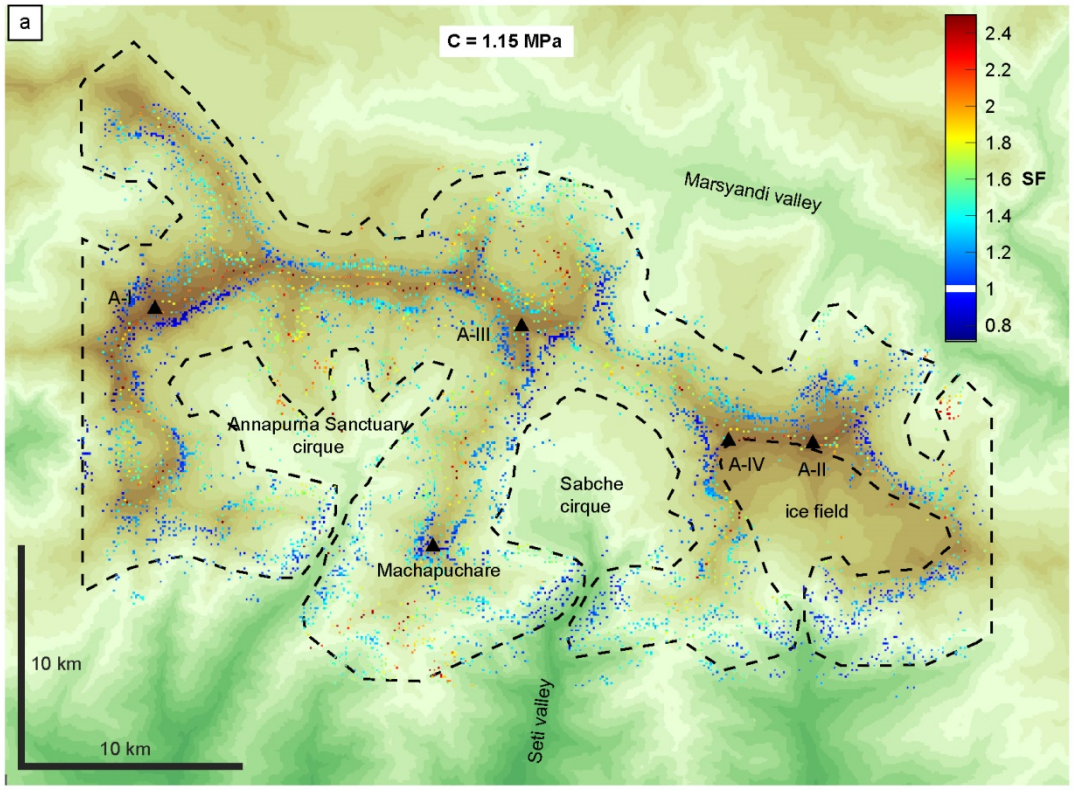

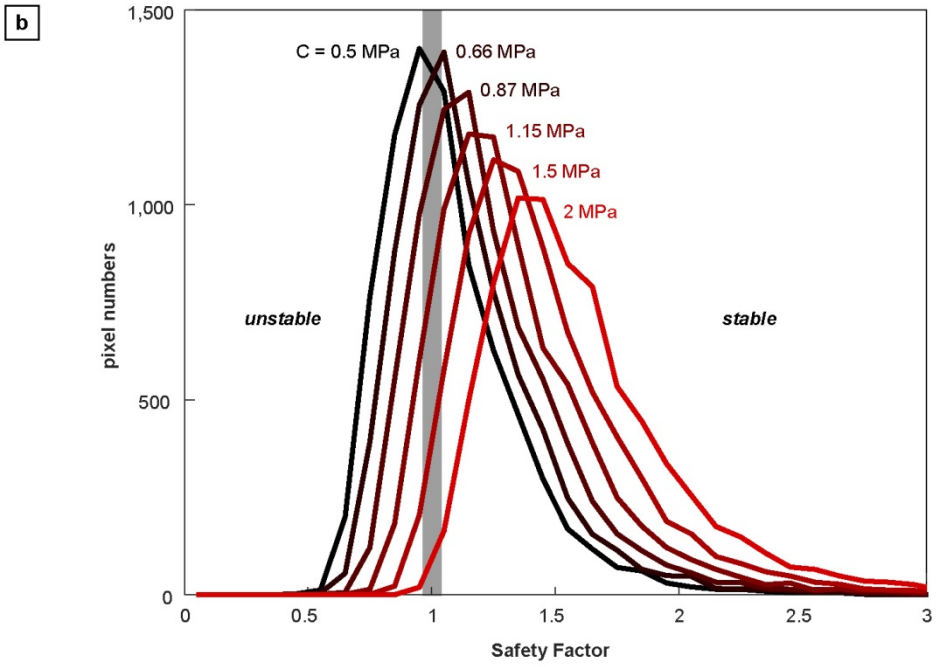

Extended data figure 8

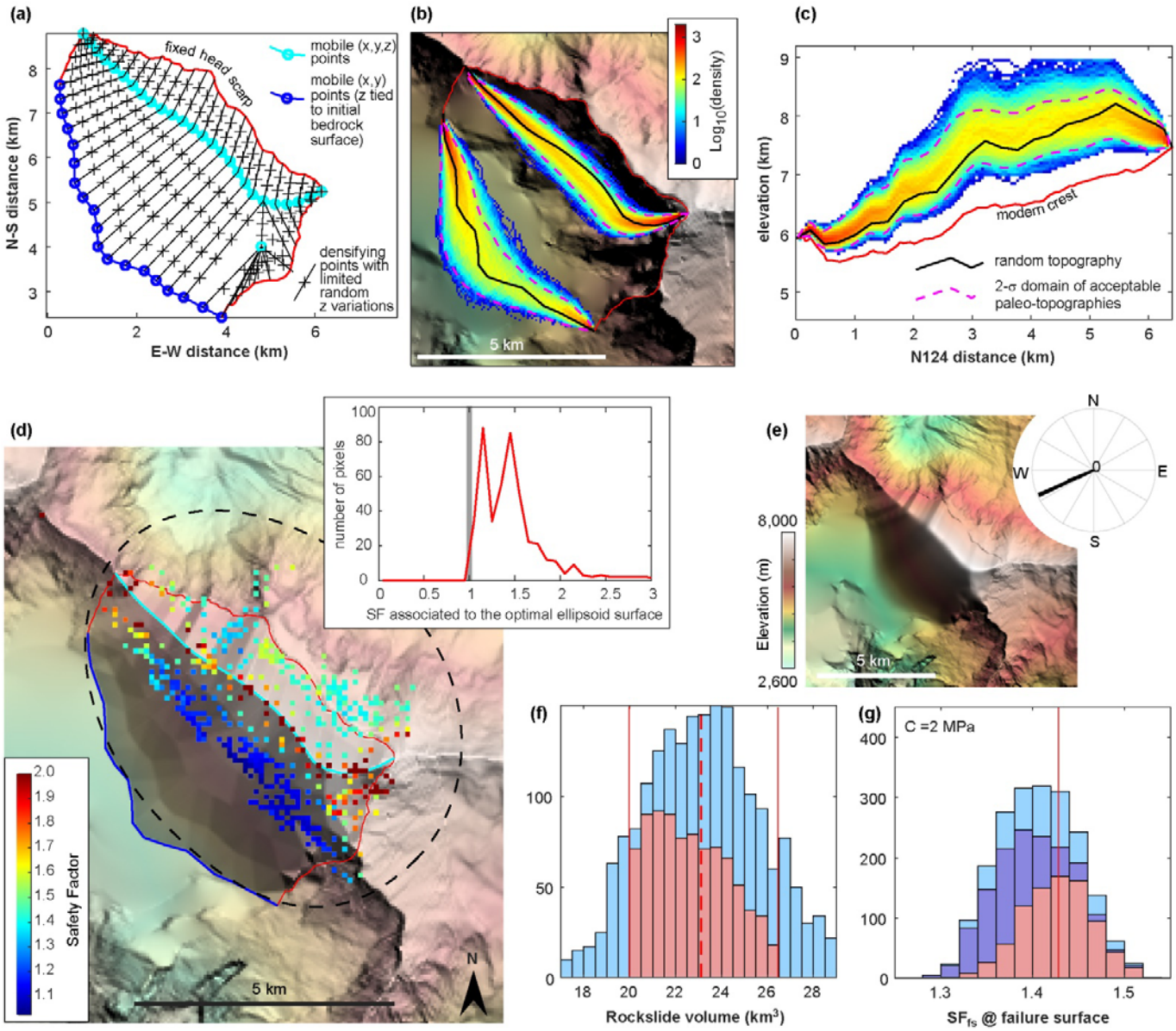

Extended data figure 9

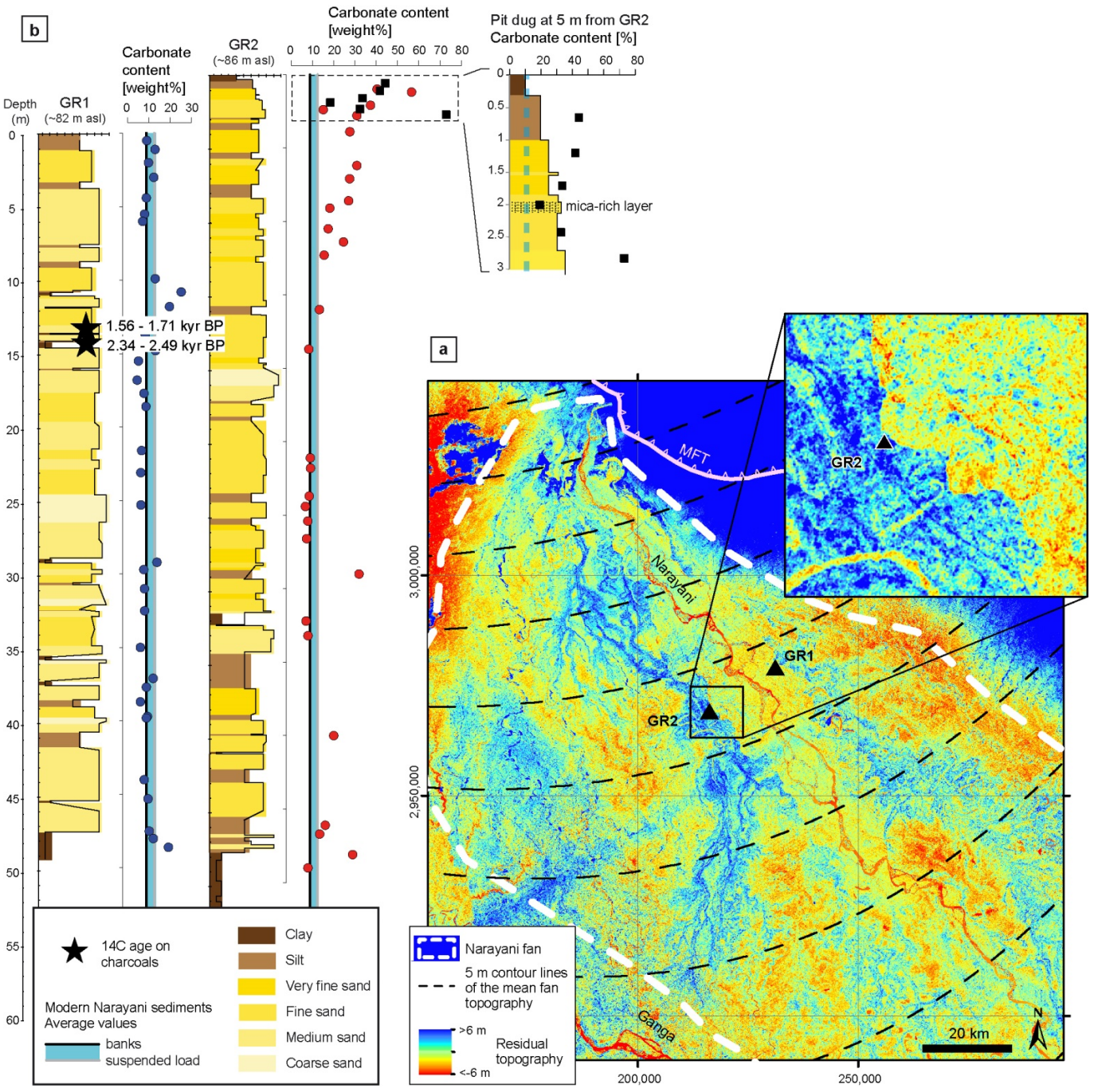

Extended data figure 10

Data availability:

All data used in this study are from the published literature as referenced[36-38], or presented in Sup. Info. tables SI-10-1,2 , SI-11-1,2,3 , SI-12-1,2 and SI-13-1.

Code availability:

To calculate minimal SF maps and reconstruct Annapurna IV paleo-topography, as shown in Extended Data Figs. 8-9, we wrote two original codes in MATLAB, described in the Methods. The two codes are available from the corresponding author upon reasonable request.

Acknowledgements: J.L. thanks B. Sitaula for his invaluable logistic help in the field, L. Bollinger for his help during the helicopter flight in Sabche cirque and the numerous pictures he took, Y. Gunzburger, F. Carraro Braga, M. Manas and P. Kumar for initial discussions and modelling on slope stability of the paleo-summit. We also thank D. Burbank, S. Gallen and N. Hovius for their very positive and constructive reviews that greatly helped to improve our manuscript. This study was funded by the ANR Calimero and the INSU-Syster and INSU-Artemis programs. P.G.V. acknowledges funding from the French ANR-PIA programme (ANR-18-MPGA-0006). The Pleiades images were acquired in the framework of the Isis collaborative program between the CNES and INSU. We thank the LMC14 (Laboratoire de Mesure du Carbone-14), ARTEMIS national facility (LSCE (CNRS-CEA-UVSQ)-IRD-IRSN-MC) for the ^{14}C AMS results, and the ASTER national facility (Cerege (CNRS, Univ Aix Marseille)) for the ^{36}Cl AMS results.

Author contributions: J.L. designed the study, conducted the modelling and wrote the manuscript, J.L. and A.G. collected observations and samples, C.G. realized the DTM, P.G.V. the IRSL measurements, V.Gu. and L.B. the ^{36}Cl measurements, C.M., JP.D. and V.Ga. conducted the ^{14}C measurements, and T.R., C.F-L., G.M. and J.L. handled the carbonate data and core drilling in the Ganga plain. P.G.V., C.F.L. and V.Ga. actively participated in the manuscript polishing.

Competing interests: The authors declare no competing interests.

Supplementary Information is available for this paper.

Correspondence and requests for materials should be addressed to J. Lavé.

Supplementary Information

SI-1*:* The breccia deposits of the Sabche cirque.

Figure SI-1-1: **Additional sedimentologic description of the breccia deposit in Sabche cirque**.

(a) Aerial view of the Sabche cirque towards the north west with, in the background, the Annapurna III summit and the ridge between the Annapurna Sanctuary cirque and the Sabche cirque, made up of the Annapurna Yellow Limestone formation[28]. The breccia of the rock avalanche deposis is visible on a large area of highly dissected landforms.
(b) Outcropping contact between the underlying bedrock and the breccia deposit (green dashed line).
(c) Compact, homogeneous, pulverized and indurated fine grained breccia exposed over the cliff of a steep penitent.
(d) Internal contact between yellowish and greyish breccia facies in the central part of the deposit, as observed from above and suggesting limited mixing during the rockslide collapse;
(e) and (f) Coarse and blocky material close to the top, displaying reverse granular grading.
(g) and (h) Contacts close to the southern base of the cirque deposit: the yellow arrow indicates a contact between yellowish and whitish breccia facies with a larger proportion of coarse elements embedded in the matrix of the yellowish facies; the red arrows highlight the shearing contact where thin band of shearing and micro-crushing were sampled for IRSL analysis (CA-13-283 is located in between the two arrows pointing toward the right).
(i) Zoom in on a rare ten-metre block of layered marly limestone (outlined by the black dashed line), within the breccia, in the basal part of the deposit.
(j) and (k) Characteristic matrix of the breccia deposit with millimetre (j) to centimetre (k) fragments

Photos (a) to (f) = taken from an ultra-light aeroplane or from helicopter.

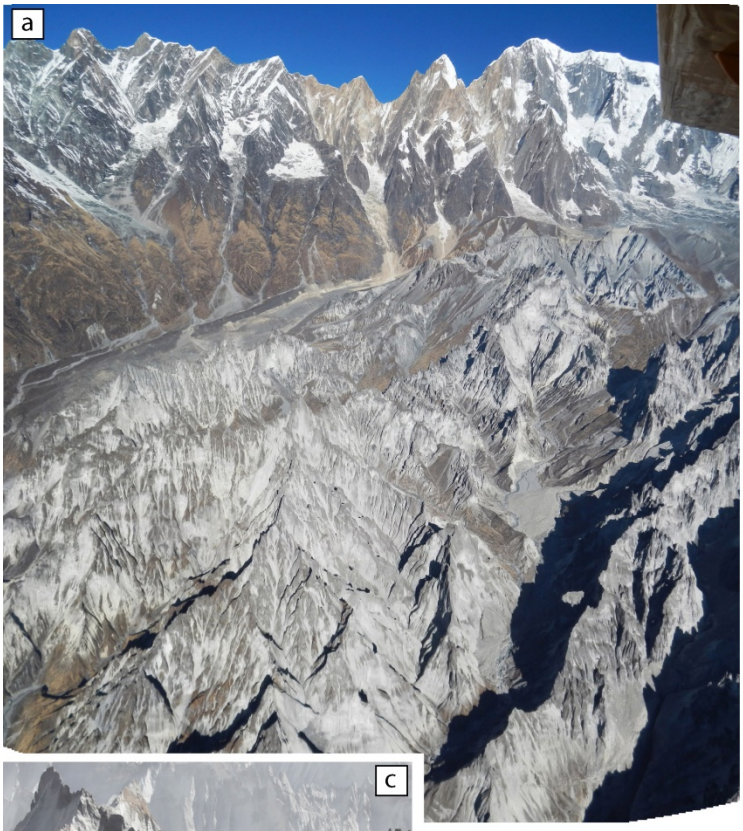
a

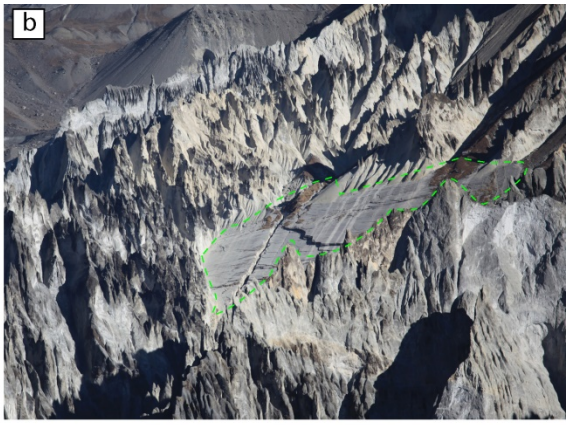
b


e

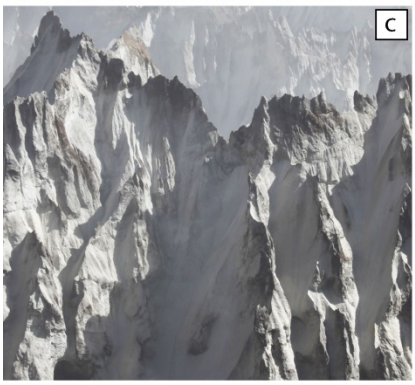
c


f

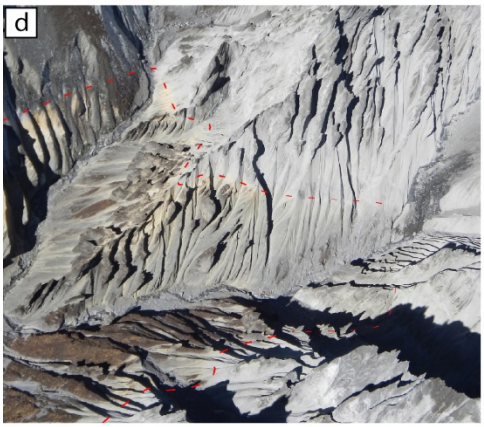
d


g


h

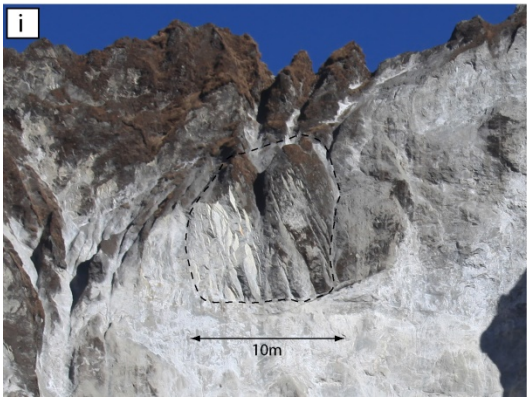
i
10m


j


k

SI-2*:* Remnants of granular flow avalanche deposit in the upper Seti valley.

Along the upper Seti, few remnants of the Sabche rock avalanche deposit are preserved along the valley walls or as isolated >200-m-high massive spurs remnants (figure SI-2-1). The preservation of the spurs is closely linked to the pinning of the very dynamic Seti River by epigenetic gorges carved into the gneisses of the High Himalayan Crystalline units. These epigenic gorges have been interpreted as resulting from local landslides deposits[36]. However, the fine and whitish brecciated material, rich in carbonates, as well as the absence of gneissic elements, except at the contact of the wall of the valley, indicate without any ambiguity an origin located in the cirque of Sabche.

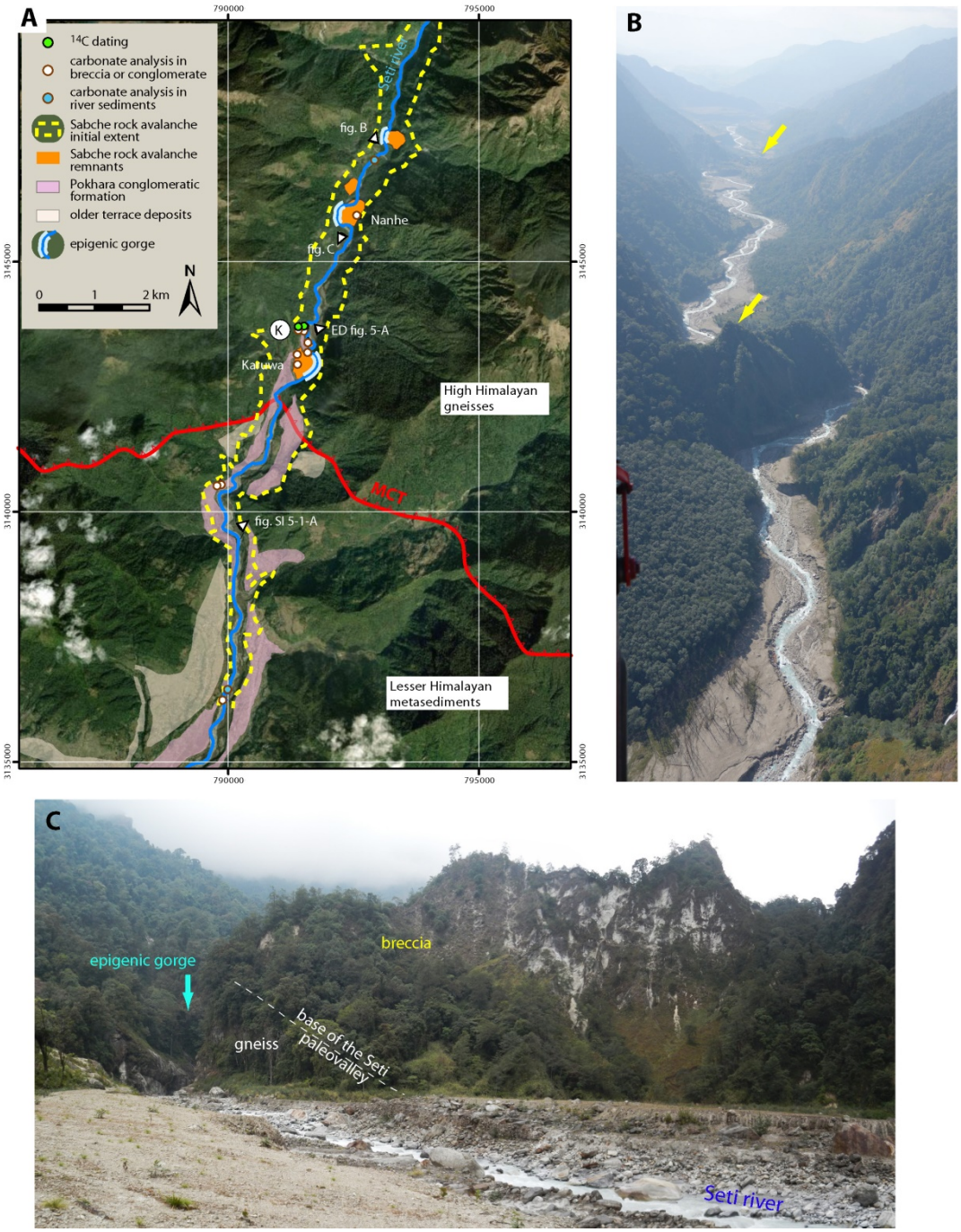

Figure SI-2-1: A. Map of the main remnants of the Sabche rock avalanche deposit along the upper Seti. B. Aerial view (looking southward) of the upper Seti showing two major breccia spurs associated to epigenetic gorges at Nanhe (yellow arrow in the foreground) and Karuwa hill (yellow arrow in the background). C. Picture of the south face of the breccia spur at Nanhe.

SI-3: Digital Terrain Model realization

A high-resolution DTM (Digital Terrain Model) (fig. SI-3-1) has been computed from Pleiades tri-stereoscopic panchromatic images acquired on December 12, 2014 and November 19, 2015 at ~0.5 m spatial resolution.

The DTMs have been calculated through an automatic pipeline which performed the data co-registration and the DTM generation as described in (Guerin, 2017). The data co-registration is realized as a pre-processing step in order to ensure that the images (and hence the DTM) are finely registered between each other's. This operation consists in a bundle-block adjustment of all the data available that can be performed without any Ground Control Points (GCP).
Once the registration is performed, the DTMs are generated at each date according to the methodology described in (Guérin, 2017) and based on the so-called ground space image matching, performed with the open source software MICMAC, developed by the IGN (French Geographic Institute) (Pierrot-Deseilligny, 2006). This methodology enables the calculation of an elevation value for each point on a grid defined on the ground with a determined planimetric and an altimetric step. Thus, for each ground point of the grid, the images coordinates are obtained according to the refined acquisition models of the images that links the ground position of the point and its coordinates on the images. A correlation score is then computed between the pixels windows selected over each image and at each altitude of the grid. The final altitude value is chosen considering the correlation score and a regularization term. Figure SI-3-1 represents the final DTM generated from the Pleiades tri-stereoscopic images. For this study, both DTM have been generated at a 1 m planimetric and altimetric step and resampled to 50 m for the need of the study.

Cloudy areas partially affect the summits and crests surrounding the southern and western parts of the cirque. In those areas, the DTM was complemented from digitized 1/50,000 topographic maps (40 m contour elevation). However, the breccia deposit and the failure surface of the rockslide in the central and north-eastern part of the cirque respectively are well resolved, and well adapted for reconstructing the initial volume of the deposit, measuring bedding dip of structural cliffs or for the calculation of the transverse curvature.

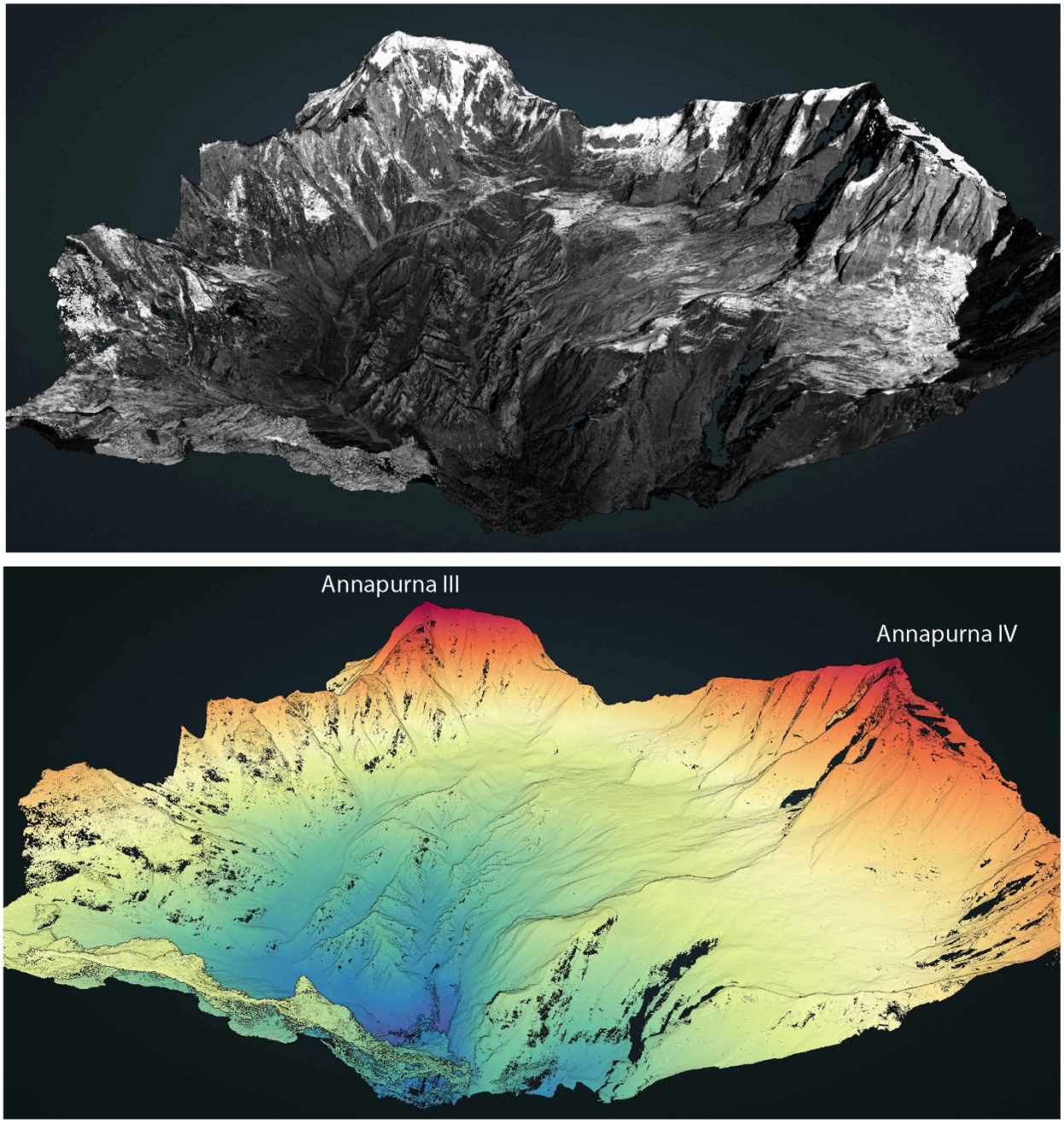

Figure SI-3-1: 2 m *Tri-stereo DTM* (lower), before holes filling and cloud corrections, and panchromatic 0.5 m Pleiade image draped on top of the DTM (upper).

SI-4: The geometry of the initial surface

To reconstruct the initial upper surface of the landslide deposit, we can first rely on a few remnants in the northern part of the cirque (Fig. 1c, Extended Data Fig. 4b and 5a) and on the constraints given by the breccias outcropping on the crest that borders the southern flank of the cirque (Extended Data Fig. 2f). These surfaces are all located at an altitude of ~4,600 m. However, they are not sufficient to constrain the geometry of the deposit surface in its central part, and the remnants of uneroded breccias forming the steep penitents in the centre of the cirque provide only a minimum elevation (fig. SI-4-1c).

To try to constrain this surface, it is possible to refer to the geometry generally observed for rockslides and rock avalanches. Depending on the fall height, basal friction, degree of internal fragmentation, or the morphology of the valley, a rock avalanche can travel a variable distance. If an avalanche is unimpeded, it is generally characterised by a thickness and surface elevation that decreases downstream. On the other hand, in the case of frontal confinement by a relief that hinders the avalanche flow, depending on its residual kinetic energy, the avalanche can go up the slope (runup), and the final deposit can be characterised by an inverse topographic gradient (e.g. Aaron and Scott McDougall, 2019). The most commonly used parameters characterizing the geometry of rock avalanche deposit and the avalanche mobility are the runout distance and the ratio of the fall height over the runout distance. These parameters have been extensively documented in the past, whether or not differentiating the type of flow confinement (e.g. Strom et al., 2019). In contrast, the shape of rock avalanche deposits has been much less parametrically described.

The case of the Sabche cirque is quite uncommon since the avalanche was confined both frontally and laterally, despite the fact it could overflow the ~4,600-m-high E-W crest in the southern part and also find a lateral exit through the Upper Seti gorges. In the absence of other well-documented examples of a collapse with such a configuration, we consider frontally confined collapses as the closest analogous and compare with a set of 8 giant collapses. Disregarding numerous secondary depressions and ridges that can exceed 100m in amplitude, the average geometry of these deposits shows 3 end members: a classically decreasing elevation gradient (schematic case A on fig. SI-4-1a, and natural cases 3, 4 and 8 on fig. SI-4-1-b), a uniform elevation surface (schematic case B on fig. SI-4-1a, and natural cases 1, 5 and 6 on fig. SI-4-1-b), and an inverted gradient with a strong runup (schematic case C on fig. SI-4-1a, and natural cases 3, 4 and 8 on fig. SI-4-1-b). Transversely, all deposits are characterised by a convex shape (Fig. SI-4-1-b) with a more or less flattened central part (respectively schematic cases E and D on fig. SI-4-1a).

The comparison with frontally confined collapses suggests that the presence of a depression in the centre of the deposit is very unlikely. Longitudinally, irrespective of the type of surface deposit geometry (type A, B or C), the centre of the deposit would be expected to be either higher than the SW edge (type A) or higher than the NE edge (type C). In addition, the flat surface remnants in the northern part of the cirque (red spots on Fig. SI-4-1c) display a fairly horizontal surface without any slope in either direction. Transversely, even if the 8 collapses presented in Table SI-4-1 and Fig. SI-4-1b are not subject to lateral confinement, a maximum elevation in the centre of the cirque with a more or less convex shape is expected. The centre of the deposit was therefore likely ≥4,600 m. The present position of the main glacier of the cirque, originating from Annapurna III, to the NNW, also supports this conclusion: it is strongly deflected along the western wall of the cirque, whereas it should have flowed towards the centre of the cirque if the deposit had been affected by a central depression.

On the basis of the above considerations, and even if one can imagine a possible convex shape in the centre of the deposit and a chaotic surface (secondary depressions and ridges), the simplest hypothesis is to consider that on average the initial surface of the Sabche rock avalanche can be approximated by a sub-horizontal surface at an altitude of ~4,600 m. The local geometry at the transition between the cirque and the Upper Seti valley remains however partly unresolved: there the initial surface of the Sabche deposit plunges toward an avalanche valley deposit, the minimum altitude of which can only be estimated from the few remnants plastered on the walls of the Upper Seti gorge (Extended Data fig. 4b and Fig. SI-2-1). Because this zone only concerns a few square kilometres, we estimate that the associated uncertainties remain limited to ≤1 km^3. Taking into account this uncertainty as well as the possible variations in altitude of 100 to 200 m linked to an irregular surface (secondary depressions and ridges) or a central convexity, we assume that the uncertainties on the volume of breccia in the cirque related to the over- and under-estimation of the deposit upper surface reaches +2 and -3 km^3 respectively.

Name	Country	n° on fig. SI-4-1b	Latitude (°N)	Longitude (°E)	Estimated volume of the deposit (km^3)	reference
Baige	China	1	31.08	98.70	0.025	Zhang et al. (2019)
Dukur Pokhari	Nepal	2	28.59	84.19	1	ref. 34
Daguangbao	China	3	31.63	104.12	1.3	Chen et al. (2014)
Ringmo	Nepal	4	29.18	82.94	1.5	Weidinger and Ibetsberger (2000)
Aricota	Peru	5	-17.37	-70.33	2	Delgado et al. (2019)
Kalopani	Nepal	6	28.65	83.59	3	Fort (2000), ref. 34
Kofels	Austria	7	47.11	10.94	4	Zangerl et al. (2021)
Flims	Swiss	8	48.83	9.30	12	Polet and Schneider (2004)

Table SI-4-1: Catalogue of the frontally confined rockslides and rock avalanches used in fig. SI-4-1b.

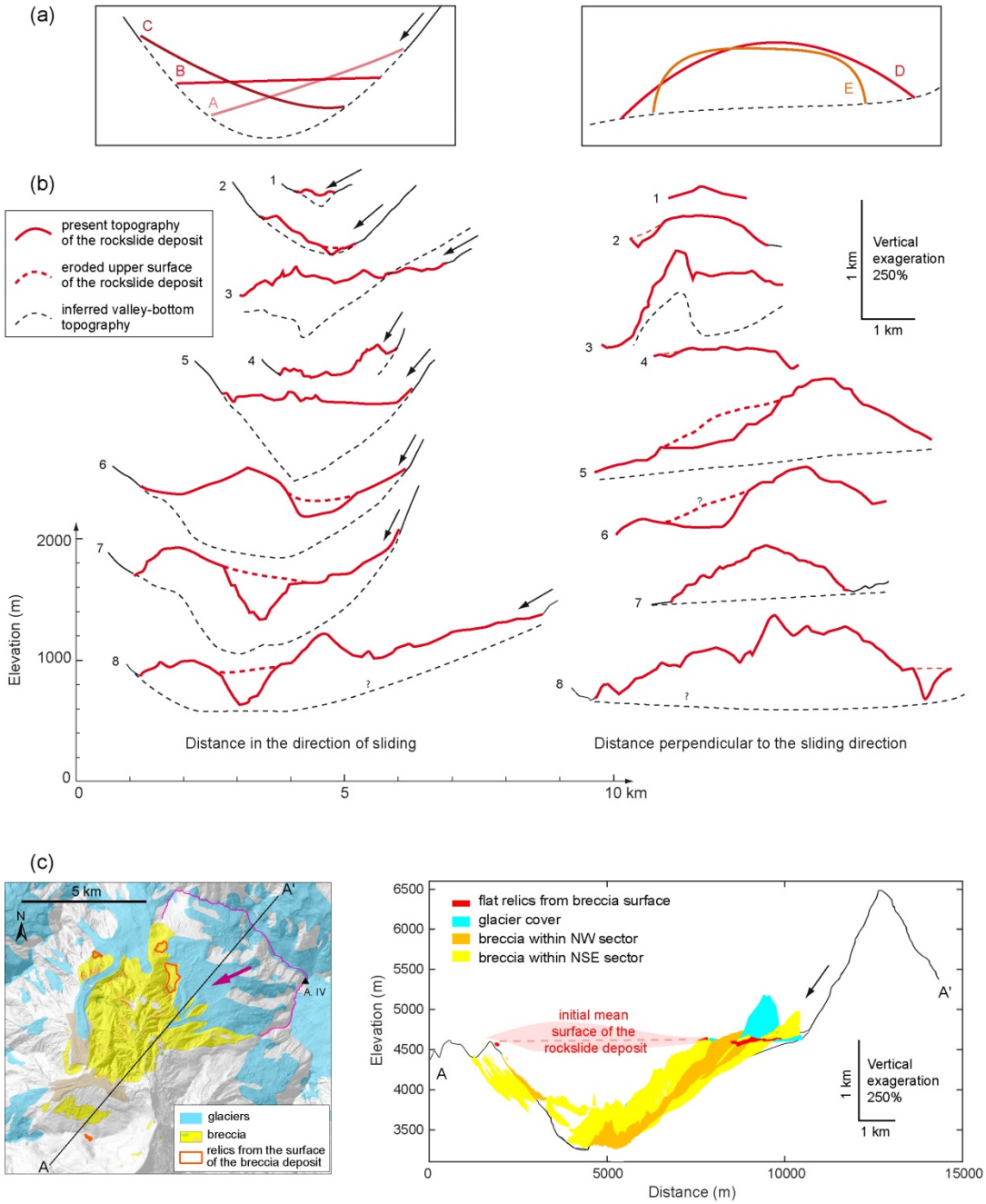

Figure SI-4-1: (a) Schematic models of the geometry of rock avalanches deposits. (b) Geometries of various frontally confined rockslides or rock avalanche deposits (see Table SI-4-1). (c) Longitudinal cross section on which all outcrop areas of the Sabche rock avalanche breccias have been projected (orange and yellow areas correspond to areas SE and NW of line AA' shown on the left map), and the hypothesized geometry of the initial surface connecting the northern and southern relics at ~4,600 m.

SI-5: Coefficient of expansion of the breccia material

In order to derive the volume of solid rock that collapsed from the Annapurna IV ridge, the volume of breccia deposit was corrected from breccia porosity. Porosity measurements made on various samples of breccia taken at different places in Annapurna region were realized by measuring density through weighing of samples plunged into water and Archimede's principle and assuming a rock density of ρ = 2.68±0.06 g/cm^3, for the Late Cambrian to Silurian TSS rocks. The porosity or expansion rate of the breccia material slightly depends on the burial depth (Fig. SI-5-1). Average value of 15+/-5% was found consistent with previous estimates of 15% made on rock avalanche material[66].

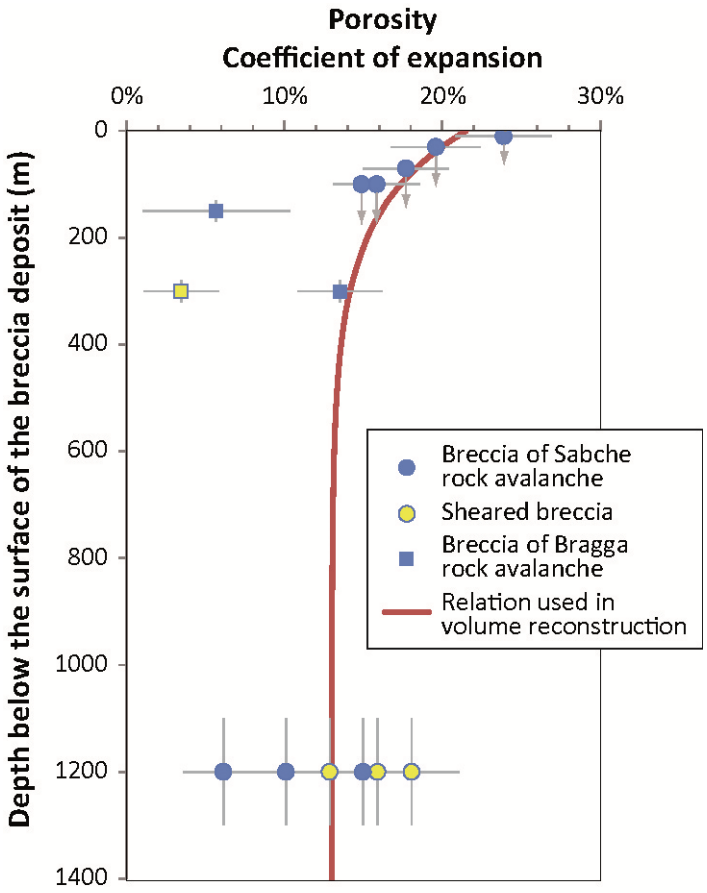

Figure SI-5-1: Average curve of the coefficient of expansion of the breccia material vs burial depth, as derived from density measurements made on rock and granular avalanches deposits in Sabche cirque, Upper Seti valley and upper Marsyandi in Bragga area on the northern part of the Annarpurna massif.

SI-6: Cohesion of the unglaciated areas along the southern flank of the High Himalaya

To demonstrate the higher apparent cohesion of the rock mass building the high-altitude peaks of the Annapurna range (Extended Data Fig. 8a), we could compare with values of the literature[47], derived in unglaciated areas. However, these previous studies in fluvially-dominated regions, which indicate cohesion values generally <0.1 MPa, use a distinct approach and were conducted in a different setting (Longmen Shan characterized by lower tectonic activity than the Himalaya).

In order to provide cohesion values of rock mass in unglaciated, fluvially-dominated Himalayan areas, we applied our method (see Methods and Extended Data Fig. 7) to the landforms south of the Annapurna massif. We defined an area (polygon in yellow color on Fig. SI-6-1a) bounded to the north by elevation < 4,000 m and to the south by a line that follows the major topographic break in slope and river gradient steepening (purple dashed line on Fig. SI-6-1a). Because this southern boundary is assumed to correspond to the top of the Main Himalayan Thrust mid-crustal ramp[25], this ensures that both glaciated and non-glaciated landforms are analysed in areas affected by similar high uplift rates (~3-4 mm/yr)[25,26], and that the comparison between both landforms is relevant. Although the influence of the tectonic variable can be ruled out, the influence of the lithology might remain, however, possible: the glaciated zone concerns carbonate sedimentary series, whereas the non-glaciated zone is mainly dominated by gneisses. Nevertheless, the change in slopes with altitude observed in the Everest region[2] have been identified as independent of lithology and suggests that here too lithology might not be a major controlling variable.

Our analysis shows that the rock mass building the fluvially-dominated landforms has a much lower strength than the glaciated high-altitude ridgelines, with a proportion of unstable slopes much higher whatever the cohesion value explored (Fig. SI-6-1b). As a matter of example, to account for ~90% of stable slopes in fluvially-dominated landforms, the cohesion must be reduced by a factor of 4 (from 1.2 to 0.3 MPa) (Fig. SI-6-1c).

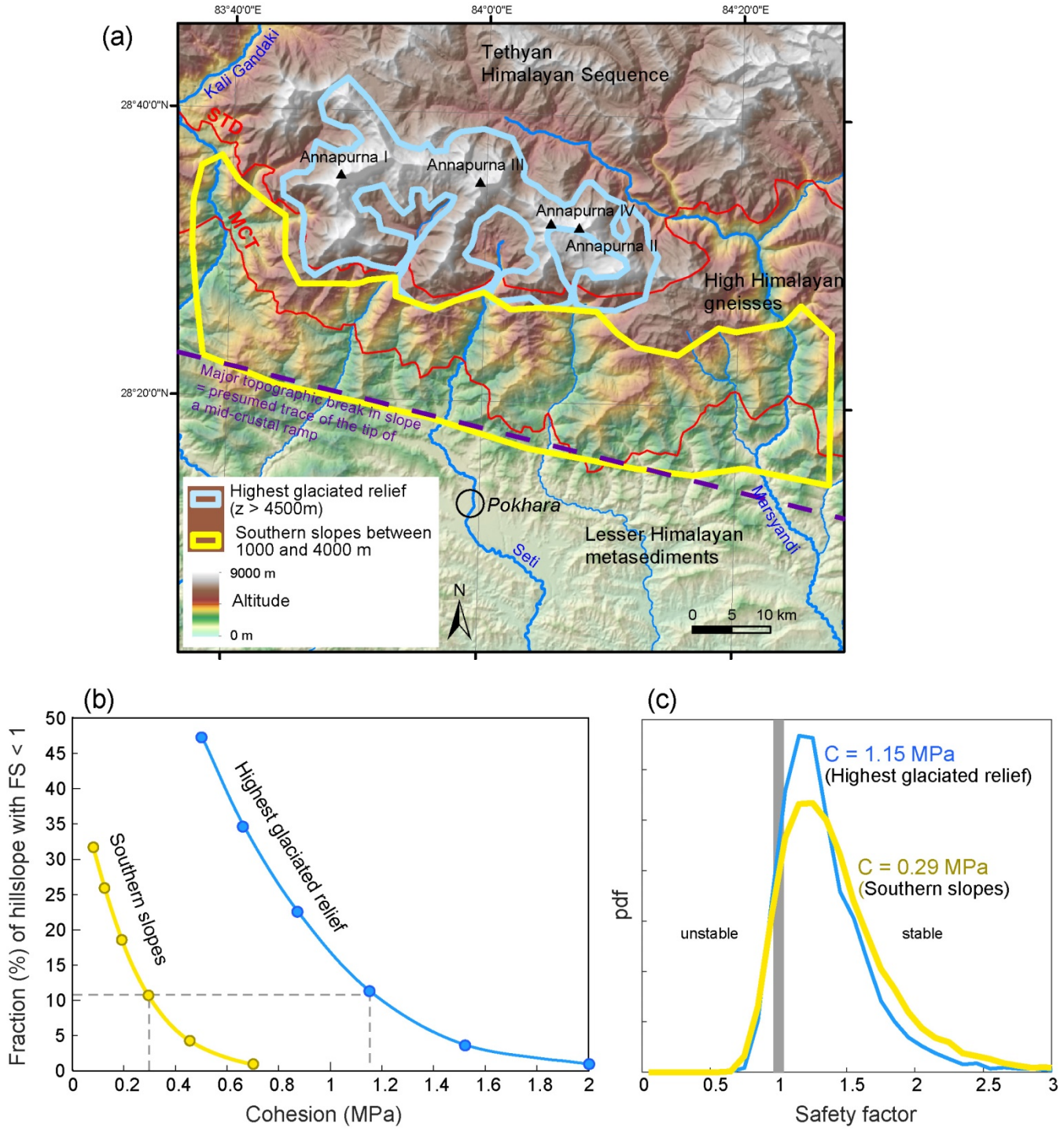

Figure SI-6-1: (a) Map of the High Himalaya in the Annapurna region displaying the two distinct areas of fluvially-dominated southern landforms (delineated by a yellow polygon) and highest glaciated landforms (delineated by a blue polygon), in which the systematic searching procedure (Extended Data fig. 7) has been realized using variable cohesion values but a fixed internal angle of friction of 35°. (b) Comparison for these two areas of the fraction of unstable slopes as a function of the imposed cohesion value. (c) Histograms of the values of the SF for values of cohesion C = 0.29 MPa and C = 1.15 MPa that lead to a similar proportion of unstable slopes (SF < 1) for the fluvially-dominated southern landforms and the highest glaciated landforms respectively.

SI-7: Paleotopographic reconstruction

To reconstructed the paleotopography of the collapsed summit, as also explained in the Method section, we have applied the following computing chart:

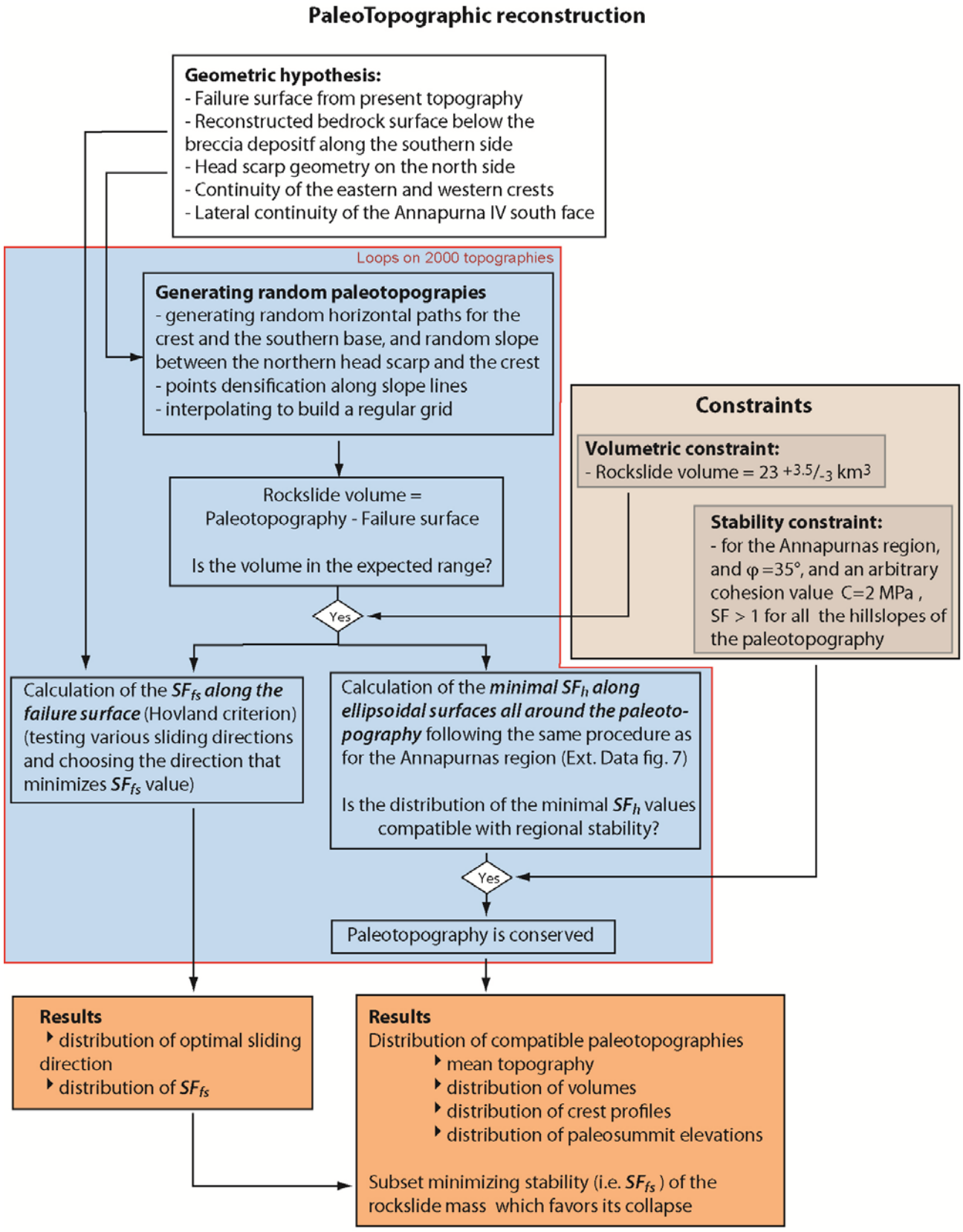

SI-8: Effects of a rise of the 0°C isotherm within the Annapurna massif at the end of the Medieval Climate Anomaly

The Medieval Climate Anomaly from 900 to 1200AD is characterized in some parts of the Northern Hemisphere by warmer temperatures[43]. Temperature anomalies were presumably maximal north of the Indian sub-continent, at high elevations, and at the end of the 12th century (Zhou et al., 2011). In the High Himalaya region, this temperature increase might have exceeded +1°C, inducing a rise of the 0°C isotherm by ~200 m.

Assuming only heat diffusion and an average thermal diffusivity for marly limestone of 1.4×10^{-6} $m^2 s^{-1}$, after 300 yr, this temperature anomaly would have propagated (with an e-fold decrease) ~150 m into the Annapurna massif and caused a fraction of the frozen section of the future failure surface to melt, mainly in its basal part (Fig. 3c).

To estimate this melted fraction, we consider a highly simplified and conservative 1D diffusion thermal model applied to the substrate of the paleo-Annapurna IV. We first estimate the thickness of permanently frozen rock below the surface, i.e. the high altitude permafrost. For that, it is assumed that the topography consists of ~45° slopes, that the 1D (vertical) thermal gradient in the massif substrate is of the order of 25 °C/km, that the atmospheric lapse rate is 6 °C/km and that the 0°C isotherm is located at 5000m. Projected onto the failure surface of the giant rockslide, the model predicts that permafrost affected a portion of about 3 km2 along the future rupture plane (light blue area in Figure SI-8-1), or 10% of the total failure surface. Next, we diffuse (analytical solution based on the Gauss error function) the assumed medieval climate anomaly (1°C warming for 300 years) into the massif, and calculate the area that has thawed. The melted area would have been ~0.1 km^2: this would have changed the frozen area of the failure surface by less than 3%, and it would have changed the cohesion of a portion that represents less than 0.3% of the total slip surface. This is a very simplified model which does not take into account the 3D effects of topography, nor the effects of snow or ice cover, but it suggests that the change in cohesion over the entire failure plane is proportionately very small. Unless the massif is close to a critical state or the temporary rise in temperature also affects fluid flow, or pore pressure via a change in the water table, it is likely that the thermal anomaly was not sufficient to trigger the slide.

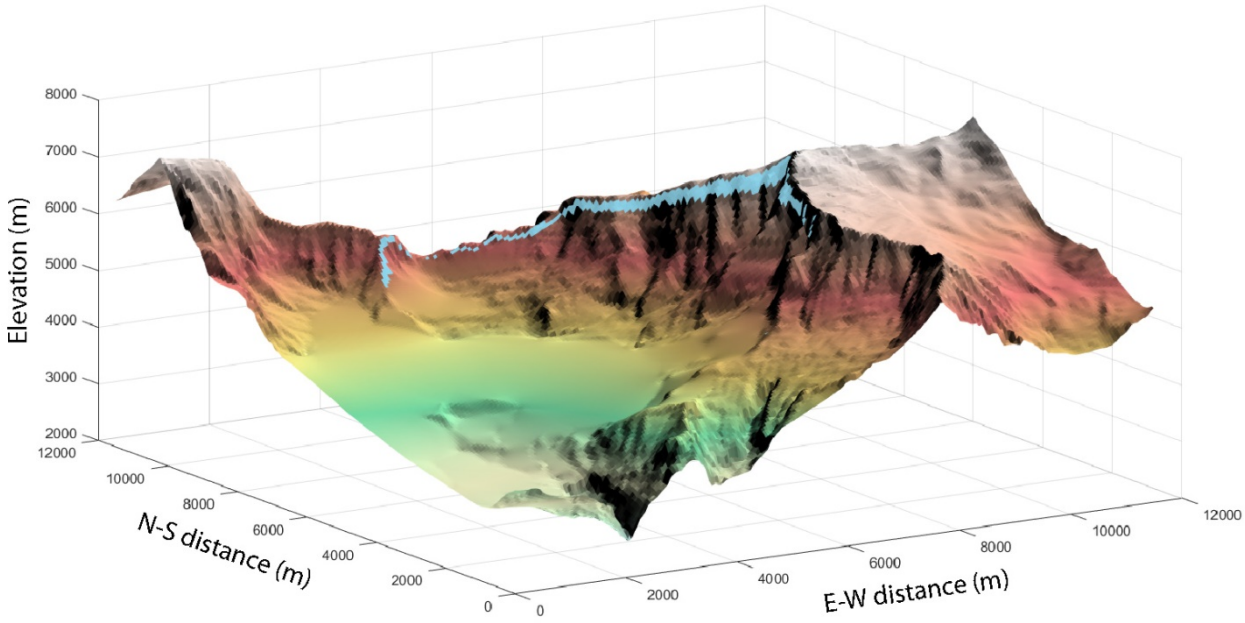

Figure SI-8-1: 3D view of the presumed topography of the giant rockslide sliding surface with the frozen parts in light blue shading.

SI-9: The Pokhara conglomeratic deposits

A. Sedimentology of the Pokhara conglomeratic formation in the Pokhara basin

The Pokhara conglomeratic Formation is characterized by a succession of planar metric to multi-metric conglomerate beds ago[30,36], with different facies (Fig. SI-9-1) and extend from upper Seti (Karuwa = site K of fig.1, down to the mountain front at Narayangad (site N)). All the units are essentially made of angulous to sub-angulous dark limestone pebbles: the origin of the gravels and pebbles is at >95% of TSS limestone and marly limestone, with a few rare granitic or gneissic pebbles, and whose only possible origin is in the Sabche cirque.

Figure SI-9-1: Pictures of some of the typical facies of the Pokhara conglomeratic Formation

In the center of Pokhara valley, most facies are well stratified conglomeratic alluvium made of alternation of relatively well sorted TSS gravels or pebbles (Figure SI-9-1-b and c) of variable median size ($0.5cm < D_{50} < 5cm$). The clasts are subangular to subrounded and are commonly imbricated (Figure SI-9-1-d). The contacts between the layers are mostly planar, without presenting any major unconformity surfaces, except at a few places where small channel reincision by a few meters can be observed (Figure SI-9-1-e). If typical proximal debris-flow units with poorly sorted and matrix-supported material were not observed in the Pokhara basin, layers made of unsorted homometric material (Figure SI-9-1-f), clast- to matrix-supported, suggest clast transport by competent or hyperconcentrated flows. Even in its upstream part (Figure SI-9-1-a), south of Karuwa, a majority of the facies correspond to dominant stratified alluvium, interlayered with a minority of debris-flow-like units. The sorting increases downstream both in the clast and matrix-supported facies.

We interpret these planar conglomeratic units to reflect rapid aggradation during turbulent, sediment-laden flows, with successions of debris floods, sheet and hyperconcentrated flows (Blair and McPherson, 2009), and alluvial reworking. The dominance of sediment-laden or hyperconcentrated require an initial sediment source reach in fine fraction. Finally, it has to be noted that the clasts as well the silty matrix of the conglomerate units display carbonate content very similar to the average material of the Sabche rockslide breccia (fig. 4).

B. Narayangad terrace

The Pokhara conglomeratic formation can be tracked at least down to the Himalayan front, just north of the city of Narayangad (see loc. “N” on fig. 1). There, the remnant of a peculiar fill deposit observed at a few meters above the present river on the left bank of the Narayani river in a somehow sheltered environment. This unit contrasts strongly with the other terrace deposits of the Narayani at that place as much on the level of its much finer granulometry as on the level of its composition much richer in carbonates. This unit presents two sequences of opposite grading but with constant CaCO3 content (Figure SI-9-2),: a basal unit with normal grading unit terminated by very fine silts is overlain in continuity by an inverse grading sequence that ranges from coarse sand to gravel clast-supported conglomerates made of small subangular, sorted, but unstratified, dark limestone gravels of similar composition as Pokhara conglomerates. We interpret such particular stratigraphic order as a deposition first of a suspended sediment laden front, likely generated just in front of the rock-avalanche, followed by aggradation of the fine pebble load that travelled more slowly as a debris or dense flow. Nevertheless the scarcity of these remnants of units indicates that after the deposition of the sequence, the Narayani river was able to recover rapidly and to wash its banks of these ~10-15 m deposits of fine conglomerates, except very locally. A microscopic charcoal or organic debris (C14-68-E) was found at the middle of the silty sequence, and is synchronous of the upper Seti rock avalanche and onset of the filling of Pokhara basin (fig. 2b).

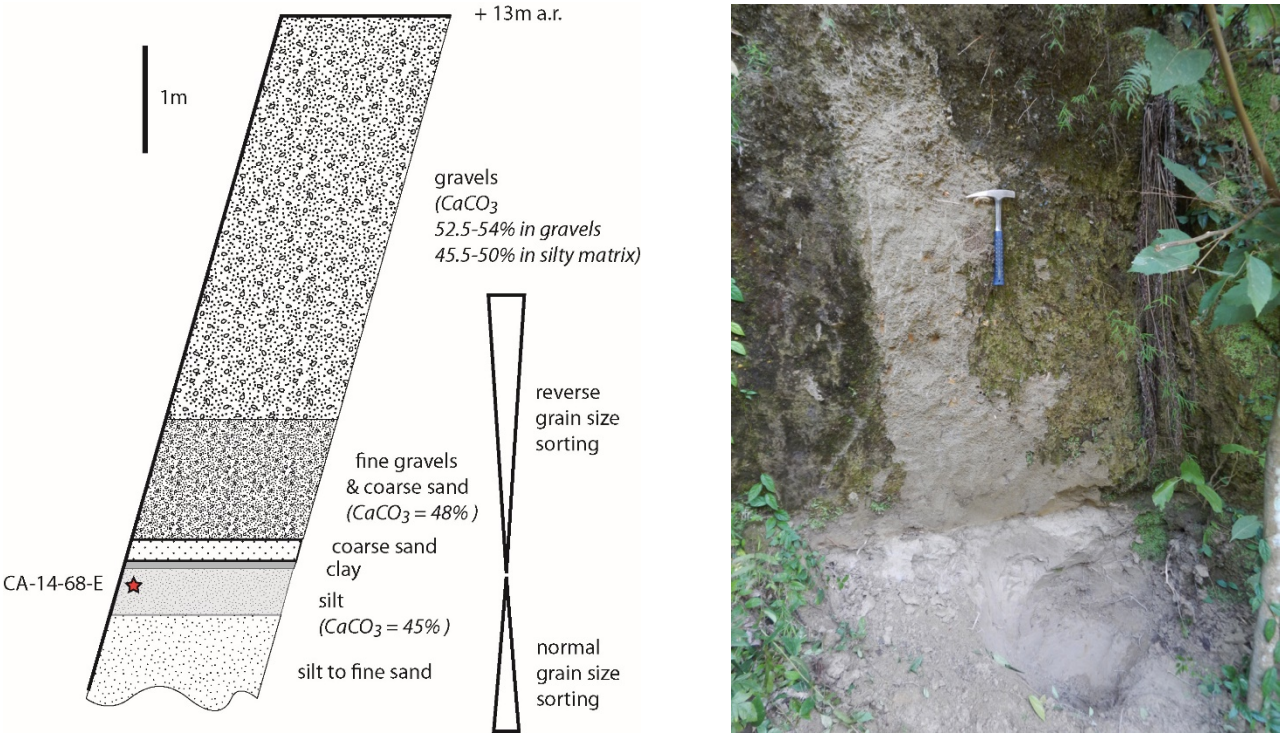

Figure SI-9-2: Micro-conglomerate deposit north of Narayangad (site N on fig.1)

C: Volume of deposited Pokhara type sediments

The volume of conglomerates in the Pokhara and upper Seti valley was estimated to reach ~5 to ~7 km^3 (refs. 30, 36) over a distance of 70 km. Further downstream, the volume of deposited Pokhara sediment was estimated by considering the present geometry of the valley and a sediment filling assuming a linearly decreasing thickness from Pokhara to the Gangetic plain, based on our field measurements: 60 m in the southern Pokhara basin, 20 m at the confluence of the Seti with the Trisuli, 13 m at Narayangad (site "N" on fig. 1b), and 3-5 m at the GR2 borehole (site "G" on fig. 1a). In the Gangetic plain, the long and narrow lobe raised on top of the mega-fan (blue-colored in Extended Data fig.10) was assumed to correspond to the deposition of sediments preferentially derived from the rockslide.

Between the southern part of the Pokhara basin and Naryangad (site "N"), the deposited volume is ~1 km^3. Between Naryangad and the MFT (most frontal thrust), in the Chitwan dun (piggy-back basin), an additional volume of ~2 km^3 of fine gravels and sands could have been deposited. Downstream of the MFT, the lobe deposited at the top in the Narayani mega-fan has represents a volume of sediment of ~6 km^3 (L x W x H ≈ 120 km x 12 km x 4 m). As a whole, 15 km^3 of sediments might have been deposited between Pokhara and the Narayani megafan, that is, considering a porosity of 30% of the sediments, ≤50% of the initial rock volume. The other half was presumably exported further downstream as suspended load like most Himalayan sediments that end up in the Bengal Fan[39].

It has to be noted that we assume above that the downstream units were not fed by the re-erosion of the upstream conglomerates. The synchronism of the sediment at Narayangad (downstream site "N") with the initial granular avalanche in the most upstream part supports such hypothesis.

D: Proportion of Sabche material in the Gandak river after the rockslide

The carbonate-rich lobe of the Narayani fan displays variable carbonate concentration between 30 and 60%, but on average it remains slightly lower than the Sabche breccia and Pokhara conglomerate. This likely arises from mixing with background supply of sediments issued from the whole Narayani catchment.

Considering the average carbonate concentrations of around 55, 40, and 10% for breccia material, sediments in the carbonate-rich lobe of the Narayani fan (upper units of GR2), and mean Narayani sediments (in GR1, lower GR2 cores or sandy fraction of modern sediments) respectively, it is shown that the carbonate-rich lobe of the Narayani was corresponding to the mixing of two volumes of Sabche debris and one volume of background Narayani sediments. Following the Annapurna IV collapse, the input of Sabche

material would have tripled the Narayani sediment flux compared to average values. In order to evacuate ~15 km^3 (the total rockslide volume minus the breccia remaining in the Sabche cirque and the deposited part along the middle and lower Seti respectively) of breccia material out of the mountain range at Narayangad, such a situation could have persisted ~150 yr, which seems to confirm accelerated erosion of the Sabche deposit over a period of 100 yr following the summit collapse.

SI-10: 14C dating of the various organic debris (wood pieces and charcoals) samples of this study

The pdf associated to the mean age for Karuwa and the basal Pokhara conglomerates (Fig. 2) were calculated by computing the uncertainty-weighted average of the 14C raw radiocarbon ages (8 dating for each mean age), before applying the calibration curve of IntCal 13 (ref. 54).

Lab.No	Sample ID	Lat [°N]	Lon [°E]	Elevation [m asl]	Material	stratigraphic setting	Radiocarbon age [y BP]	Calibrated age
Karuwa debris flow								
SacA-41772	CA-14-59	28° 23.24'	83° 58.51'	1460	wood	base of the granular avalanche breccia	950 ± 30	1085 AD ± 47
SacA-43078	CA-14-58	28° 23.24'	83° 58.51'	1460	wood	base of the granular avalanche breccia	840 ± 30	1199 AD ± 29
SacA-48072	CA-16-5-C	28° 23.24'	83° 58.51'	1460	bark	base of the granular avalanche breccia	830 ± 30	1208 AD ± 30
SacA-46539	CA-16-5-D	28° 23.24'	83° 58.51'	1460	monocots type stem	base of the granular avalanche breccia	870 ± 30	1139 AD ± 61
SacA-48073	CA-16-5-D	Replicate					895 ± 30	1125 AD ± 52
SacA-48714	CA-16-7	28° 23.25'	83° 58.43'	1530	wood (root)	paleosoil buried by the granular avalanche breccia	835 ± 30	1212 AD ± 30
SacA-46541	CA-16-8-B	28° 23.25'	83° 58.43'	1530	small branch	base of the granular avalanche breccia	935 ± 35	1094 AD ± 48
SacA-48715	CA-16-8-E	28° 23.25'	83° 58.43'	1530	small branch	base of the granular avalanche breccia	825 ± 30	1229 AD ± 22
Pokhara basin								
SacA-41776	CA-13-245	28° 6.62	84° 7.18	588	small tree trunk	Paleosoil buried by the Pokhara Fm	740 ± 30	1261 AD ± 15
SacA-41777	CA-13-246	28° 6.64'	84° 7.19'	605	charcoal	Paleosoil buried by the Pokhara Fm	940 ± 30	1090 AD ± 46
SacA-43080	CA-13-246-B	28° 6.64'	84° 7.19'	605	charcoal	Paleosoil buried by the Pokhara Fm	955 ± 30	1082 AD ± 47
SacA-41773	CA-14-63-B	28° 8.05'	84° 5.70'	640	charcoal	Thin sand layer at the top of Pokhara Fm	1940 ± 30	57 AD ± 33
SacA-43079	CA-14-64-A	28° 7.17'	84° 6.31'	612	charcoal	Paleosoil buried by the Pokhara Fm	940 ± 30	1090 AD ± 46
SacA-41774	CA-14-64-B	28° 7.17'	84° 6.31'	612	charcoal	Paleosoil buried by the Pokhara Fm	940 ± 30	1090 AD ± 46
SacA-41775	CA-14-66	28° 5.60'	84° 4.53'	547	charcoal	Paleosoil buried by the Pokhara Fm	3375 ± 35	1678 BC ± 45
SacA-46544	CA-16-27	28° 5.57'	84° 3.89'	549	wood	slackwater deposits at tributary damming	870 ± 30	1139 AD ± 61
Narayangad								
WHOI-133624	CA-14-68E	27°42.83'	84°26.03'	198	Micro-charcoal	Silt layer at the base of fine conglomerates	885 ± 25	1126 AD ± 60

Table SI-10-1: Details of the samples of the organic debris found at Karuwa, in Pokhara basin and Narayangad, and dated by 14C AMS dating. Several charcoals, in particular CA-14-63B and CA-14-66 in paleosoils buried by the Pokhara conglomeratic formation, are clearly too old and suggest either long residence time in the soil (CA-14-66) or reworking (CA-14-63B).

SampleID	River	ref.	Latitude	Longitude	Sample elevation	Material	Pokhara Fm top elevation	Elevation of the Seti river	Age (calibrated 14C age AD)		
			(°N)	(°E)	(m asl)		(m asl)	(m asl)	mediane ($P_{50\%}$)	$P_{2.5\%}$	$P_{97.5\%}$
BIJ02	Bijaypur	36	28.219	84.029	820	Humic Silt	828	710	1246	1167	1290
PH02C	Phusre	36	28.18	83.968	730	Leaves	773	680	1193	1046	1269
PHUSRE03	Phusre	36	28.183	83.951	740	Charcoal	773	680	1098	1016	1205
SARA1-1	Saraudi	36	28.096	84.029	541	Wood	560	490	1265	1215	1298
MADHI2	Magdi	36	28.015	84.117	495	Charcoal	500	438	1061	990	1155
PH6	Phusre	36	28.175	83.976	703	Wood	773	680	1160	1038	1224
Phusre010	Phusre	36	28.175	83.982	706	Wood	773	680	1170	1043	1241
Phusre012	Phusre	36	28.175	83.982	698	Leaves	773	680	1232	1169	1270
Phusre013	Phusre	36	28.175	83.982	696	Wood	773	680	1199	1058	1262
Phusre14	Phusre	36	28.175	83.982	701	Charcoal	773	680	1219	1163	1264
PhusreFa	Phusre	36	28.185	83.958	728	Charcoal	773	680	1106	1033	1204
PRE14C1	Phusre	36	28.184	83.934	748	Charcoal	773	680	1347	1298	1410
KBP03	Bijaypur	36	28.218	84.027	825	Wood	828	710	1289	1263	1388
TAL02	Tal	36	28.117	84.105	583	Wood	623	530	1214	1161	1264
TAL05	Tal	36	28.117	84.105	614	Wood	623	530	1099	1025	1165
Anpu02	Anpu	36	28.109	84.116	591	Humic Silt	618	530	1097	1024	1155
KBP02	Bijaypur	37	28.218	84.027	825	Humic Silt	828	710	1176	1045	1250
Phusre11	Phusre	37	28.175	83.982	698	Wood	773	680	1186	1049	1256
Tal01	Tal	37	28.117	84.105	585	Humic Silt	623	530	1224	1165	1265
14CAnpu11	Anpu	37	28.108	84.114	590	Charcoal	618	530	1099	1025	1165
14CAnpu01	Anpu	37	28.111	84.105	556	Leaves	618	530	1186	1049	1256
14CAnpu16	Anpu	37	28.11	84.12	592	Charcoal	618	530	1214	1161	1264
BIJ03	Bijaypur	37	28.219	84.029	820	Humic Silt	828	710	1299	1270	1390
Ph6u_14C	Phusre	37	28.176	83.977	704	Wood	773	680	1113	1037	1207
EBGcc01	Anpu	37	28.111	84.12	609	Charcoal	618	530	698	656	769
PhTree1	Phusre	38	28.183	83.953	725	tree trunk	773	680	1232	1169	1270
PhTree2	Phusre	38	28.183	83.953	725	tree trunk	773	680	1272	1223	1295
AnpuTrib	Anpu	38	28.118	84.105	587	tree trunk	623	530	1209	1157	1264
AnpuTree1	Anpu	38	28.111	84.12	601	tree trunk	618	530	1242	1190	1279
AnpuTree2	Anpu	38	28.11	84.122	608	tree trunk	618	530	1240	1189	1277
AnpuTree3	Anpu	38	28.111	84.121	591	tree trunk	618	530	1228	1168	1266
AnpuTree4	Anpu	38	28.111	84.121	591	tree trunk	618	530	1199	1058	1262
AnpuTree5	Anpu	38	28.11	84.12	592	tree trunk	618	530	1224	1165	1265
CA-14-63-B	upper Begnas	this study	28.1342	84.0950	640	charcoal in sand lense	640	560	62	-20	130
CA-14-64-A	Rupa	this study	28.1195	84.1052	612	charcoal in paleosoil	623	532	1098	1025	1160
CA-14-64-B	Rupa	this study	28.1195	84.1052	612	charcoal in paleosoil	623	532	1098	1025	1160
CA-14-66	Seti Majuwa	this study	28.0933	84.0755	547	charcoal in paleosoil	585	507	-1669	-1753	-1549
CA-13-245	Anpu	this study	28.1103	84.1197	588	small tree trunk base	618	530	1270	1224	1291
CA-13-246	Anpu	this study	28.1107	84.1198	605	charcoal in paleosoil	618	530	1098	1025	1160
CA-13-246B	Anpu	this study	28.1107	84.1198	605	charcoal in paleosoil	618	530	1096	1022	1155
CA-16-27	Rudi	this study	28.0929	84.0649	549	wood	580	500	1176	1045	1250

Table SI-10-2: Published 14C dating (dated by AMS) of the various organic debris samples of the Pokhara conglomeratic formation, including their location and their elevation as well as that of the Seti and the top of the Pokhara formation used in fig.2b. The sample names in bold correspond to the most basal ones, used in fig.2a.

SI-11: ^{36}Cl dating of blocks at the rockslide deposit summit (4600m)

^{36}Cl exposure ages of the blocks sampled at the top of the deposit at ~4,600 m have been calculated incorporating snow cover correction and potential erosion. The snow cover correction corresponds to about 25-30 cm of snow (in water equivalent) during 120 days (mainly from January to May) and is calculated on the basis of 50% of the snow cover measured at several stations located between 3,200 and 4,400 m along the ridges that dominate the Khudi Khola (25 km east of Sabche cirque in a slightly more advanced position on the southern flank of the Himalayas) between 1999 and 2002 (ref. 57).

Using depth and duration of snow cover measured on the Himalayan southern flanks 25 km to the east[61], estimate of the shielding factor by snow would reach 0.87. However, as observed on site or on satellite images, the top of the plurimetric blocks are cleared of their snow cover much faster than the rest of the flat surrounding ground. Considering also that the Sabche cirque may be partially sheltered compared to the most exposed southern flank and receives less snow precipitation, we therefore adopt a conservative snow shielding factor of 0.95+/-0.5.

Sample name	Lithology	Latitude	Longitude	Altitude	boulder height above ground	sample thickness	Bulk density	Possible erosion of the block surface	Topographic shielding	Snow shielding
		(° N)	(° E)	(m)	(m)	(cm)	(g/cm^3)	(cm)		
CA13-260	marly limestone	28.5352	84.0274	4,590	5	3	2.6	0	0.975	0.94±0.05
CA13-261	schistosed marly sandstone	28.5359	84.0271	4,590	2.5	3	2.6	2±2	0.975	0.94±0.05
CA13-262	schistosed marl	28.5365	84.0276	4,590	5	4	2.6	1±1	0.975	0.94±0.05
CA13-263	schistosed marl	28.5374	84.0281	4,590	1 to 4	10	2.6	3±3	0.975	0.94±0.05
CA13-264	schistosed marl	28.5382	84.0284	4,590	1.2	5	2.6	2±2	0.975	0.94±0.05
CA13-265	schistosed marly sandstone	28.5394	84.0297	4,590	1.1	10	2.6	1±1	0.975	0.94±0.05

Table SI-11-1: Location and characteristics of the 6 blocks sampled on Nov. 2013 at the top of the relic surface of the rockslide deposit.

Sample name	% dissolved rock	^{36}Cl/^{35}Cl	^{35}Cl/^{37}Cl	^{36}Cl (/g of dissolved rock)	Cl (/m of dissolved rock)	CaO in target fraction	K_2O	TiO_2	Fe_2O_3	Exposure age without snow shielding	Exposure age with snow shielding
	%	($\times10^{-13}$)		10^3 atoms/g	[ppm]	%	%	%	%	yr	yr
CA13-260	82.2	2.706 ± 0.081	33.387 ± 0.793	168.3 ± 5.2	4.4	52.36	0	0	0	796 ± 70	839 ± 76
CA13-261	52.8	1.551 ± 0.058	40.284 ± 1.317	165.5 ± 6.5	6.2	54.28	0	0	0	758 ± 69	799 ± 74
CA13-262	75.6	2.493 ± 0.075	24.061 ± 0.886	170.5 ± 5.3	6.8	51.86	0	0	0	816 ± 70	860 ± 80
CA13-263	72.9	2.157 ± 0.071	27.046 ± 1.115	145.1 ± 4.9	5.9	52.69	0	0	0	749 ± 73	790 ± 76
CA13-264	75.7	1.130 ± 0.049	31.172 ± 1.218	84.7 ± 3.8	5.7	52.65	0	0	0	423 ± 39	446 ± 43
CA13-265	26.0	0.515 ± 0.032	31.209 ± 1.295	93.6 ± 6.4	14.0	54.41	0	0	0	446 ± 46	470 ± 49
Blank		0.072 ± 0.012	427.025 ± 3.187								

Table SI-11-2: Sample information, AMS measurement results, and calculated ^{36}Cl and chlorine concentrations and concentration of Ca measured at ICP-AES (inductively coupled plasma atomic emission spectrometry). Exposure ages calculated with Online Chronus Calculator (http://hess.ess.washington.edu/math/index_dev.html). Reported analytical uncertainties include uncertainties in AMS counting statistics, the isotopic ratios of the standards, and on the blank chemical measurements, an external AMS error of 0.5% (Arnold et al., 2010), and the uncertainties associated with the cosmogenic nuclide half-lives. External uncertainties include the uncertainties associated with the cosmogenic nuclide production rates, the sample thickness, the estimated surface and snow shielding.

Sample Name	SiO_2	TiO_2	Al_2O_3	Fe_2O_3	MnO	MgO	CaO	Na_2O	K_2O	H_2O	Cl	B	Sm	Gd	U	Th	Cr	Li
	%	%	%	%	%	%	%	%	%	%	ppm	ppm	ppm	ppm	ppm	ppm	ppm	ppm
CA13-260	9.65	0.09	1.80	0.76	0.01	2.36	45.49	0.41	0.51	0.43	10	9	0.92	0.75	0.69	2.60	4.3	5.2
CA13-261	31.12	0.26	4.79	0.89	0.02	2.09	31.64	1.11	1.16	0.79	10	22	2.07	1.71	1.49	8.13	15.3	12.8
CA13-262	13.70	0.13	2.52	0.81	0.02	2.53	42.45	0.65	0.70	0.49	10	12	1.60	1.29	0.84	3.66	7.2	6.2
CA13-263	15.83	0.19	3.60	1.00	0.02	2.65	40.65	0.58	1.12	0.61	10	17	2.45	1.95	0.81	5.22	14.5	11.3
CA13-264	15.62	0.19	3.70	1.18	0.02	1.80	41.05	0.55	1.03	0.65	10	36	2.13	1.80	0.70	5.54	16.5	9.8
CA13-265	45.41	0.44	8.57	2.84	0.03	3.03	19.02	1.21	2.58	1.31	25	46	4.21	3.49	1.55	11.9	33.2	23

Table SI-11-3: Bulk rocks geochemical composition of the 6 blocks sampled at the top of the relic surface of the rockslide deposit: Major and trace elements composition measured by ICP-MS (SARM, CRPG).

SI-12: Infra-red stimulated luminescence (IRSL) measurements and results on sheared breccia deposits

Breccia samples were first sawed in subdued light conditions to remove the exposed outer rock surfaces. Samples were then dissolved in HCl. and the silicate fraction was treated using H_2O_2 (30%) and sieved to coarse sand fraction before density separation with LST to isolate K-felspar fraction (d<2.58). K-feldspar separates were settled on 10-mm diameter stainless steel discs for subsequent luminescence analyses. About 50 g of bulk sample was saved (external breccia surface) and sent to Actlabs or SARM-CRPG for ICP analysis to quantify U, Th and K contents (Table SI-8-1). Final dose rate determination, using grainsize range and estimated water content, were obtained through the Dose Rate and Age Calculator[59] (DRAC).

All conventional luminescence measurements were carried out using TL/OSLDA-20 Risø readers, equipped with a calibrated $^{90}Sr/^{90}Y$ beta source (reader dose rate ~0.1Gy/s; Institute of Earth Surface Dynamics, University of Lausanne, Switzerland). Luminescence signals were detected using an EMI 9235QA photomultiplier tube, in the blue region through a Schott BG-39 filter for IRSL measurements. We used the post-IR IRSL protocol[60], applying first a preheat treatment at 250°C for 60s before a single-aliquot regenerative-dose (SAR) protocol (Murray & Wintle 2000) with a first IRSL stimulation at 50 °C (100 s, IR50) followed by a second IRSL stimulation at 225 °C (100 s, pIR225). For all the samples, residual doses and dose recovery ratios were quantified. Dose–response curves were constructed using an exponential+linear fitting (with recycling ratios within 15% of unity and recuperation within 10% of the natural dose were used as acceptance criteria for the single-aliquot data).
We used the Luminescence R package (Kreutzer et al. 2012) to quantify the Central Age Model (CAM) for all samples[61], and based on the overdispersion in De distributions we also calculated a Minimum Age Model (MAM) for sample CA-13-283 (ref. 61). Fading rates (g_{2days}) were measured following Auclair et al. (2003) (Figure SI-12-1). Final fading-corrected ages were calculated following ref. 62 fading correction procedure (Table SI-12-2).

Sample	Coordinates (WGS84, °N/°E, and elevation, m a.s.l.)	Radionuclide concentration[1]			Grain size range[2] (μm)	Total dose rate[3] (Gy ka^{-1})
		U (ppm)	Th (ppm)	K (%)		
CA-13-273	28.5058; 84.0001 3410	1.69±0.06	10.8±0.38	1.82±0.06	90-180	3.83±0.21
CA-13-274	28.5058; 84.0001 3410	1.64±0.06	10.3±0.36	1.90±0.07	90-180	3.85±0.21
CA-13-283	28.5055; 83.9999 3405	2.15±0.08	12.6±0.44	2.04±0.07	180-250	4.39±0.17

Table SI-12-1. Details of dose-rate calculations for IRSL dating.
Samples were collected at the base of the breccia deposit (see Extended Data Figs. 2 and 6) but this was rapidly incised after deposition. To account for this, a 0.25 Gy dose has been substracted for post-deposition exposure to cosmic rays.
[1]Radionuclide concentrations were quantified on bulk samples using ICP at Actlabs (CA-13-273/-274) and at SARM-CRPG (CA-13-283).
[2]Coarse-grain fraction of 90-180 μm was isolated for samples CA-13-273 and CA-13-274, and of 180-250 μm for CA-13-283, to ensure material abundance for IRSL measurements.
[3]Dose rate calculations were performed with DRAC[59], assuming water content of 2±2%, an internal K-content of 12.5±0.5% (Huntley and Baril, 1997) and an alpha efficiency value of 0.15±0.05 (Balescu and Lamothe, 1994).

Sample (*aliquots*)	Signal	Dose recovery ratio[1]	residuals[1] (Gy)	CAM[2] uncorrected D_e (Gy)	OD[2] (%)	MAM[3] uncorrected D_e (Gy)	Fading[4] g_{2days} (%/decade)	CAM or MAM* fading-corrected age (ka)
CA-13-273 (*17*)	IR50	0.94±0.04	0.57	84.2±9.0	9.2	/	1.40±0.48	31.9±4.3
	pIR225	0.90±0.03	2.27	156.7±25.8	15.0	/	0.58±0.34	34.6±4.1
CA-13-274 (*17*)	IR50	0.94±0.04	0.57	90.5±8.8	8.0	/	1.47±0.75	64.4±7.4
	pIR225	0.91±0.03	2.26	155.8±26.0	15.3	/	0.63±0.28	48.1±2.5
CA-13-283 (*60*)	IR50	0.88±0.02	0.25	7.5±2.2	28.7	5.2±0.6	1.37±0.64	1.21±0.23*
	pIR225	0.86±0.02	0.27	8.7±2.9	32.3	6.2±1.0	0.59±0.39	1.50±0.30*

Table SI-12-2. IRSL dating of the base of the breccia deposit (see Extended Data Figs. 2d and 6) on small-aliquots, using feldspar infra-red luminescence at 50°C (IR50) and post-infra-red infra-red luminescence at 225°C (pIR225) signals. Analytical details and measurement protocols are given in supplementary text.
[1]Dose recovery ratios have been calulated for each individual sample and using a given dose of 60Gy for 5 aliquots. Residuals have been estimated for 4 aliquots per sample, with an additional 0.25 Gy to account for post-deposition cosmic-ray exposure following rapid breccia incision.
[2]De = Equivalent doses, CAM = Central Age Model, OD = overdispersion of D_e distribution[61].
[3]MAM = Minimum Age Model[61] (MAM-3). It was applied for D_e distributions with OD > 25%, i.e. for sample CA-13-283. Sigma-b (σ_b) values of 0.085 and 0.152 were used for IR50 and pIR225 signals, respectively, based on OD values for CA-13-273/-274 samples. No MAM was run for CA-13-273/-274, due to the low OD in the D_e distribution (Fig. SI-12-1).
[4]Fading measurements have been performed on 12-14 aliquots per sample to evaluate the variability in fading rates for IR50 and pIRI225 signals (Fig. SI-12-1).

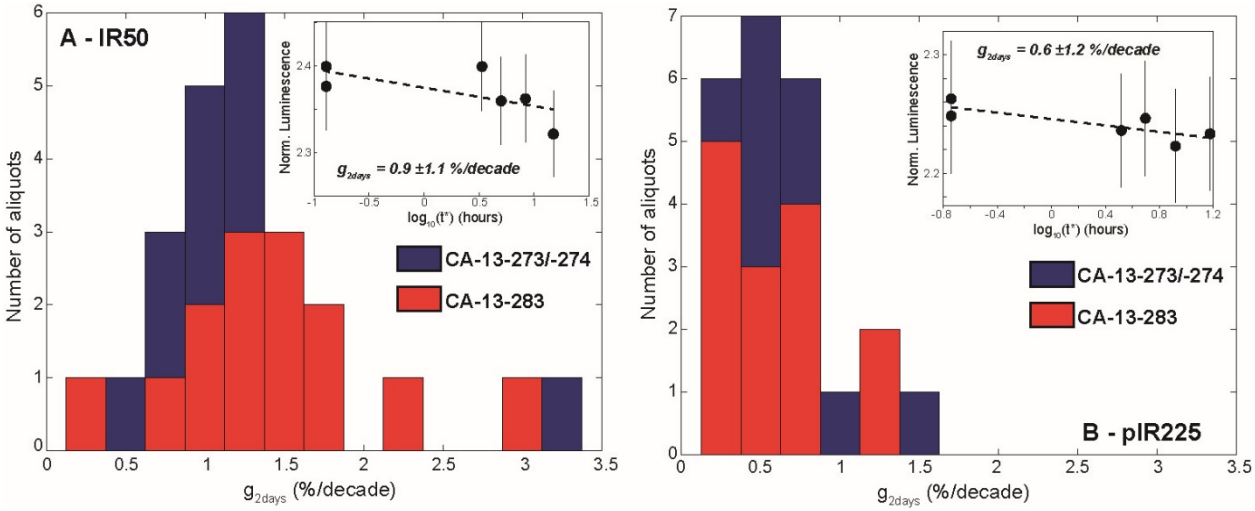

Fig. SI-12-1. Fading rate (g2days values) distributions for K-feldspar IR50 (A) and pIRIR225 (B) signals. Insets show representative examples of fading measurements. Fading rate distributions illustrate similar behaviour between CA-13-273, -274 and -283.

SI-13: Carbonate content

Total carbonate (*Table SI-13-1*) content was measured by phosphoric acid dissolution at 70°C on a gas-bench coupled to a MAT253 spectrometer using internal concentration standards. Concentrations are expressed in equivalent $CaCO_3$ wt% and the overall uncertainty is ± **2**% relative.

Sample	Sample Type	Lithology	river / location	Latitude	Longitude	distance from Sabche divide	$CaCO_3$
				(°N)	(°E)	(km)	%
Rivers							
Seti & downstream (Trisuli, Narayani)							
HF 10	sand (bank)	sand	Seti Kh. North of Pokhara	28.4200	83.9921	19	56.0
CA-13-232	sand (bank)	sand	Seti Kh. North of Pokhara	28.3219	83.9573	30	29.4
CA-13-233	sand (bank)	silt	Seti Kh. North of Pokhara	28.3219	83.9573	30	48.5
HF 11	sand (bank)	sand	Seti Khola	28.3015	83.9429	36	44.0
LO 313	sand (bank)	sand	Seti Khola	28.1274	84.0836	69.5	44.4
MO 305	Suspended Load	silt	Seti Khola	28.0500	84.0700	78.5	47.0
CA-14-72	sand (bank)	sand	Seti Khola	27.8273	84.4662	142	11.0
LO 303	sand (bank)	sand	Seti Khola	27.8255	84.4635	142	24.7
CA 11133	sand (bank)	sand	Seti Khola	27.8292	84.4667	142	*17*
CA13-251	sand (bank)	sand	lower Trisuli	27.7564	84.4638	157.3	8.2
CA-14-67	sand (bank)	sand	Narayani	27.7022	84.4262	166.5	9.18
LO 309	sand (bank)	sand	Narayani	27.7020	84.4260	166.5	14.7
NAG 48	sand (bank)	sand	Narayani	27.7020	84.4260	166.5	13.8
LO 741	sand (bank)	sand	Nayayani	27.7020	84.4260	166.5	15.0
CA 11-140	sand (bank)	sand	Narayani	27.7020	84.4260	166.5	9.19
Narayani	sand (mean)	sand	Narayani @ Narayangad	27.7020	84.4260	166.5	12.4
	(std)						2.9
Narayani	Suspended load (average 2010 monsoon)	silt	Narayani @ Narayangad	27.7020	84.4260	166.5	16.4
	(std)						3.9
CA 11305	sand (bank)	sand	Narayani	26.8598	84.2098	337	9.3
CA 11306A	sand (bank)	Bank	Narayani	27.2059	83.9300	284	10.1
CA 11306B	sand (bank)	Bank	Narayani	27.2059	83.9300	284	7.8
CA 11306D	sand (bank)	Bank	Narayani	27.2059	83.9300	284	7.9
CA 11307	sand (bank)	Bank	Narayani	27.1215	84.0609	301	9.4
CA 11308	sand (bank)	Bank	Narayani	26.6890	84.4333	369	11.2
Main Tributaries							
CA-13-237	sand (bank)	sand	Mardi Khola	28.2996	83.9267	38	7.9
CA-13-238	sand (bank)	sand	Madi Khola	28.2341	84.0868	113	2.4
CA-13-239	silt (bank)	silt	Madi Khola	28.2243	84.0592	113	4.2
CA-13-247	sand (bank)	sand	Madi Khola	27.9783	84.2600	113	3.64
LO 305	sand (bank)	sand	Trisuli	27.8180	84.4640	144	3.2

LO 307	sand (bank)	sand	Kali Gandaki	27.7486	84.4194	161	12.3
CA11136	sand (bank)	sand	Kali Gandaki	27.7486	84.4194	161	21.2
CA-13-126	sand (bank)	sand	Kali Gandaki	27.7486	84.4194	161	15.6
CA-13-128	sand (bank)	sand	Kali Gandaki	27.7486	84.4194	161	17.9
Breccia (Sabche rockslide deposit)							
CA-13-270	breccia	matrix	Sabche cirque _ base of deposit	28.5061	83.9999	5	48.6
CA-13-275	sediment in gully	sand	Sabche cirque _ base of deposit	28.5039	83.9996	5	65.1
							66.7
CA13-275_A	sediment in gully	clast	Sabche cirque _ base of deposit	28.5039	83.9996	5	15.9
CA13-275_B	sediment in gully	clast	Sabche cirque _ base of deposit	28.5039	83.9996	5	99.0
CA13-275_C	sediment in gully	clast	Sabche cirque _ base of deposit	28.5039	83.9996	5	82.6
CA13-275_D	sediment in gully	clast	Sabche cirque _ base of deposit	28.5039	83.9996	5	87.7
CA-13-280		mixed clasts	Sabche cirque _ base of deposit	28.5056	83.9999	5	79.2
CA13-280_A	breccia	mixed clasts	Sabche cirque _ base of deposit	28.5056	83.9999	5	58.7
CA13-280_B	breccia	mixed clasts	Sabche cirque _ base of deposit	28.5056	83.9999	5	75.1
CA-13-281		matrix	Sabche cirque _ base of deposit	28.5056	83.9999	5	41.2
CA13-281_A	breccia	clast	Sabche cirque _ base of deposit	28.5056	83.9999	5	55.6
CA13-281_B	breccia	clast	Sabche cirque _ base of deposit	28.5056	83.9999	5	20.8
CA13-281_C	breccia	clast	Sabche cirque _ base of deposit	28.5056	83.9999	5	88.5
CA13-281_D	breccia	clast	Sabche cirque _ base of deposit	28.5056	83.9999	5	71.0
Breccia (upper Seti rock avalanche deposit)							
CA-14-57	avalanche deposit (top)	matrix	upper Seti Kh. _ Nanhe spur	28.4112	83.9871	21	55.9
CA-14-56	fluid injection vein	greenish part	upper Seti Kh. _ Karuwa	28.3870	83.9751	24	42.9
		pinkish part					43.8
		whitish part					19.8
CA-14-60	breccia of light tone clasts		upper Seti Kh. _ Karuwa	28.3870	83.9751	24	46.5
							41.3
CA-16-9	avalanche deposit (base)	matrix	upper Seti Kh. _ Karuwa	28.3875	83.9738	24	21.8
CA-16-10	avalanche deposit (base)	matrix	upper Seti Kh. _ Karuwa	28.3875	83.9738	24	27.4
CA-16-11	avalanche deposit (base)	matrix	upper Seti Kh. _ Karuwa	28.3875	83.9738	24	35.4

CA-16-12	avalanche deposit (base)	matrix	upper Seti Kh. _ Karuwa	28.3875	83.9738	24	33.2
		gravels					39.9
CA-16-13	avalanche deposit (base)	matrix	upper Seti Kh. _ Karuwa	28.3875	83.9738	24	29.7
CA-16-14	avalanche deposit (base)	matrix	upper Seti Kh. _ Karuwa	28.3875	83.9738	24	55.9
CA-16-15	avalanche deposit (base)	light tone gravels	upper Seti Kh. _ Karuwa	28.3875	83.9738	24	39.6
		dark gravels					33.3
		matrix					41.5
CA-16-17	avalanche deposit (base)	matrix	upper Seti Kh. _ Karuwa	28.3873	83.9750	24	32.3
CA-16-18	avalanche deposit (base)	matrix	upper Seti Kh. _ Karuwa	28.3873	83.9750	24	45.5
		light tone gravels					26.9
		dark gravels					13.6
CA-16-19	avalanche deposit (base)	matrix	upper Seti Kh. _ Karuwa	28.3873	83.9750	24	30.3
CA-16-20	avalanche deposit (base)	matrix	upper Seti Kh. _ Karuwa	28.3869	83.9750	24	30.9
CA-16-4	avalanche deposit (base)	matrix	upper Seti Kh. _ Karuwa	28.3846	83.9757	24.5	38.2
CA-16-21	avalanche deposit (base)	matrix	upper Seti Kh. _ Karuwa	28.3828	83.9754	24.8	28.6
CA-16-2	avalanche deposit (middle height)	gravels	upper Seti Kh. _ Karuwa	28.3806	83.9733	25	59.8
		matrix				25	68.3
CA-16-3	avalanche deposit (middle height)	matrix	upper Seti Kh. _ Karuwa	28.3825	83.9732	25	70.5
CA-16-22	avalanche deposit (middle height)	matrix	upper Seti Kh.	28.3594	83.9571	29	59.6
CA-13-234	avalanche deposit (middle height)	matrix	Seti Kh. _ North of Pokhara	28.3203	83.9567	34	28.2
CA-14-62	isolated breccia remnant	matrix	Seti Kh. _ South of Pokhara	28.1229	84.0849	68.5	40.3
Pokhara formation							
CA-19-18	conglomerate	gravels	upper Seti Kh. _ Karuwa	28.3860	83.9750	24	32.7
CA19-18_A	conglomerate	individual gravel	upper Seti Kh. _ Karuwa	28.3860	83.9750	25	14.3
CA19-18_B	conglomerate	individual gravel	upper Seti Kh. _ Karuwa	28.3860	83.9750	25	75.0
CA19-18_C	conglomerate	individual gravel	upper Seti Kh. _ Karuwa	28.3860	83.9750	25	58.0
CA19-18_D	conglomerate	individual gravel	upper Seti Kh. _ Karuwa	28.3860	83.9750	25	74.4
CA-16-24	conglomerate	gravels	upper Seti Kh.	28.3591	83.9566	29	59.1
		matrix				29	52.7
CA-13-236	conglomerate		Seti Kh. _ north of Pokhara	28.3096	83.9406	37	58.5
CA-14-61	fine conglomerate	matrix	Seti Kh. _ north of Pokhara	28.1340	84.0731	66.3	55.7

CA-13-240	slackwater deposit	silt	Seti Kh. _ south of Pokhara	28.1088	84.1151	70	58.1
						70	57.1
						70	58.9
CA-13-241	unstratified angular clasts unit	gravels	Seti Kh._ south of Pokhara	28.1083	84.1156	70	63.1
						70	62.2
		matrix				70	59.9
						70	58.6
						70	62.6
						70	62.5
CA-14-65	unstratified angular clasts unit	matrix	Seti Kh.	28.0933	84.0755	73	63.7
CA-16-30	upper part of Pokhara Fm	silt	Seti Kh. _ south of Pokhara basin	28.0926	84.0688	73.5	55.1
CA-16-31	unstratified angular clasts unit	matrix	Seti Kh. _ south of Pokhara	28.0182	84.0967	83	53.8
CA-13-249	fine conglomerate		lower Trisuli	27.7564	84.4638	157.3	51.5
						157.3	52.8
CA-13-252	fine conglomerate	gravels	Narayani at Narayangad	27.7137	84.4339	164	54.5
						164	58.4
		matrix				164	50.4
						164	50.4
CA-14-69	conglomerate	matrix	Narayani at Narayangad	27.7140	84.4339	164	45.6
		mixed gravels				164	52.5
CA14-69_A	conglomerate	gravel	Narayani at Narayangad	27.7140	84.4339	164	79.1
CA14-69_B	conglomerate	gravel	Narayani at Narayangad	27.7140	84.4339	164	38.7
CA14-69_C	conglomerate	gravel	Narayani at Narayangad	27.7140	84.4339	164	65.2
CA14-69_D	conglomerate	gravel	Narayani at Narayangad	27.7140	84.4339	164	68.7
CA14-69_E	conglomerate	gravel	Narayani at Narayangad	27.7140	84.4339	164	10.5
CA-14-70	coarse sand unit	sand	Narayani at Narayangad	27.7140	84.4339	164	48.6
						164	47.5
CA-14-71	silty unit	silt	Narayani at Narayangad	27.7140	84.4339	164	45.3
						164	45.2
pit near GR2 core (Gandak fan)							
GR2_16-5	sediment @ -2.85m below surface	sand	Dudahi (India)	26.8161	84.1458	337	73.1
GR2_16-6	sediment @ -2.45m below surface	fine sand	-	-	-	337	32.5
GR2_16-7	sediment @ -2m below surface	micaceous sand	-	-	-	337	18.5
GR2_16-8	sediment @ -1.7m below surface	silt / fine sand	-	-	-	337	33.7

GR2 16-9	sediment @ -1.2m below surface	silt / fine sand	-	-	-	337	41.9
GR2 16-2	sediment @ -0.9m below surface	silt / fine sand	-	-	-	337	36.6
GR2 16-10	sediment @ -0.65m below surface	silt	-	-	-	337	44.4
TSS Rocks							
CA-13-260	block on surface of rockslide deposit	Sombre Fm (Silurian)	Seti (upper)	28.5352	84.0274		90.7
							86.6
							85.6
CA-13-261	block on surface of rockslide deposit	Sombre Fm (Silurian)	Seti (upper)	28.5359	84.0271		48.7
							44.9
							48.7
CA-13-265	block on surface of rockslide deposit	Sombre Fm (Silurian)	Seti (upper)	28.5394	84.0297		41.3
							40.7
CA-14-29	morainic block	Sombre Fm (Silurian)	Upper Marsyandi	28.6069	84.0525		62.4
CA-14-32	morainic block	Sombre Fm (Silurian)	Upper Marsyandi	28.6042	84.0516		41.4
							40.5
CA-14-36	glacial striated surface	lower Nilgiri Fm (ordovicien)	Upper Marsyandi	28.6012	84.0508		49.0
							51.3
CA-14-38	morainic block	Sombre Fm (Silurian)	Upper Marsyandi	28.5977	84.0510		59.3
CA-14-40	morainic block	Sombre Fm (Silurian)	Upper Marsyandi	28.5957	84.0513		88.1
CA-14-44	morainic block	Sombre Fm (Silurian)	Upper Marsyandi	28.5985	84.0563		81.9
UM-18-3	bedrock	annapurna lm (cambrien)	Upper Marsyandi	28.5590	84.2220		58.0
UM-18-4	bedrock	annapurna lm (cambrien)	Upper Marsyandi	28.5758	84.1870		55.2
UM-18-8	bedrock	top of annapurna lm (cambrien)	Upper Marsyandi	28.5905	84.1949		59.8
UM-18-10	bedrock	top of annapurna lm (cambrien)	Upper Marsyandi	28.5923	84.1949		60.9
UM-18-11	bedrock	lower Nilgiri Fm (ordovicien)	Upper Marsyandi	28.6029	84.1742		78.6
UM-18-12	bedrock	Nilgiri Fm (ordovicien)	Upper Marsyandi	28.6105	84.1514		32.0
UM-18-13	bedrock	top of Nilgiri Fm (Silurian)	Upper Marsyandi	28.6252	84.1331		56.2

Table SI-13-1: Summary of the $CaCO_3$ content of Sabche rocklside deposit, related sediments further downstream, modern river sediment of the area, and of the Silurian to Cambrian TSS units typical of rockslide source.

References:

Aaron, J., & McDougall, S. (2019). Rock avalanche mobility: the role of path material. *Engineering Geology*, *257*, 105126.

Arnold, M., Merchel, S., Bourlès, D. L., Braucher, R., Benedetti, L., Finkel, R. C., ... & Klein, M. (2010). The French accelerator mass spectrometry facility ASTER: improved performance and developments. *Nuclear Instruments and Methods in Physics Research Section B: Beam Interactions with Materials and Atoms*, *268*(11-12), 1954-1959.

Auclair, M., Lamothe, M. & Huot, S. 2003: Measurement of anomalous fading for feldspar IRSL using SAR. Radiation Measurements 37, 487–492.

Balescu, S. & Lamothe, M., 1994: Comparison of TL and IRSL age estimates of feldspar coarse grains from waterlain sediments. Quat. Sci. Rev. 13, 437-444.

Blair, T. C., & McPherson, J. G. (2009). Processes and forms of alluvial fans. In *Geomorphology of desert environments* (pp. 413-467). Springer, Dordrecht.

Buylaert, J.P., Murray, A.S., Thomsen, K.J. & Jain, M. 2009: Testing the potential of an elevated temperature IRSL signal from K-feldspar. Radiation Measurements 44, 560–565.

Chen, Q., Cheng, H., Yang, Y., Liu, G., & Liu, L. (2014). Quantification of mass wasting volume associated with the giant landslide Daguangbao induced by the 2008 Wenchuan earthquake from persistent scatterer InSAR. *Remote sensing of environment*, *152*, 125-135.

Delgado, F., Zerathe, S., Audin, L., Schwartz, S., Benavente, C., Carcaillet, J., ... & Team, A. (2020). Giant landslide triggerings and paleoprecipitations in the Central Western Andes: The aricota rockslide dam (South Peru). *Geomorphology*, *350*, 106932.

Durcan, J.A., King, G.E. & Duller, G.A.T. 2015: DRAC: Dose Rate and Age Calculator for trapped charge dating. Quaternary Geochronology 28, 54–61.

Fort, M. (2000). Glaciers and mass wasting processes: their influence on the shaping of the Kali Gandaki valley (higher Himalaya of Nepal). *Quaternary International*, *65*, 101-119.

Galbraith, R.F., Roberts, R.G., Laslett, G.M., Yoshida, H. & Olley, J.M., 1999: Optical dating of single and multiple grains of quartz from jinmium rock shelter, northern Australia: part i, experimental design and statistical models. Archaeometry 2, 339-364.

Guérin, C. (2017). Effect of the DTM quality on the bundle block adjustment and orthorectification process without GCP: Exemple on a steep area. In *2017 IEEE International Geoscience and Remote Sensing Symposium (IGARSS)* (pp. 1067-1070). IEEE.Huntley, D.J. & Baril, M.R., 1997: The K content of the K-feldspars being measured in optical dating or in thermoluminescence dating. Anc. TL 15, 11-13.

Kreutzer, S., Schmidt, C., Fuchs, M.& Dietze, M. 2012: Introducing an R package for luminescence dating analysis. Ancient TL 30, 1–8.

Murray, A.S. & Wintle, A.G. 2000: Dating quartz using an improved single-aliquot regenerative-dose (SAR) protocol, Radiation Measurements 32, 57–73.

Pierrot-Deseilligny, M., & Paparoditis, N. (2006). A multiresolution and optimization-based image matching approach: An application to surface reconstruction from SPOT5-HRS stereo imagery. *Archives of Photogrammetry, Remote Sensing and Spatial Information Sciences*, *36*(1/W41), 1-5.

Pollet, N., & Schneider, J. L. (2004). Dynamic disintegration processes accompanying transport of the Holocene Flims sturzstrom (Swiss Alps). *Earth and Planetary Science Letters*, *221*(1-4), 433-448.

Strom, A., Li, L., & Lan, H. (2019). Rock avalanche mobility: optimal characterization and the effects of confinement. *Landslides*, *16*(8), 1437-1452.

Weidinger, J. T., & Ibetsberger, H. J. (2000). Landslide dams of Tal, Latamrang, Ghatta Khola, Ringmo, and Darbang in the Nepal Himalayas and related hazards. *Journal of Nepal Geological Society*, *22*, 371-380.

Zangerl, C., Schneeberger, A., Steiner, G., & Mergili, M. (2021). Geographic-information-system-based topographic reconstruction and geomechanical modelling of the Köfels rockslide. *Natural Hazards and Earth System Sciences*, *21*(8), 2461-2483.

Zhang, L., Xiao, T., He, J., & Chen, C. (2019). Erosion-based analysis of breaching of Baige landslide dams on the Jinsha River, China, in 2018. *Landslides*, *16*(10), 1965-1979.

Zhou, T. J., Li, B., Man, W. M., Zhang, L. X., Zhang, J., 2011. A comparison of the Medieval Warm Period, Little Ice Age and 20th century warming simulated by the FGOALS climate system model. Chinese Science Bulletin 56 (28-29), 3028–3041.